

UNIVERSITÀ DEGLI STUDI DI MILANO BICOCCA  
Facoltà di Scienze Matematiche, Fisiche e Naturali  
Dottorato di Ricerca in Astronomia e Astrofisica XVII ciclo

**GAMMA-RAY EMISSION FROM THE  
GALACTIC PLANE:  
A NEW MODEL FOR AGILE**

Supervisor :

**Dr. Sandro MEREGHETTI**

Tutor :

**Prof. Monica COLPI**

Coordinatore :

**Prof. Guido CHINCARINI**

PHD thesis of :

**Andrea GIULIANI**

Matricola R00185

Università degli Studi di Milano Bicocca  
Facoltà di Scienze Matematiche, Fisiche e Naturali  
Dottorato di Ricerca in Astronomia e Astrofisica  
XVII ciclo  
A.A. 2003/2004

## **GAMMA-RAY EMISSION FROM THE GALACTIC PLANE: A NEW MODEL FOR AGILE**

Supervisore: Dr. Sandro Mereghetti (IASF-CNR)

Tutor: Prof. Monica Colpi (Università di Milano-Bicocca)

Coordinatore: Prof. Guido Chincarini (Università di Milano-Bicocca)

Commissione:

Prof. G. Gavazzi (Università di Milano-Bicocca, Presidente)

Prof. T. Courvoisier (Université de Geneve)

Prof. F. Frontera (Università di Ferrara)

Dott. B. Poggianti (INAF - OAPd)

Dott. A. Strong (MPE Garching)

Dott. E. Costa (IASF - CNR)

**Tesi di:**  
**Andrea Giuliani**  
**Matricola R00185**

IASF - CNR, Sezione di Milano “G. Occhialini”, Via Bassini 15 - 20133 - Milano



# Contents

<b>Introduction</b>	<b>4</b>
<b>1 Gamma-Ray Emissivity of the Interstellar Medium</b>	<b>9</b>
1.1 The Interstellar Matter . . . . .	11
1.1.1 The Molecular Clouds . . . . .	12
1.1.2 The Atomic Hydrogen . . . . .	13
1.1.3 The Ionized Hydrogen . . . . .	17
1.2 The Interstellar Radiation Field . . . . .	17
1.3 The magnetic field . . . . .	19
1.4 Cosmic Rays . . . . .	20
1.4.1 Cosmic Electrons . . . . .	22
1.4.2 Cosmic Protons . . . . .	26
1.5 The physical processes producing gamma-ray emissivity . . . .	27
1.5.1 Proton-Proton collisions . . . . .	27
1.5.2 Electron Bremsstrahlung . . . . .	30
1.5.3 Inverse Compton . . . . .	33

<b>2</b>	<b>Modeling the Gamma-Ray Emission of the Galaxy</b>	<b>35</b>
2.1	The EGRET observations and the EGRET diffuse emission model	35
2.2	Beyond the EGRET model . . . . .	37
2.3	The AGILE diffuse gamma-ray emission model . . . . .	41
2.4	Mapping the matter distribution in the Galaxy . . . . .	43
2.5	Line broadening and anomalous velocities . . . . .	46
2.6	The dynamical ambiguity . . . . .	47
2.7	Rotation curve . . . . .	48
2.8	Diffuse matter distribution . . . . .	49
2.9	Interstellar Radiation Field . . . . .	51
2.10	Cosmic Rays . . . . .	51
<b>3</b>	<b>Observing the Diffuse Emission</b>	<b>55</b>
3.1	The gamma-ray sky . . . . .	55
3.2	New vs old model . . . . .	56
3.3	Model vs Observations . . . . .	61
3.4	Cosmic-Ray Studies . . . . .	69
3.5	AGILE and the Diffuse $\gamma$ -ray emission . . . . .	80
3.6	A simulated AGILE observation . . . . .	82
<b>4</b>	<b>AGILE performances optimization</b>	<b>85</b>
4.1	The AGILE instrument . . . . .	86

<i>CONTENTS</i>	<b>3</b>
4.2 On-board tracks reconstruction . . . . .	90
4.2.1 Event reconstruction in pair production detectors . . .	93
4.2.2 The "Kalmaex Algorithm" . . . . .	94
4.2.3 Simulation Results . . . . .	99
4.2.4 Background rejection . . . . .	99
4.3 On-ground tracks reconstruction . . . . .	101
4.3.1 Spectral capabilities . . . . .	107
<b>5 Conclusions</b>	<b>111</b>
<b>Acknowledgments</b>	<b>115</b>
<b>Bibliography</b>	<b>116</b>



# Introduction

The interaction between cosmic rays and the Galactic interstellar medium produces a non-thermal emission which is very intense in the high-energy gamma-ray band, making the Milky way the most prominent source in the sky at energies greater than 100 MeV.

Studies of gamma emission from the interstellar medium, by means of high-energy gamma-ray telescopes, provide important information on the distribution of both cosmic rays and interstellar medium. In particular observations with the EGRET instrument on board of the NASA Compton Gamma-Ray Observatory (CGRO) led to important conclusions concerning, for example, the galactic origin of cosmic rays. Nonetheless, many questions concerning the cosmic rays and interstellar medium components remain open. The gamma-ray telescope AGILE, to be launched in 2005 and operating in the band 30 MeV - 30 GeV and 15-45 KeV will be able to improve our knowledge of the gamma-ray diffuse emission, because of its large field of view (covering one fourth of the sky), and its angular resolution much better than that of previous instruments. In order to explain the observations of the diffuse gamma-ray emission a set of theoretical models is required to be considered in detail. Moreover, the galactic diffuse gamma-ray emission represents a background component for the study of discrete gamma-ray sources, even at high galactic

latitudes. The data analysis for any source in the gamma band requires a likelihood analysis, for which a model of the background due to galactic emission is a crucial input.

In chapters 1 and 2 of this thesis I describe the development of a model of the diffuse gamma-ray emission to be used in the forthcoming AGILE observations. This new model is represented by a 4-dimensional matrix  $g(l,b,r,E)$ , in which the spatial coordinates map the whole Galaxy, while the fourth dimension gives, for each cell, the gamma emissivity spectrum. The latter is evaluated as the sum of different contributions due to three production processes (pp scattering, Bremsstrahlung and inverse Compton). The model is built first by obtaining the three-dimensional distributions of cosmic rays and of the components of interstellar medium relevant for the gamma-ray production: HI regions, molecular clouds and interstellar radiation field. Using these distributions, the emission spectra in the gamma-ray band for the three process are calculated, and finally the predicted intensity of the gamma-ray sky is obtained by integrating the gamma-ray emissivity along the line of sight.

In Chapter 3, I present an original method that I propose to extract information on the cosmic-rays galactic distribution from the diffuse gamma-ray observations. This technique uses the matter distribution obtained from the model presented in the previous chapters, but it does not assume any cosmic-ray distribution. It can therefore be used to test theoretical cosmic-ray models. This method, that we have tested on EGRET data, can be easily applied to future observations from other satellites.

In chapter 4, I describe the work done for the optimization of the AGILE science performance. In particular, I report on the development of techniques

aimed at improving the angular and spectral resolution in the energy band 30 MeV - 30 GeV, and the development of techniques for the rejection of the particle background, an essential step in order to detect the diffuse gamma-ray emission of the Galaxy.



# Chapter 1

## Gamma-Ray Emissivity of the Interstellar Medium

The interstellar medium of our Galaxy is the most intense source of the gamma-ray sky, producing about 80% of observable photons with energy larger than few tens of MeV (as clearly shown in fig. 1.1). Early observations of the gamma diffuse radiation along the Galactic plane were obtained through the gamma counter mounted on-board of the OSO-3 satellite [Kraushaar et al., 1972]. The major features of this component were defined by measurements made with the SAS-2 satellite [Fichtel et al., 1975] and the COS-B satellite [Bennett et al., 1977]. These measurements were later refined by the observations performed by the Energetic Gamma Ray Experiment (EGRET) flown on the Compton Gamma-Ray Observatory (CGRO). These observations are currently the most suitable to study the interstellar gamma-ray emission.

For gamma-ray energy larger than a few tens of MeV, the Galaxy is transparent to the radiation (the maximum average thickness of the Galaxy is 1/10 of the radiation length). Therefore, the emission intensity is, at least in first approximation, proportional to the Galaxy thickness crossed by the line of

sight. Hence the Galaxy emission shows a intense ridge of apparent width of about 5 degrees in galactic latitude, outside which the emission intensity is strongly reduced (see Fig 1.2)

In order to understand the galactic diffuse radiation, the knowledge of the diffuse medium components is needed and it is also necessary to make use of information obtained from other wavelengths, particularly the radio band, as well as measurements of the cosmic-ray particles.

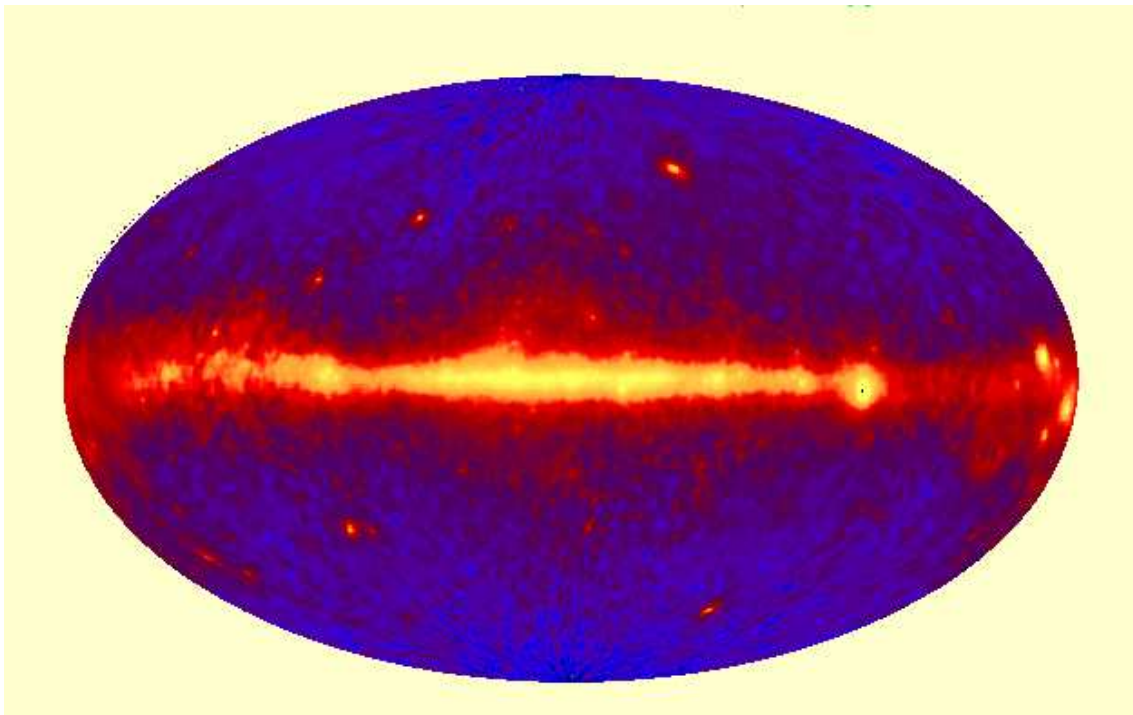


Figure 1.1: The Gamma-Ray sky as observed by EGRET above 100 MeV [Thompson et al., 1993].

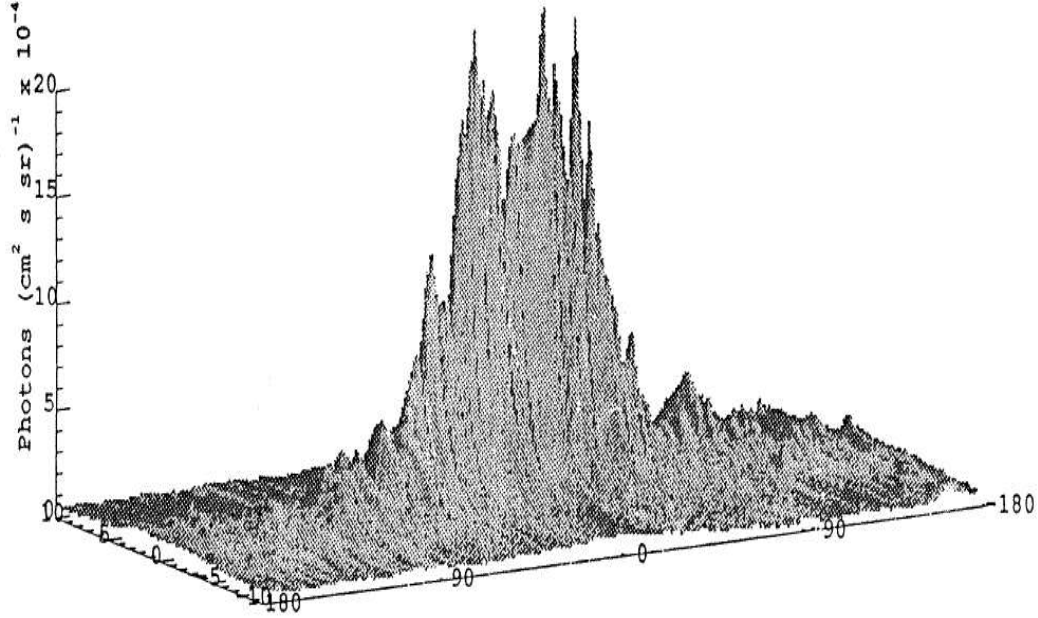


Figure 1.2: The intensity of gamma-ray emission derived from EGRET observations (for energy greater of 100 MeV). The abscissa represents the galactic longitude (degree) while in ordinate is the galactic latitude (degree). It is clearly visible the galactic ridge [Bertsch et al., 1993].

## 1.1 The Interstellar Matter

The interstellar matter is made mainly of Hydrogen and, in smaller measure, Helium and minimal part of heavy elements and dust. At the equilibrium, several phases of interstellar matter with different density and temperature can coexist. Therefore, using a classification based on the Hydrogen atomic states, it is possible to distinguish the *molecular regions* formed from molecular Hydrogen, the *HI regions* in which Hydrogen is neutral, and the *ionized Hydrogen regions HII*.

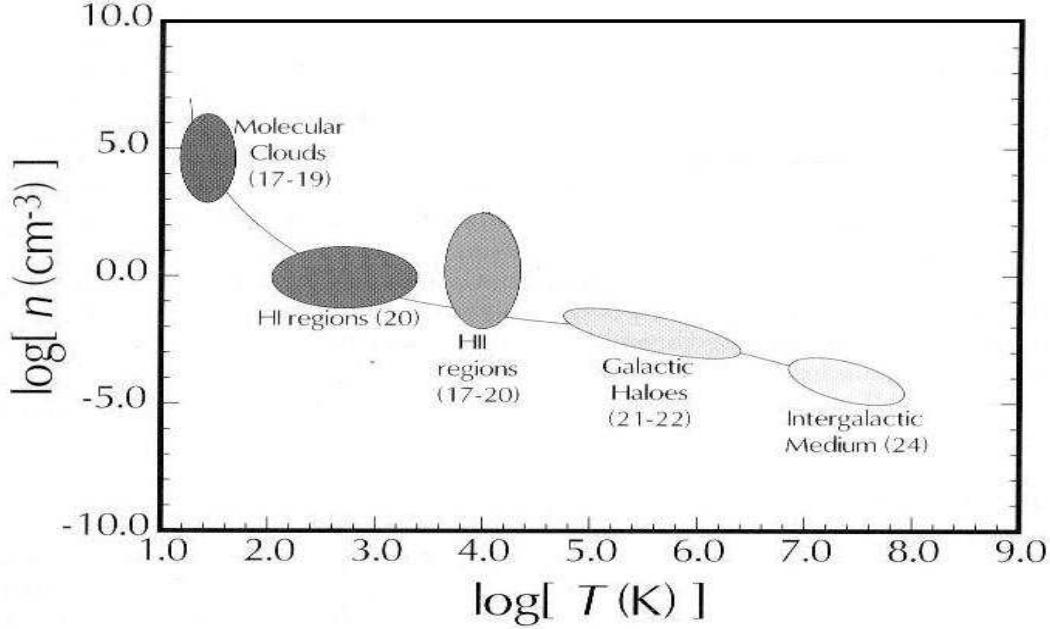


Figure 1.3: Densities and temperatures of the dominant phases of galactic and intergalactic diffuse media. For each class of objects, the characteristic size in log(cm) is given. Figure from [Dopita & Sutherland, 2003]

### 1.1.1 The Molecular Clouds

A large amount of interstellar matter resides in molecular regions, largely concentrated in form of giant clouds of mass  $10^4 - 10^8 M_\odot$  disposed along the spiral arms of the Galaxy. These clouds are concentrations of gas and dust with very high number densities (more than  $10^3 \text{ cm}^{-3}$ ) with respect to the average density of the Galaxy (approximately one atom per  $\text{cm}^3$ ). The presence of a high-density medium and dust makes these regions optically thick to the visible and ultraviolet radiation, allowing the existence of molecular Hydrogen that otherwise would not be possible. In our solar neighborhood, molecular clouds typically have masses of about  $10^5 M_\odot$  and are about 50 pc in diameter.

These entities are self-gravitating and are coupled to the stochastic pressure in the interstellar medium only at their surfaces. The molecular clouds have a relatively small scale thickness, about 120 pc, and they are the birthplace of both the massive and the low-mass stars.

### The 2.6 mm line

The molecule of Hydrogen is homopolar, and therefore it has no electric dipole moment. For this reason it does not emit either vibrational or rotational radiation. The most abundant molecule after  $H_2$  is expected to be carbon monoxide, CO, with emits strong line radiation at 2.6 millimeter, corresponding to the  $J = 0 \rightarrow 1$  rotational transition.

Strong CO radiation has been detected throughout the Galaxy and provides important information about dense molecular regions. The importance of CO observations is that it can be assumed that wherever there are CO molecules there must also exist  $H_2$  molecules, and hence CO is used as a tracer for  $H_2$  molecules. Indeed, the excitation mechanism for the CO molecules is collisions with hydrogen molecules. The CO observations hence provide a measure of the number density of  $H_2$  molecules in these clouds.

### 1.1.2 The Atomic Hydrogen

The atomic phases of interstellar medium of our galaxy can be distinguished into a cold neutral medium and a warm neutral medium. A great part of the mass resides in the cold neutral medium, distributed in dense sheets or filaments (the HI clouds) occupying 1–4% of the total volume of the Galaxy disk.

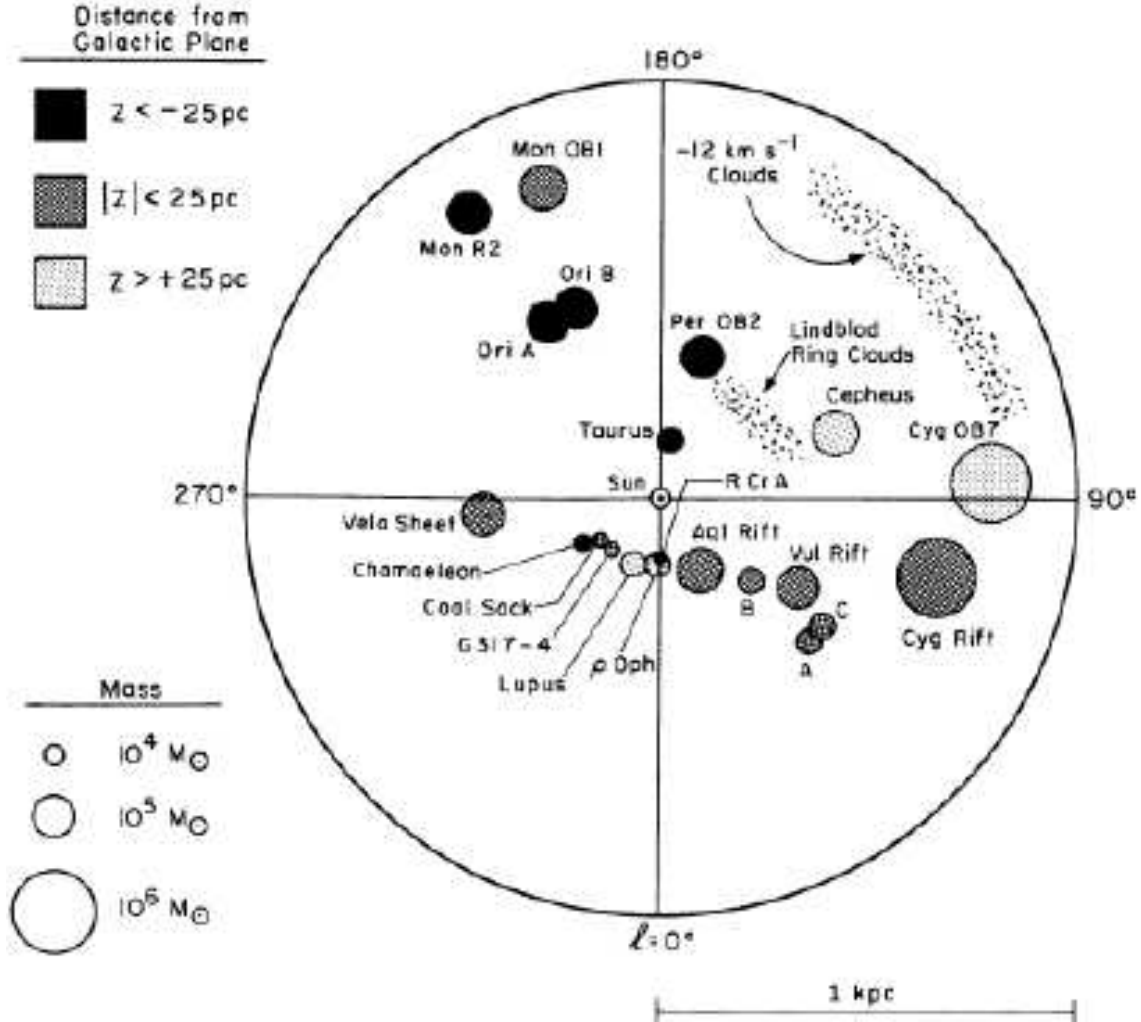


Figure 1.4: Distribution of molecular clouds in the galactic region close to the Sun [Dame et al., 1987].

These clouds, which are not gravitationally bound, have a number density of about  $20 - 60 \text{ cm}^{-3}$  and a temperature of  $\sim 100 \text{ K}$ .

The warm neutral medium fills a substantial fraction ( $\sim 30 - 60\%$ ) of the available volume. This material, located mainly in photodissociation regions, has a density of about  $0.3 - 1 \text{ cm}^{-3}$  and a temperature of  $\sim 6000 \text{ K}$ . These two phases exist in pressure balance with each other, which is a necessary condi-

tion for the existence of a two-phases medium.

### The 21 cm line

Neutral hydrogen is observable at radio frequencies, because its ground level term,  $1^2S_{1/2}$ , is split into two sublevels. This occurs because the electron spin and the proton spin may be either parallel or antiparallel. The electron angular momentum vector ( $J=L+S$ ) can therefore combine in vector addition with the nuclear spin  $I$  to form a total angular momentum vector  $F=J+I$ . Two states  $F=1$  (parallel spins) or  $F=0$  (antiparallel spins) are possible and the second configuration has slightly lower energy than the first, giving two hyperfine levels. The statistical weights of the two levels are 3 and 1 respectively.

The energy separation is due to the interaction between the magnetic field produced by the moving electron and the magnetic moment of the nucleus. The energy difference between the two hyperfine levels is tiny; the transition between the two levels corresponds to a frequency of 1420.40575 MHz or a wavelength of 21.1049 cm. The transition probability is very small ( $A_{21cm} = 2.8710^{-15} s^{-1}$ ), giving a radiative lifetime for the upper level of  $\sim 1.1 \cdot 10^7$  years. The lifetime of the state is so long that natural broadening is negligible, so that, when the line is optically thin, the line profile is determined entirely by kinetic temperature and velocity structure along the line of sight. The population balance between the two hyperfine levels is determined entirely by collisions, so that Boltzmann equilibrium pertains, and the relevant temperature is the spin temperature  $T_S$ . In most cases however, the spin temperature can be taken as the kinetic temperature.

This emission shows a different Doppler shift depending on the zone of the galaxy from which it comes, combining these observations with the rotational curve of the Galaxy it is possible to reconstruct the three-dimensional structure of the Milky Way.

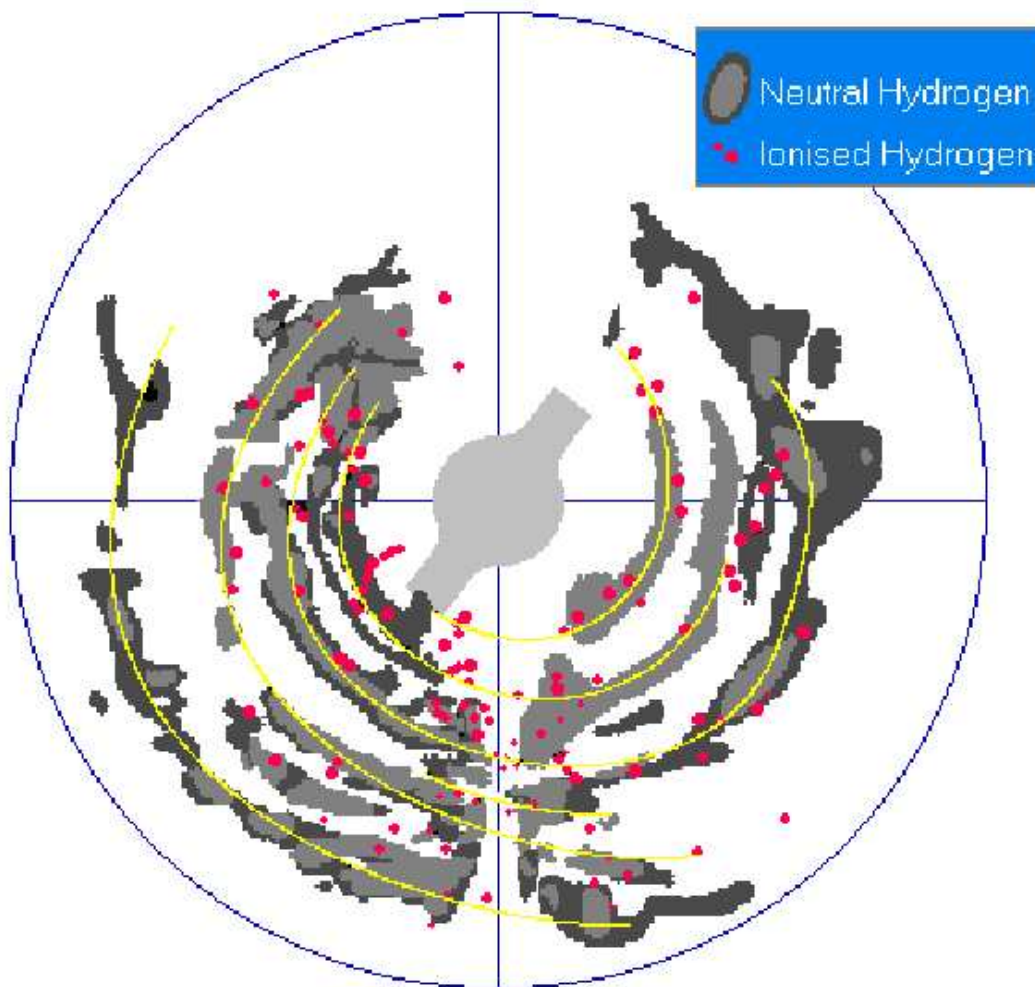


Figure 1.5: Distribution of neutral and ionized regions.

### 1.1.3 The Ionized Hydrogen

The warm phase of the ionized medium is associated with HII regions where it is photoionized by hot young stars. These regions occupy only about 2-4 % of the total interstellar medium volume; they have a density of about  $1 \text{ cm}^{-3}$ , and a temperature of 6000-12000 K. The emission is mainly in the optical and ultraviolet band, due to the recombination lines of the ionized gas. The warm phase has also been detected in regions distant from star-forming regions in both our galaxy and in external galaxies. This material, called “Reynolds layer” in our galaxy, has a temperature of 6000 K and density of  $0.3 \text{ cm}^{-3}$ , and occupies at least 15% of the total volume.

The hot phase of ionized medium has a temperature larger than  $10^6 \text{ K}$  and density less than  $10^{-2} \text{ cm}^{-3}$ . It is heated by strong shocks resulting from supernova explosions or violent stellar winds. Near the midplane of galaxies it has a relatively small filling factor, above the galactic plane its buoyancy encourages it to flow out through galactic chimneys in the denser phase of the interstellar medium, so that it occupies a much larger fraction of the available volume out of the plane. The sun sits in such a hot phase, in a bubble of plasma with a hydrogen density of about  $5 \cdot 10^{-3} \text{ cm}^{-3}$ .

The total mass of the ionized medium is only 0,1% of the total mass of the galaxy.

## 1.2 The Interstellar Radiation Field

Beside the diffuse matter, the interstellar space is filled with the electromagnetic radiation field produced by stars and interstellar matter.

Table 1.1: The five phases of interstellar matter.

Regions		Density ( $cm^{-3}$ )	T (K)	ISM Mass Fraction
<b>Molecular clouds</b>		$10^3$	10 - 30	40-50%
<b>Neutral medium</b>	<b>cold</b>	1-100	80	40-50%
	<b>warm</b>	0.3-1	6000	4-6%
<b>Ionized medium</b>	<b>warm</b>	0.1 - 1	6000-12000	0.1%
	<b>hot</b>	$10^{-2}$	$10^6$	$\sim 0$

*Stellar Contribution.* The radiation field spectrum is dominated by the emission from stars of late spectral classes, which has a large peak in the near infrared, at wavelength of about 1 micron. The energy density of this component has a local value of about  $0.5eV/cm^3$  [Mathis 1983]. A second stellar component, due to stars of class OB, has a peak in the ultraviolet range (at 0.1 micron) but has an energy density lower by about an order of magnitude. Energy density and spectrum of the radiation field show large variation along the Galaxy depending on the distribution of the stars spectral type. In particular, toward the Galactic center an energy density distribution larger by a factor 3-10 and with a softer spectrum is expected.

*Dust Contribution.* Another component of the interstellar radiation field is due to emission in the far infrared of the dust associated with the interstellar matter and heated by absorption of star light. Depending on the temperature, it is possible to distinguish three components [Cox et al., 1986]:

- Cold Dust, with temperature of about 15-25K, is associated to the HI

regions and to the molecular clouds. It may be heated by both old and young stellar population.

- Warm Dust, with temperature of about 30-40K, is associated to HII regions and is heated by stars of spectral class O and B.
- Hot dust, with temperature of about 250-500K is constituted of very small (radius  $\sim 5$  Å) grains heated by general ISRF and normal grains (radius  $\sim 0.1 \mu m$ ) heated by M giants.

This temperature distribution gives rise to a spectrum with a main peak corresponding to a wavelength of 100 micron and to a secondary peak around 10 micron. Even if the dust component is less known, its energy density can be estimated between 0.05 and 0.3 eV ([Mathis 1983] , [Chi & Wolfendale, 1991], [Strong et al., 2000]).

### 1.3 The magnetic field

There is strong evidence that the Milky Way galaxy contains an ordered, large-scale magnetic field of the value of some *microgauss* ( $\mu G$ ). This field configuration has been explored through various methods which include analysis of starlight polarization, modeling pulsar or Faraday rotation, and Zeeman splitting of hydroxyl masers in regions of star formations. The galactic magnetic field can gradually act on the dust particles and cause their rotational axes to line up, therefore their axes are parallel to the direction of the field which is in turn aligned with the Milky Way band and the galactic plane. This

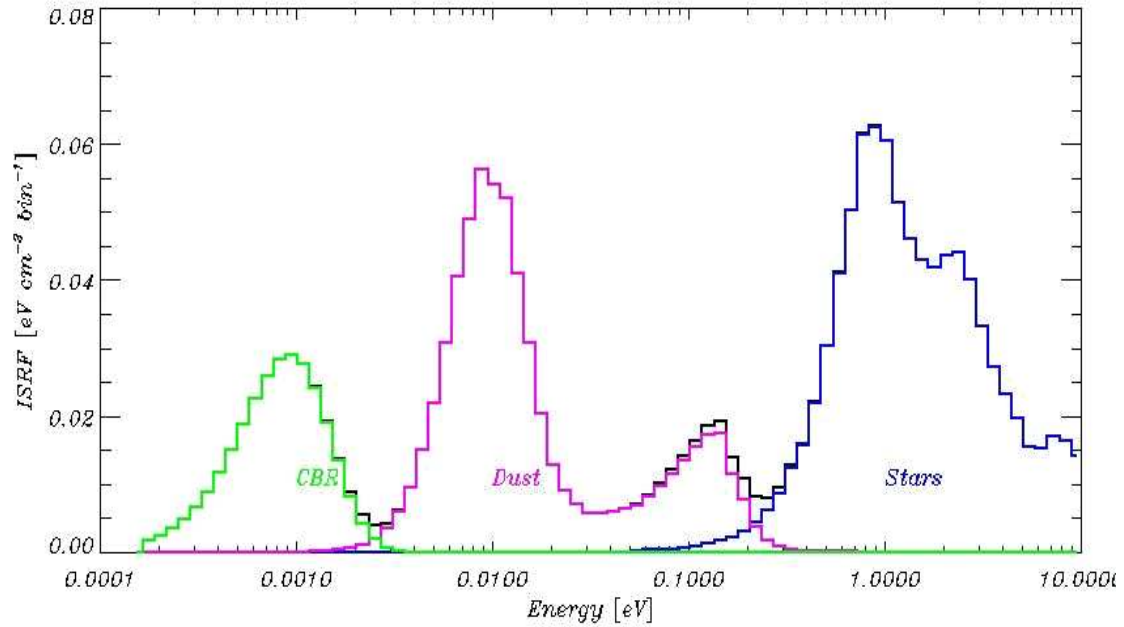


Figure 1.6: The components of the spectrum of the interstellar radiation field. The spectrum of the cosmic background radiation it is also shown. (Adapted from [Strong et al., 2000]).

pattern is confirmed by polarization measurements. The Zeeman splitting of atomic or molecular lines is used to determine the direction and magnitude of a component of the magnetic field in the diffuse and molecular clouds.

## 1.4 Cosmic Rays

Cosmic rays consist of atomic nuclei (mostly H nuclei) and electrons. Positrons and antiproton may also be present. The existence of cosmic rays has been known since the beginning of XX century. Despite the long period since they have been known, many "open questions" on their origin are still without answer.

Cosmic rays may get their energy through the mechanism called "Fermi acceleration", a process in which the particles gain energy by a compressing medium. Shocks in the interstellar medium can generate such a situation. The matter in the pre-shock region and in the post-shock regions acts as magnetic walls. A charged particle on the shock edge sees the two regions of the shock as a compressing system which accelerate the particle.

The gas density jump, in the case of shock, is

$$r = \frac{\gamma + 1}{\gamma - 1 + \frac{2}{M^2}} \quad (1.1)$$

where  $\gamma$  is the adiabatic index and  $M$  is the Mach number. For relativistic particles the energy distribution generated by shock acceleration follows a power law  $f(E) = kE^{-p}$  where  $p$  is:

$$p = \frac{r + 2}{r - 1} \quad (1.2)$$

For very large  $M$  and the usual  $\gamma = 5/3$ ,  $p$  is equal to 2, while for  $\gamma = 4/3$  (typical value for relativistic gas)  $p$  is  $3/2$ .

Radio observations have shown the presence of accelerated electrons inside supernova remnants (SNR), which are therefore identified as the most probable birthplace for the cosmic-ray electronic component. SNR are also supposed to allow for proton and nuclei acceleration, but no evidence has been found until now.

Regardless to their origin, the features of the spatial and spectral distribution of cosmic rays results to depend also on the interaction with the interstellar medium in which they propagate. The interaction with the Galactic magnetic

field cause the cosmic ray diffusion to depend on both the particles energy and the magnetic field irregularities spectrum. Considering a Kolmogorov irregularities spectrum, the particle diffusion outside the Galaxy disk is proportional to  $E^{1/3}$ , which makes cosmic ray spectrum steeper by a factor 1/3.

Cosmic ray interaction with the interstellar medium also causes energy losses, which in turn modify in different way the initial spectrum for electron and proton.

### 1.4.1 Cosmic Electrons

Assuming that the initial spectrum for cosmic ray electrons can be represented by a power law:

$$Q = kE^{-p}[\text{electrons}/\text{cm}^2 \text{ sec eV sr}] \quad (1.3)$$

the spectrum evolution follows the law :

$$\frac{dN}{dt} = D\nabla^2 N + \frac{\partial}{\partial E} [b(E)N(E)] + Q(E) \quad (1.4)$$

where D is the diffusion coefficient and :

$$b(E) = -\frac{dE}{dt} \quad (1.5)$$

Equation 1.4 can be resolved in first approximation by ignoring the terms due to diffusion (assuming e.g. a uniform sources distribution) and  $\partial N/\partial t$  we obtain

$$\frac{\partial}{\partial E} [b(E)N(E)] = -Q(E) = -kE^{-p} \quad (1.6)$$

and integrating :

$$N(E) = \frac{kE^{-(p-1)}}{(p-1)b(E)} \quad (1.7)$$

The shape of the initial particle ( $e^-$ ) spectrum is therefore modified according to the dependence of  $b$  on  $E$ . The energy loss can be due to:

- **Synchrotron losses:** due to the interaction of electrons with the galactic magnetic field and producing a radio emission detectable in the MHz range. This energy loss is proportional to the magnetic field energy density and to the square of the electron Lorentz factor. For this reason the effect on  $N(E)$  is especially important above a critical energy  $E_s^*$ , causing, for  $E > E_s^*$ ,  $N(E)$  to become steeper and proportional to  $E^{-(p+1)}$
- **Inverse Compton losses:** they are due to the interaction with the interstellar radiation field and with the cosmic background radiation and produce emission in the gamma ray range (see par 1.5.3). As the synchrotron losses, they are proportional to the square of the electrons Lorentz factor and dominate at high energy. Also in this case the photon spectrum becomes proportional to  $E^{-(p+1)}$  above a critical energy  $E_{ic}^*$ .
- **Bremsstrahlung losses:** they are due to interaction with the atomic nuclei of the interstellar matter and produce gamma emission (see par.

1.5.2). They are proportional to the electron energy and do not cause a change in the electron spectral shape.

- **Ionization losses:** they are due to interaction with interstellar matter atoms. They have a slight dependence on the electrons energy and the spectrum become proportional to  $E^{-(p-1)}$

The radio observation of the synchrotron diffuse emission cover the range between few tens of MHz to a few GHz. These observations show a radiation spectrum with index  $\beta$  between 2.4 and 3, which corresponds to a spectral index of the electron flux  $\alpha$  between 2 and 3. In particular an increase of  $\beta$  from 2.4-2.6 to 2.8-3 is observed for frequency larger than 400 MHz [Strong et al., 2000]. This can be connected to the spectral break due to synchrotron and inverse Compton energy losses, as is foreseen for electron spectrum at energy of about few GeV.

The spectrum of cosmic electrons can also be obtained from the direct measurements performed at the top of the atmosphere, for energies larger than some GeV, where the solar modulation is not important. Recent measurements found that the local electron spectrum can be fitted by a single power-law, with index 3.4, up to 2-3 GeV [Casadei & Bindi, 2004].

However the electron distribution is expected to be very inhomogeneous for energies above some tens of GeV, as more energetic electrons are confined close to the sources [Strong et al., 2000], [Pohl & Esposito, 1998]. This suggests that the spectrum of cosmic electrons can be different from that measured locally.

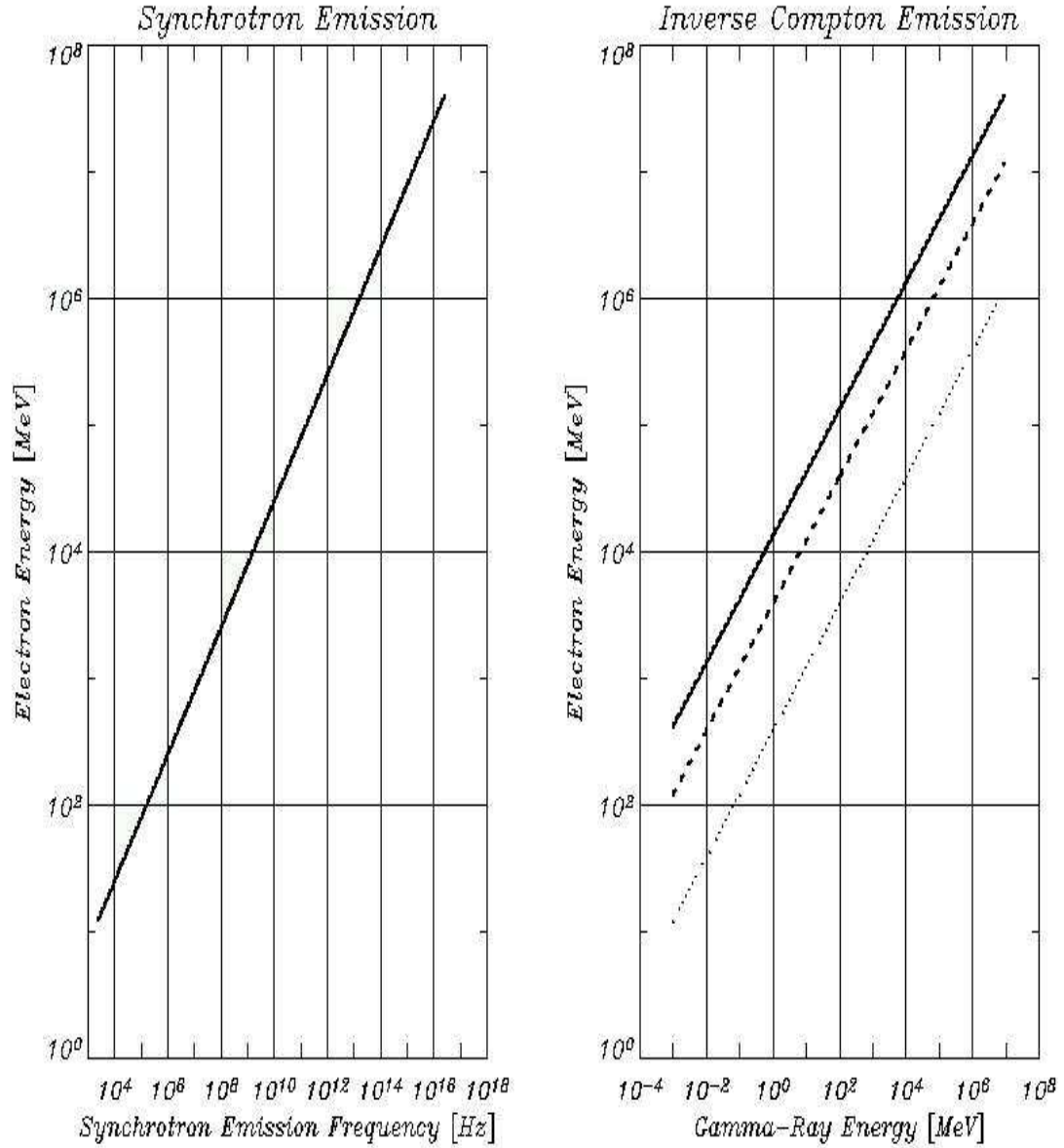


Figure 1.7: Left: Relation between electron energy and frequency of the emitted synchrotron radiation, (a value of galactic magnetic field of  $6 \mu G$  has been assumed). Right: Relation between electron energy and energy of the emitted inverse-Compton radiation, for the stellar radiation field (dotted line), the dust radiation field (dashed line) and the cosmic microwave background (solid line)

### 1.4.2 Cosmic Protons

Unlike electrons, proton interactions with interstellar medium produce a negligible energy loss. The most important physical processes which cosmic protons undergo (beside the interaction with the magnetic field described above) are ionization of the interstellar medium and inelastic scattering with atomic nuclei of the ISM. The latter produce gamma radiation (see par 1.5.1), which is the only observable radiation emission produced by cosmic proton. Observation of galactic gamma diffuse emission are therefore fundamental in order to obtain the proton galactic distribution. In particular, gamma observations of our Galaxy and of the Magellanic Clouds performed by EGRET demonstrate the galactic origin of the cosmic rays, at least for energies up to few hundreds of TeV [Sreekumar, 1993]. The proton spectrum is believed to be less dependent on the position where it has been measured, unlike that of electrons, and therefore local measurements of cosmic rays can be considered more similar to the average galactic spectrum. The measured cosmic proton flux shows a spectrum with a constant index of 2.75 over six orders of magnitude and with an energy ranging between a few GeV (below this energy the effect of the solar magnetic field on the observed fluxes is dominant) and  $10^{15}$  eV. At this energy a steeping of the spectrum is observed (known as “cosmic-ray knee”) and the spectral index is about 3.3 This behavior is maintained up to energy of about  $10^{17}$  eV above which the spectral index is again about 2.7 (“cosmic-ray ankle”). The latter value of the spectral index remains constant up to the highest energy measured up to now ( $3 \cdot 10^{20}$  eV) [Biermann & Sigl, 2001]. The “cosmic-ray knee” at  $10^{15}$  eV is typically understood in terms of disappearing of the galactic cosmic ray component and appearing of an extragalactic contri-

bution. For energy larger than  $10^{17}$  eV, protons interact with infrared photons of the cosmic background radiation. This process, known as GKZ effect, is supposed to cause the “ankle” in the spectrum and the disappearing of the protons for energy larger than  $10^{20}$  eV .

## 1.5 The physical processes producing gamma-ray emissivity

### 1.5.1 Proton-Proton collisions

In collisions between high energy protons and nuclei, pions of all charges,  $\pi^+$ ,  $\pi^-$  and  $\pi^0$  are produced as secondaries.  $\pi^+$  and  $\pi^-$  generate electrons and positrons, while the neutral  $\pi$  decays in a pair of gamma photons. The energy of the emitted gamma is, in the reference frame of the  $\pi^0$ , half of the  $\pi^0$  rest mass, and therefore the observed energy of the gamma ray depends on the momentum of  $\pi^0$  respect to the observer. If  $f_p$  is the spectra of protons

$$f_p = \frac{dN_p}{dA dt d\Omega dE_p} \left[ \frac{\text{proton}}{cm^2 sec sr MeV} \right] \quad (1.8)$$

the  $\pi$  emissivity per hydrogen atom is :

$$q_\pi(E_\pi) = 4\pi\sigma_{pi}(E_p)f_p(E_p)\frac{1}{k_\pi} \left[ \frac{\pi}{sec MeV H} \right] \quad (1.9)$$

where  $E_\pi$  is the energy of the emitted pion,  $E_p$  is the energy of the proton,  $\sigma_\pi$  is the cross section for  $\pi$  production through proton-proton collision (see par. 1.5.1).  $k_\pi$  is the mean fraction of proton kinetic energy transferred to the neutral pion, and is about 0.17 [Mori, 1997].  $E_\pi$  and  $E_p$  then are related by:

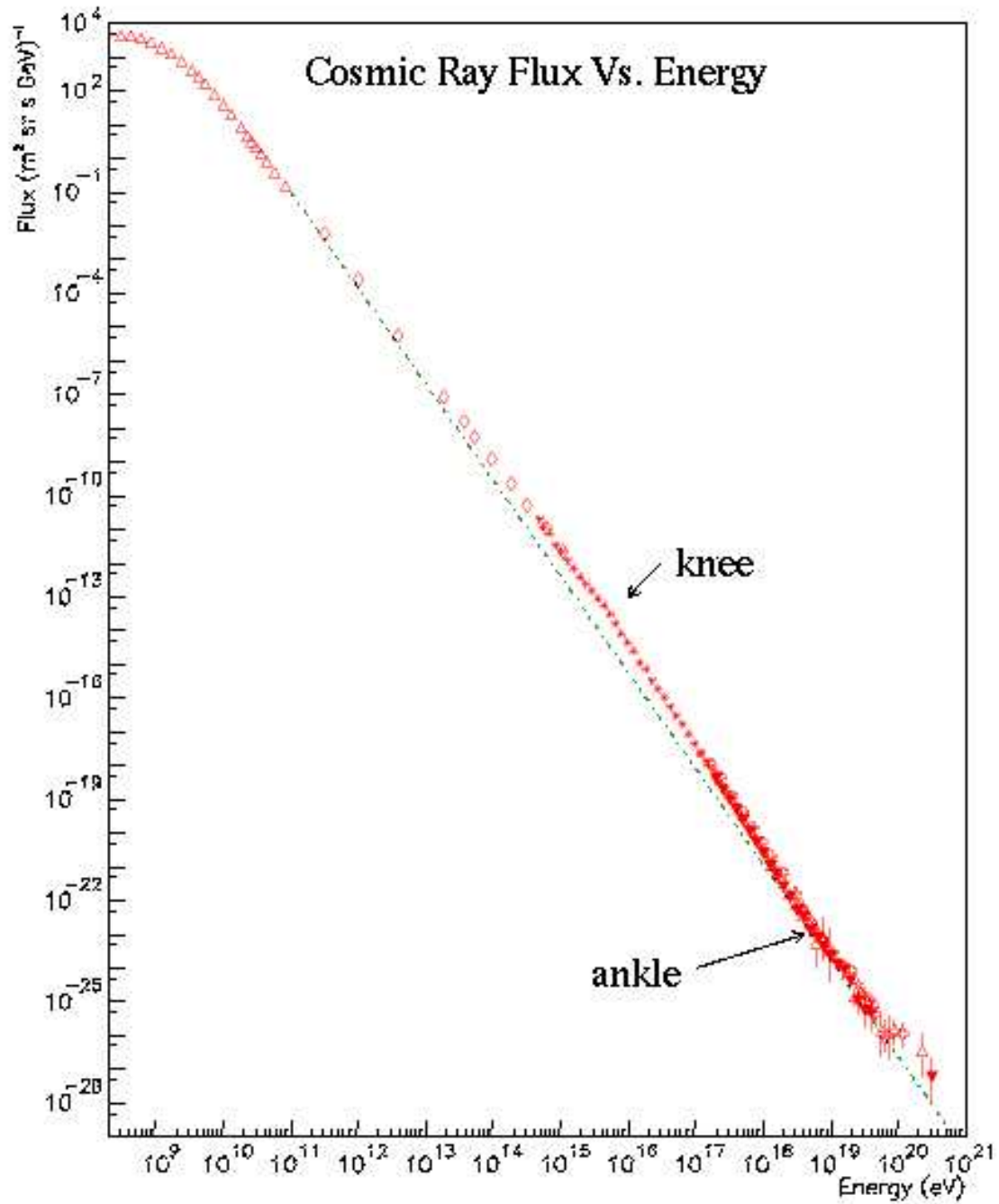


Figure 1.8: Spectrum of the local proton flux.

$$E_\pi = \frac{E_p - m_p c^2}{K_\pi} \quad (1.10)$$

$m_p$  is the proton rest mass. The gamma-ray emissivity results to be:

$$q_\gamma(E_\gamma) = 2 \int_{E_{min}}^{\inf} \frac{q_\pi(E_\pi)}{p_\pi c} dE_\pi \left[ \frac{ph}{sec \text{ MeV } H} \right] \quad (1.11)$$

where  $E_\gamma$  is the photon observed energy,  $p_\pi$  is the pion momentum and  $E_{min}$  is the minimal energy necessary for a pion to create a photon of energy  $E_\gamma$  (in the observer reference system):

$$E_{min} = E_\gamma + \frac{m_\pi^2 c^4}{4E_\gamma} \quad (1.12)$$

where  $m_\pi$  is the neutral pion rest mass. The emissivity per unit volume of interstellar matter is then:

$$g_{pp} = q_\gamma n_H \left[ \frac{ph}{cm^3 \text{ sec MeV}} \right] \quad (1.13)$$

where  $n_H$  is the density of H atom (both atomic and molecular).

### **The $\pi^0$ cross section**

Although the cross section of the  $\pi$  production for pp collision is fundamental to estimate the interstellar gamma-ray emissivity its value is not yet well known. Its value is zero for kinetic energy less than 300 MeV the (threshold energy) and about 30 mbarn for kinetic energy more than 2 GeV . In the energy range  $300 \text{ MeV} < E_{kin} < 2 \text{ GeV}$  the cross section increase rapidly. A good fit of the experimental data is given by [Dermer, 1986b].

$$\sigma_{\pi} = \begin{cases} 32.6(p_p - 0.8)^{3.21} & p_p < 1.27 \\ 5.4(p_p - 0.8) & 1.27 < p_p < 8 \\ 32 \ln(p_p) + \frac{48.5}{\sqrt{p_p}} - 59.5 & p_p > 8 \end{cases} \quad (1.14)$$

where  $p_p$  is the proton momentum.

Nevertheless, it is important to notice that this is an assumption in the gamma-ray pp emissivity calculation, small variations in the cross section in the  $300 \text{ MeV} < E_{kin} < 2 \text{ GeV}$  range can lead to different results for gamma-ray spectrum with energy between about 50 MeV and 90 MeV.

In order to take into account the effect of heavier nuclei than protons in cosmic rays and the interstellar matter, we have use a constant multiplication factor independent of energy of value 1.5. This is a reasonable approximation, at least for energy less than 100 GeV per nucleon [Mori, 1997].

### 1.5.2 Electron Bremsstrahlung

If  $f_e$  is the energy spectrum of cosmic electrons in units of  $particle/cm^2 \text{ sec sr MeV}$ , the photons of energy  $E_{\gamma}$  produced by electrons of energy  $E_e$  are:

$$\begin{aligned} dN_{\gamma}(E_e, E_{\gamma}) &= 4\pi\sigma(E_{\gamma}, E_e)f(E_e)n_H dE_{\gamma}dE_e = \\ &= \frac{4\pi n_H}{x_0 E_{\gamma}} f(E_e) dE_{\gamma}dE_e \end{aligned} \quad (1.15)$$

where we used:

$$\sigma(E_{\gamma}, E_e) = \frac{1}{x_0 E_{\gamma}} \quad (1.16)$$

with :

$$x_0 = \frac{1}{4\alpha r_e^2 G_a} \quad (1.17)$$

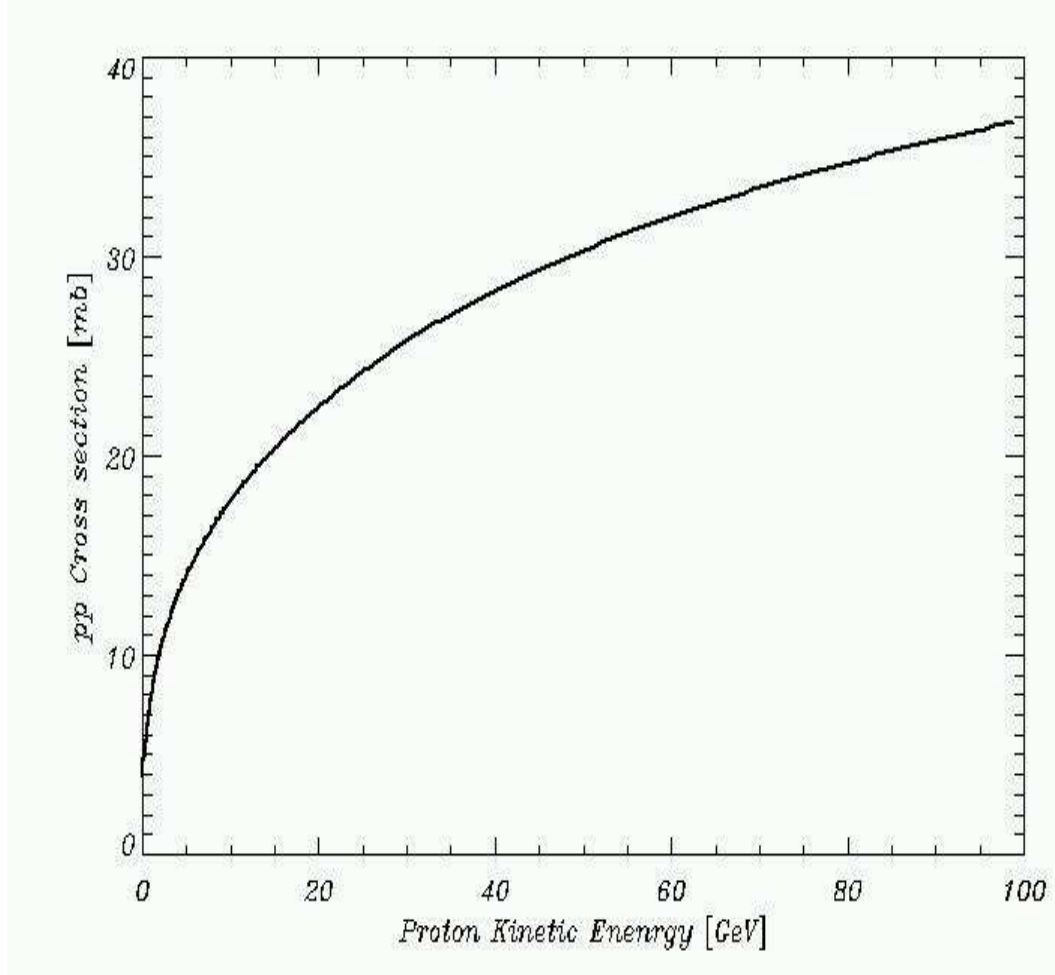


Figure 1.9: Cross section of neutral pion production through proton-proton collision [Dermer, 1986b].

$\alpha$  is the constant of fine structure,  $r_e$  is the classical electron radius. The Gaunt factor  $G_a$  for bare nuclei is:

$$G_a = \ln(2\gamma) - \frac{1}{3}$$

and for neutral atoms is:

$$G_a = \ln\left(\frac{183}{Z^{1/3}}\right) - \frac{1}{18}$$

The Bremsstrahlung gamma-ray emissivity of interstellar matter is therefore:

$$g_{br} = \frac{4\pi n_H}{x_0 E_\gamma} \quad (1.18)$$

The radiation lost by Bremsstrahlung of a relativistic electron of energy  $E_e$  moving through a medium formed by Hydrogen atoms is :

$$I(\omega) = \frac{e^6 N}{16\pi^3 \epsilon_0^3 c^4 m_e^2} G_a = 4c\hbar\alpha r_e^2 N G_a \quad (1.19)$$

It shows a flat energy spectrum up to energy  $\omega = E_e/\hbar$ . The photon spectrum is then:

$$n_\gamma(\hbar\omega) = \frac{4c\alpha r_e^2 N}{\hbar\omega} G_a \quad (1.20)$$

The integration of the (1.19) on  $\omega$  leads to the energy emitted (therefore lost) by the electron :

$$-\frac{dE}{dt} = 4c\alpha r_e^2 N G_a E \quad (1.21)$$

For a distribution of electrons with spectrum  $N_e(E) = kE^{-a}$  we get:

$$I(\hbar\omega) = 4Z^2 c\alpha r_e^2 N G_a k \frac{(\hbar\omega)^{-a}}{a-1} \quad (1.22)$$

Therefore the index of photon spectrum of electron spectrum have the same value.

### 1.5.3 Inverse Compton

The energy of a gamma photon produced via inverse Compton by an electron of energy  $E_e$  and a photon of energy  $E_{ph}$  is:

$$E_\gamma = \frac{4}{3} \left( \frac{E_e}{m_e c^2} \right)^2 E_{ph} \quad (1.23)$$

The cross section of the reaction is the Thompson cross section ( $\sigma_t$ ). The inverse-Compton gamma-ray emissivity of interstellar matter is therefore:

$$g_{IC}(E_\gamma) dE_\gamma = 4\pi\sigma_t \frac{U_{ph}}{E_{ph}} f(E_e) dE_e \quad (1.24)$$

where  $U_{ph}$  is the energy density of the radiation field of photons of energy  $E_{ph}$ . By integrating:

$$g_{IC}(E > E_\gamma) = 4\pi\sigma_t \frac{U_{ph}}{E_{ph}} \int_{E_e}^{\text{inf}} f(E'_e) dE'_e \quad (1.25)$$

where  $E_\gamma$ ,  $E_{ph}$  and  $E_e$  are related by eq. 1.23. For a distribution of electrons with spectrum  $N_e(E) = kE^{-a}$ , from eq 1.24  $g_{IC}$  become:

$$\begin{aligned} g_{IC}(E_\gamma) &= 4\pi\sigma_t \frac{U_{ph}}{E_{ph}} f(E_e) \frac{dE_e}{dE_\gamma} = \\ &= \frac{8\pi\sigma_t}{3} k (m_e c^2)^{1-a} \left( \frac{3}{4E_{ph}} \right)^{\frac{3-a}{2}} E_\gamma^{-\frac{a+1}{2}} \end{aligned} \quad (1.26)$$

Therefore the spectrum of produced photons is still a power law, with index  $\frac{a+1}{2}$



## Chapter 2

# Modeling the Gamma-Ray Emission of the Galaxy

A model of interstellar gamma-ray emissivity is important for two main reasons. First, the model can help our understanding of gamma-ray emission from the interstellar medium, which is a probe for the study of cosmic rays (distribution, propagation, sources, ..) and for the mapping of the interstellar matter and radiation field. The second reason is that the galactic diffuse gamma-ray emission represents a background over which the point like sources are seen. A detailed modelization of this component is therefore necessary also for the analysis of the gamma-ray point sources.

### 2.1 The EGRET observations and the EGRET diffuse emission model

In the years between 1991 and 2000, the EGRET instrument performed observations in the gamma band, in the energy range from 30 MeV to 10 GeV. EGRET observations covered the whole sky, providing data on Galaxy emis-

sion, both in the plane and at high latitudes.

These observations have demonstrated the correlation between the galactic structures (arm - interarm regions) and the gamma emission, thus confirming the model of gamma emission based on the interaction between cosmic rays and interstellar medium. A further relevant result of EGRET observations on diffuse emission is the demonstration of the galactic origin of cosmic rays (at least for energy smaller than  $10^{15} \text{eV}$ ). The flux of gamma-rays from the Large Magellanic Cloud is consistent with a cosmic ray density similar to that of Milky Way, while the upper limit for the Small Magellanic Cloud implies a cosmic ray density several times less [Sreekumar, 1993].

The EGRET galactic diffuse emission model is a 3D grid of gamma-ray emissivity of the Galaxy, centered on the Sun with coordinates given by galactic longitude, galactic latitude and distance along the line of sight [Bertsch et al., 1993], [Hunter et al., 1997]. The bin size of this matrix is  $0.5^\circ$  for longitude and latitude and 0.5 kpc for radial distance. The cosmic ray model used to derive the gamma emissivity assumes that cosmic rays have the same energy spectrum as the local one [Skibo, 1993]. Also the ratio between protons and electrons fluxes is assumed to be equal to the local value. The normalization of the cosmic-ray energy spectrum is instead dependent on position: it is assumed that the cosmic-ray intensity is proportional to the matter surface density in the Galaxy.

The atomic hydrogen distribution is derived mainly from the 21 cm galactic plane survey of Weaver and Williams (1973) and the Maryland-Parkes southern survey [Kerr et al., 1986], while the molecular clouds distribution is obtained from the “superbeam” survey [Dame et al., 1987]. These radio data

were the best ones available when the EGRET model was made.

The good agreement of this model with the results of EGRET observations demonstrates that the computation of gamma-ray emissivity based on proton-proton and Bremsstrahlung interaction of cosmic ray on interstellar matter and on inverse Compton interaction on interstellar radiation field can reproduce quite well the observed diffuse-emission features (spectrum and spatial distribution), also at the level of single molecular clouds systems [Hunter et al., 1994], [Digel et al., 1996], [Digel et al., 1999] and [Digel et al., 2001].

## 2.2 Beyond the EGRET model

Several questions about the correct modeling of the interstellar medium gamma-ray emissivity are still open. The measured spectrum appear to have a 40% of excess with respect to the theoretical prediction for energy above 1 GeV [Hunter et al., 1997]. Many hypothesis have been proposed to solve this problem. Most theories explain this feature assuming that the galactic cosmic ray spectrum is on average different from that obtained from local measurements. Pohl & Esposito showed that the energy losses suffered by high energy electrons imply that these electrons are confined in regions close to their sources [Pohl & Esposito, 1998]. This would imply that the spectrum is highly inhomogeneous (both in space and in time) and therefore the local spectrum cannot be assumed as representative of the whole Galaxy. Moreover, according to this model, electrons would have a spectrum on average harder than the local spectrum. This would increase the contribution due to inverse Compton and would explain the event excess for gamma-ray energy above 1 GeV.

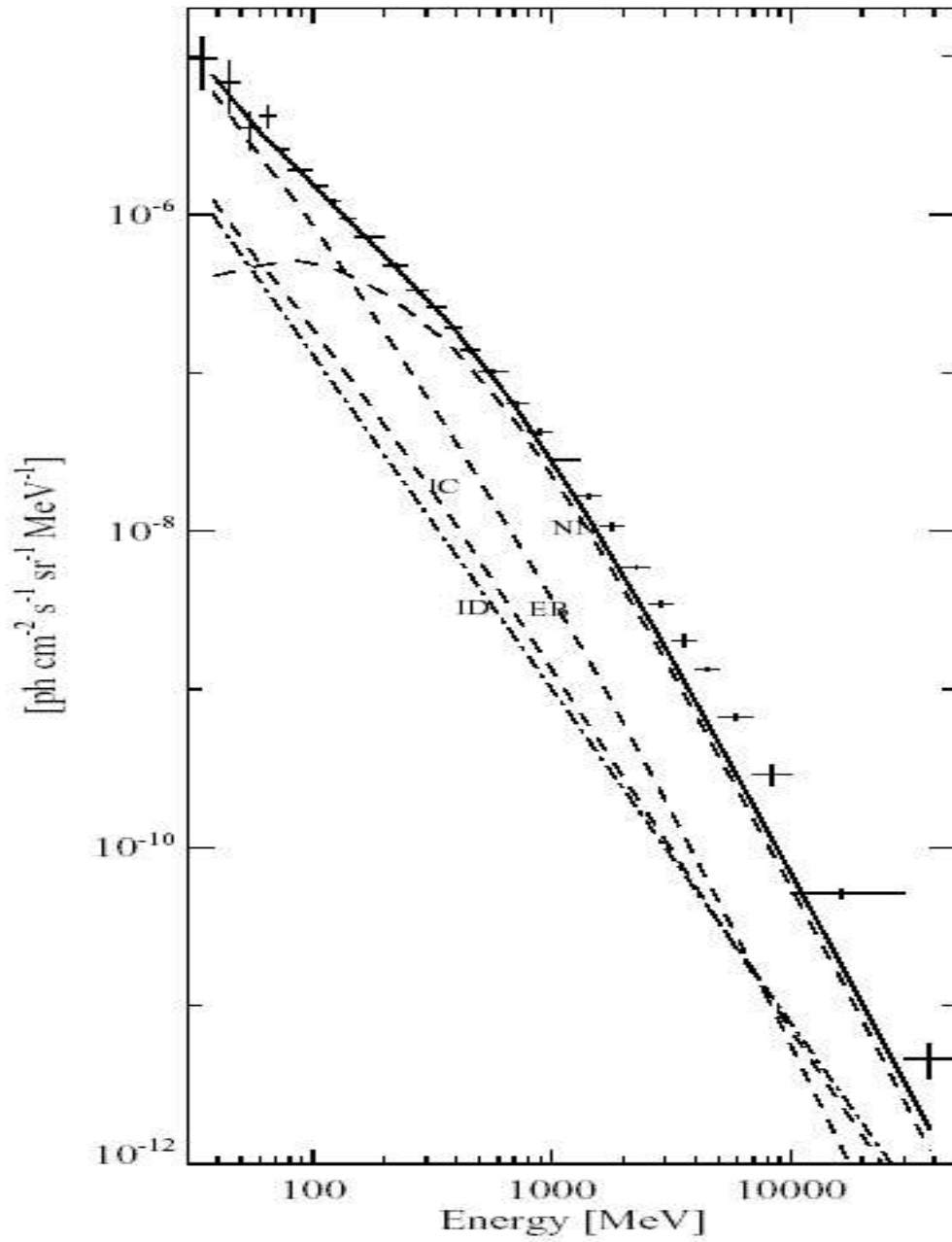


Figure 2.1: Spectrum of the inner Galaxy ( $|l| < 60^\circ$ ,  $|b| < 10^\circ$ ) with calculated components from bremsstrahlung (EB), inverse Compton (IC),  $\pi^0$  decay (NN), and extragalactic isotropic emission (ID) [Hunter et al., 1997].

Other models, instead, link the excess of diffuse radiation to the hadronic component of cosmic rays. Mori has calculated the gamma emission due to proton-proton interactions using numeric simulation based on the Monte Carlo method [Mori, 1997]. This work confirmed the results obtained when the production of secondary pions is evaluated in a simpler way [Dermer, 1986a]. He concluded that a harder proton spectrum (with spectral index 2.4 - 2.5) would explain, at least in part, the excess measured at high energies. A model able to reproduce the whole spectrum of diffuse emission of the inner Galaxy in the full range between 10 keV and 100 TeV is presented in [Aharonian & Atoyan, 2000]. In this model the excess at GeV is reproduced by summing to the contribution due to electron inverse Compton emission, the  $\pi^0$  decay emission produced by protons with a quite flat (spectral index 2.1) energy distribution and with a break around 10 GeV. Busching et al., 2001 show that a spectrum of Galactic protons on average harder than the local spectrum can be explained by assuming a dispersion of the spectrum index of injection for nucleons accelerated by supernova remnants. In [Strong et al., 2000] a study of several possible scenarios, in which both the electrons and protons spectra are modified, is presented also taking in consideration the local measure of atomic abundance in cosmic rays, of secondaries (as antiprotons and positrons) and of synchrotron emission. From this study one can deduce that changing only the proton spectrum would produce a rate of antiprotons and positrons not compatible with the measurements. On the contrary, taking a proton spectrum consistent with the limits imposed by secondaries measurements and a harder spectrum for electrons (injection index 1.9), it is possible to reproduce the GeV excess and to fit the radio observations of synchrotron

radiation. [Strong et al., 2004a] proposed a model that assumes an electron and a proton spectrum slightly harder than the local ones (electrons injection index 1.5 below rigidity 20 GV and 2.42 above and the same indexes for protons but with the break at rigidity 10 GV). This model can fit the observations in the radio and gamma bands as well as the primary and secondary cosmic rays abundances. Other works propose that the excess is caused by non resolved sources with a harder spectrum than that of diffuse emission, as supernova remnants [Berezhko & Völk, 2000] or pulsars [Pohl et al., 1997]. In [De Boer et al., 2004] the excess is interpreted as WIMP annihilation emission coming from a dark matter halo and disk.

Finally we cannot exclude that the theoretical knowledge about gamma-ray emission due to hadronic component of cosmic rays needs to be improved.

Beside the GeV excess other problems are still waiting for a solution. For example, the gradient of diffuse emission in galactic longitude is significantly different from the gradient derived from supernova remnants, which are assumed to be cosmic-ray sources. This discrepancy could be linked to propagation effects of cosmic rays. In particular, it can be supposed either that the thickness of the Galactic halo in which the cosmic rays are confined is a function of the distance from the center of Galaxy [Breitschwerdt et al., 2002] or that the propagation is deeply affected by turbulence of interstellar medium [Erlykin & Wolfendale, 2002]. Another possibility is that the factor  $X$  (which is used to derive the  $H_2$  density from CO emission intensity) has a strong gradient along the distance from the Galactic center (about an order of magnitude from 0 to 10 kpc) [Strong et al., 2004b].

Due to the poor angular resolution of previous missions it is not possible to

know how the observed diffuse emission is contaminated by the presence of unresolved sources. Many Galactic sources of gamma rays have been proposed as possible contributors to the diffuse emission, as, pulsars [Pohl et al., 1997], supernova remnants [Berezhko & Völk, 2000] or molecular clouds [Aharonian, 1991].

## 2.3 The AGILE diffuse gamma-ray emission model

The AGILE diffuse gamma-ray emission model is a 3D grid with bins of  $0.25^\circ$  in galactic longitude and latitude and 0.2 kpc in distance along the line of sight. The gamma-ray emissivity is supposed to be produced by the interaction of cosmic rays with the interstellar medium through these physical processes: (1) protons interacting with the interstellar-medium nuclei (pp scattering) and producing  $\pi^0$  which in turn decay in a gamma-ray pair. (2) Electrons interacting with the diffuse matter by Bremsstrahlung and with the interstellar radiation field by inverse Compton scattering.

Therefore, to build a gamma-ray emissivity map of the Galaxy it is necessary to know the 3D distribution both of cosmic rays and of cosmic-ray targets, namely the interstellar matter, given mainly by atomic hydrogen and molecular clouds, and the interstellar radiation field. The distributions of the interstellar diffuse matter determine the spatial features of the gamma-ray emissivity model at small angular scale. The spectrum of the gamma emissivity is instead mainly determined by the cosmic rays model assumed (even if the ratio between the diffuse matter density and the interstellar radiation field can influence the spectrum at high energy). The spatial variation at large

scale, instead, depend both on the cosmic ray model and on the cosmic rays target distribution.

In order to model the Galaxy matter distribution we use the HI and CO radio surveys recently terminated (described in section 2.8) which are more accurate than those used in previous works (as for the EGRET model, or [Pohl & Esposito, 1998], or [Strong et al., 2000]). These new radio data allow to derive a matter distribution with a finer angular resolution; moreover, the good sensitivity of the new surveys allows mapping the Galaxy up to large distances.

For the cosmic-ray model we have used the results of the GALPROP code (with the hard electron spectrum described in [Strong et al., 2000]), which is able to reproduce the GeV-excess.

It is convenient to express the interstellar-medium gamma-ray emissivity  $g(l, b, r, E)$  by separating the terms depending on the cosmic rays from those related to their target density.

$$g(l, b, r, E) = [q_{pp}(l, b, r, E) + q_{br}(l, b, r, E)][n_{H_2}(l, b, r) + n_{HI}(l, b, r)] + \quad (2.1) \\ + q_{iC}(l, b, r, E)n_{ph}(l, b, r)$$

where  $q_{pp}$  and  $q_{br}$  are the gamma-ray emissivity per hydrogen atom due to either pp scattering or Bremsstrahlung, while  $q_{iC}$  is the gamma emissivity per target photon due to inverse Compton.  $n_{HI}$ ,  $n_{H_2}$  and  $n_{ph}$  are, respectively, the density of molecular hydrogen, the density of atomic hydrogen and the density of ISRF photons.

## 2.4 Mapping the matter distribution in the Galaxy

Radio emission from the interstellar matter is dominated by emission lines of its constituents. The width of these lines, which are shifted by the Doppler effect, depends on both temperature and turbulence existing in the emitting clouds. Due to the optimal spectral resolution of radio receivers, the observation of lines at radio wavelengths allows to resolve the Doppler shift and to measure the radial velocity of the emitting matter. It is therefore possible to produce sky survey in which, for every direction, the emission is given as a function of the radial velocity with which the line is observed. The data cubes produced in this way are usually called *velocity-resolved surveys*. Velocity-resolved radio data, as for example the 21 cm survey, have proved to be a very important tool for studying the gas distribution in the spiral arms of our galaxy.

These surveys are very important because they allow to obtain a three-dimensional distribution of the medium which has generated the observed emission.

The galactic disk indeed rotates differentially and this produces Doppler shifts in the observed spectral lines emitted from gas at different distances from the galactic center than the Sun. This is illustrated in fig 2.2. Once we measure the Doppler shift we can deduce the net velocity  $\Delta v$

$$\Delta v = v - v_0 = \Omega(R)R\sin(l) - \Omega(R_0)R_0\sin(\lambda) \quad (2.2)$$

but (see figure 2.3)

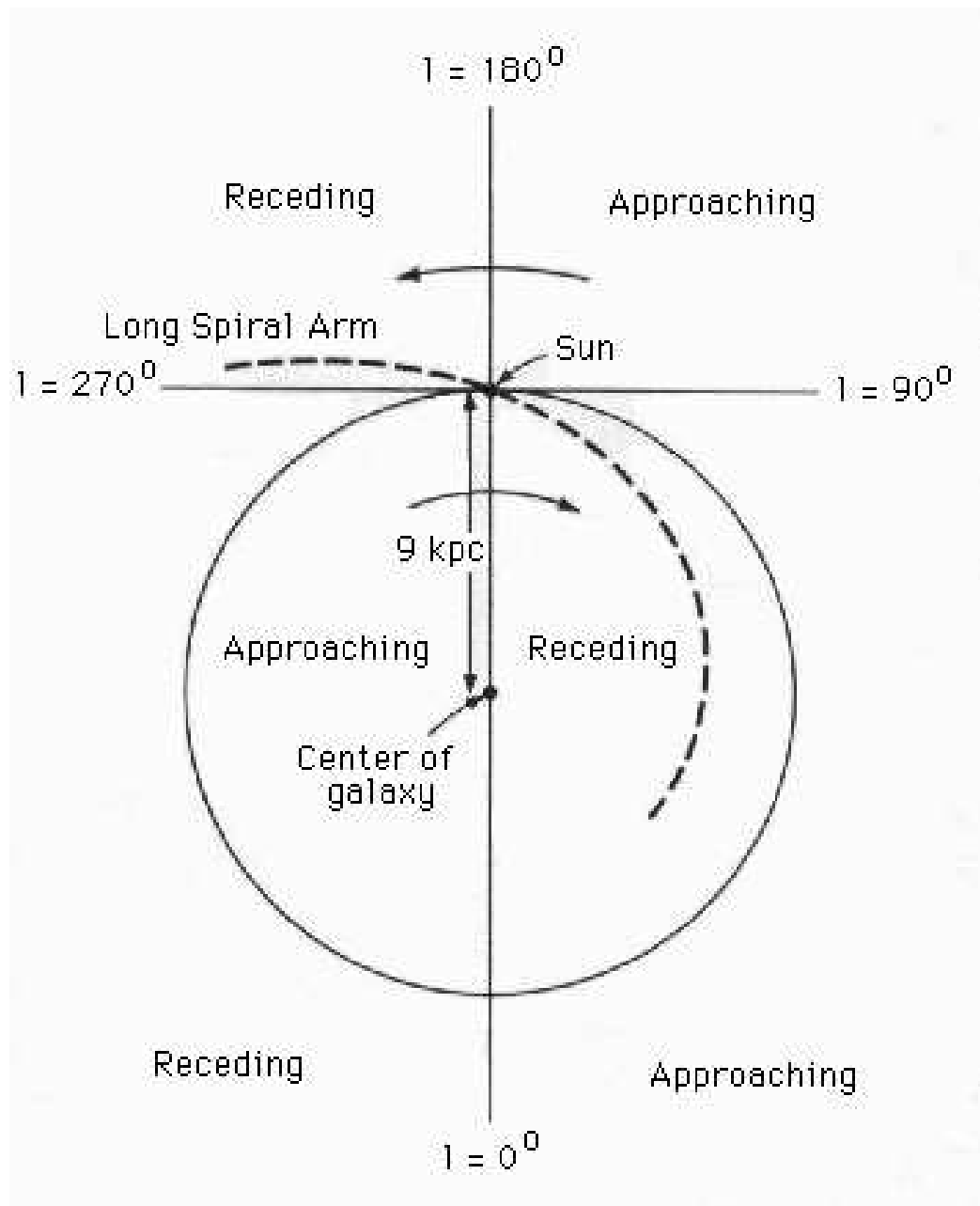


Figure 2.2: Simplified plan-view sketch of our galaxy showing regions of relative approach and recession with respect to the Sun [Kraus, 1986].

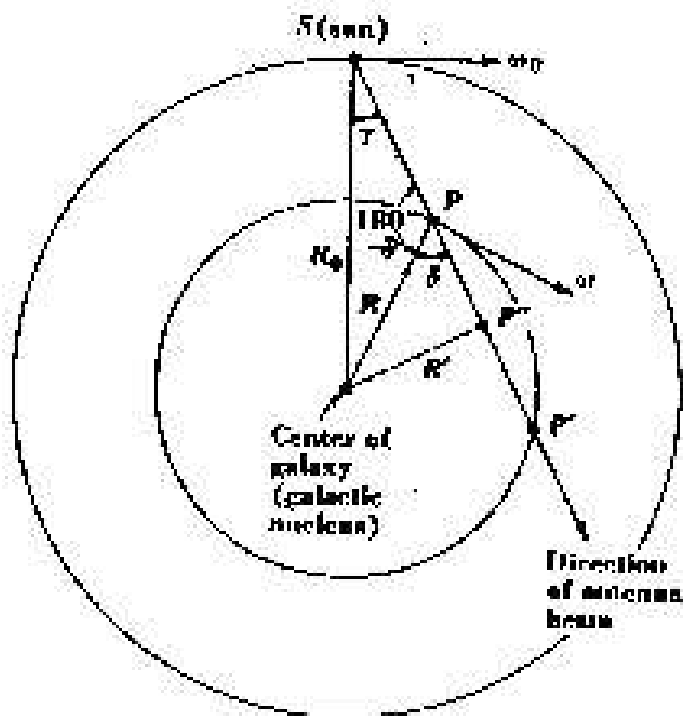


Figure 2.3: Geometric entities relevant in the computation. [Kraus, 1986]

$$R \sin \lambda = A = R_0 \sin(l) \quad (2.3)$$

and therefore:

$$\Delta v(R, l) = R_0 \sin(l) [\Omega(R) - \Omega(R_0)] \quad (2.4)$$

Therefore if we know how the Galaxy rotational velocity depends on the distance from the center (that is, if we know the galactic rotational velocity curve,  $\Omega(R)$ , see sec. 2.7) we can, for a given direction, associate at every radial velocity a distance along the line of sight.

## 2.5 Line broadening and anomalous velocities

The intrinsic broadening of the line emitted by a cloud, due to thermal motion and internal turbulence, gives a limit of this deprojecting technique. In fact, a cloud of temperature  $T$  generate a line emission with a width which corresponds to a  $\Delta v$  :

$$\Delta v = \sqrt{\frac{2kT}{m_H}} \quad (2.5)$$

where  $k$  is the Boltzmann constant and  $m_H$  is the proton mass. For example, for a HI cloud of temperature 100 K at galactic longitude  $30^\circ$ , this corresponds to a  $\Delta v$  of about 1 km/s, which in turn means a distance uncertainty of 100 pc along the line of sight. Therefore the resolution of matter radial distribution can not be smaller than this value. Internal turbulence of clouds also contributes to broaden the line profile, with  $\Delta v$  spanning a wide range of values.

For molecular clouds  $\Delta v$  can reach values of 10-20 km/s.

Line broadening is also responsible for the emission observed at velocities outside the dynamical range predicted by the rotational curve. In the deprojection process it is then necessary to take into account the line broadening to include also the matter with anomalous velocities.

## 2.6 The dynamical ambiguity

Each line of sight along which an observation is made crosses a circle of gas at a given distance from the center of galaxy in two points. Thus an ambiguity arises, because the Doppler velocities with respect to the Sun corresponding to these two points are the same. To resolve this ambiguity is needed to resort to a probabilistic approach. If the line of sight has a galactic latitude different from 0, then the two points with the same velocity lie at different heights on the galactic plane ( $z$ ). The matter density in the disk decreases exponentially with  $z$ , with different scale height for the different components. Then for a given line of sight, we can estimate that the probability of finding matter at distance  $r$  is proportional to

$$\zeta = e^{-\frac{1}{2} \frac{r^2 \cos^2 b}{z_h^2}} \quad (2.6)$$

where  $z_h$  is the scale height. The values we have used in our model are  $z_h = 100$  pc and  $z_h = 60$  pc respectively for HI region and for molecular clouds, according to recent estimates of the disk thickness of the two components. The density derived from the radio signal, at a velocity range that gives ambiguity, will be split between the two ambiguity points according to the weighting

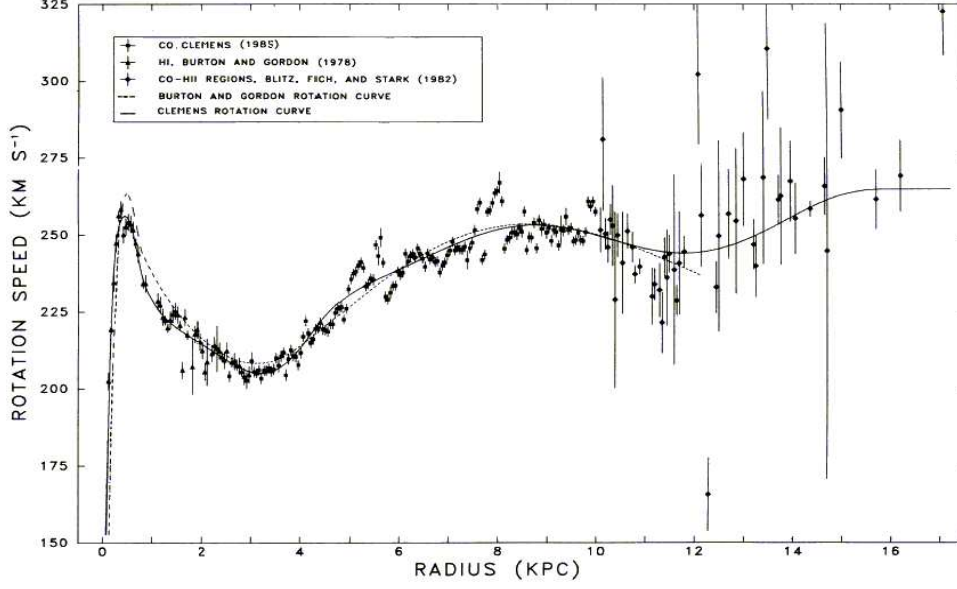


Figure 2.4: Plots of the rotation speed versus galactocentric radius. The solid line correspond to the polynomial fit [Clemens, 1985].

functions:

$$w_{near} = \frac{\zeta_{near}}{\zeta_{near} + \zeta_{far}} \quad (2.7)$$

$$w_{far} = \frac{\zeta_{far}}{\zeta_{near} + \zeta_{far}} \quad (2.8)$$

where  $\zeta_{near}$  and  $\zeta_{far}$  are the functions 2.6 calculated for the near and the far distance giving the same Doppler shift.

## 2.7 Rotation curve

In order to use the deprojection technique described above it is essential to exactly know the function  $\Omega(r)$ . The rotation curve we assume in the model is the one parameterized by [Clemens, 1985], and scaled for a galactic center

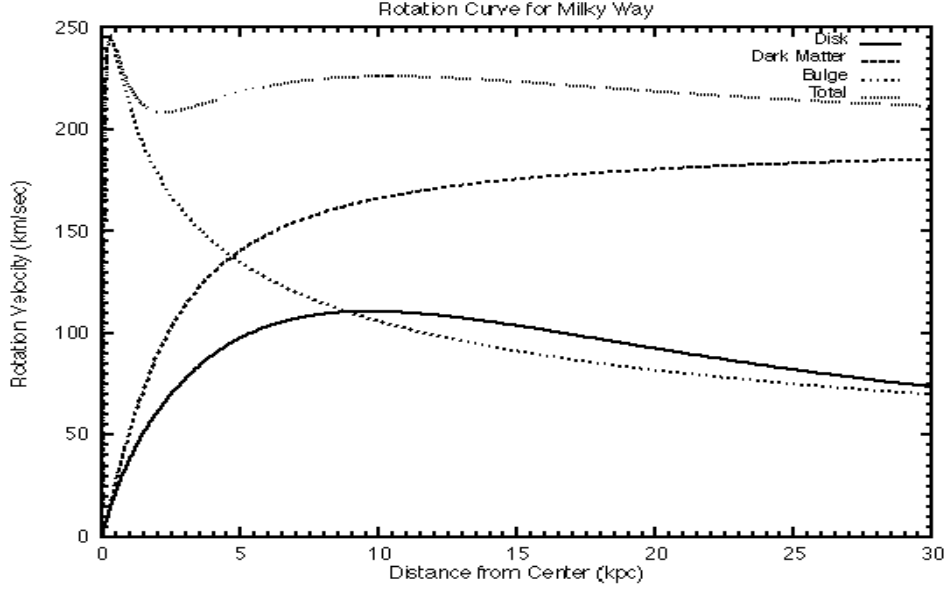


Figure 2.5: The observed rotation curve can be decomposed into the individual parts contributed by each component of the Galaxy: the disk (represented by the lowest solid line), the bulge plus the stellar halo (dotted line), and dark matter (dashed line).

distance of 8.5 kpc.

This curve was determined for the northern disk component of the Galaxy combining the Massachusetts-Stony Brook Galactic plane CO survey with data for HI in the nuclear region, outer CO - HII regions and globular clusters. The curve, obtained by fitting the data with a polynomial, is shown in figure 2.4.

## 2.8 Diffuse matter distribution

For the HI Hydrogen distribution we used the Leiden-Dwingeloo 21 cm survey ([Hartmann & Burton, 1997]). This survey covers the sky above declination  $-30^\circ$ . The Leiden-Dwingeloo survey improves the previous results especially in terms of sensitivity (an order of magnitude better), velocity range and

resolution. For the region around the south celestial pole, which is not covered by this survey, we used other observations, such as those from the Maryland-Parkes survey ([Kerr et al., 1986]).

The neutral Hydrogen density along the line of sight can be obtained by:

$$n_{HI} = -\frac{1.83 \cdot 10^{18}}{\Delta r} \int_{\Delta \nu} T_S \tau(\nu) d\nu \quad (2.9)$$

where  $T_S$  is the spin temperature and  $\tau(\nu)$  is the optical thickness:

$$\tau(\nu) = \ln\left(1 - \frac{T_b(\nu)}{T_S}\right) \quad (2.10)$$

where  $T_b$  is the observed brightness temperature.

The molecule of Hydrogen does not emit vibrational or rotational excitation mode. Therefore, in order to map the molecular Hydrogen distribution, it is used to observe the radiation emitted by CO as many observations have shown a strong correlation between CO emission,  $I(CO)$ , and  $H_2$  density,  $n(H_2)$ . The CO is assumed to be a tracer of molecular hydrogen with a ratio between hydrogen density and CO radio emissivity given by the factor X:

$$X = \frac{I(CO)}{n(H_2)} \quad (2.11)$$

The deprojected column density of molecular Hydrogen is related to the CO brightness temperature by the relation:

$$n_{H_2} = \frac{2X}{\Delta r} \int_{\Delta \nu} T_b(\nu) d\nu \quad (2.12)$$

In order to obtain the distribution of molecular hydrogen we use the CO observations described in [Dame et al., 2001]. These observations came from 31 surveys which cover different portions of the galactic plane.

## 2.9 Interstellar Radiation Field

Cosmic rays produce gamma rays through the inverse Compton interaction with photons of the cosmological background and of the interstellar radiation field (ISRF). In order to account for this component we use the analytical model proposed by Cox [Cox et al., 1986], and parametrized by Chi & Wolfendale [Chi & Wolfendale, 1991]. It describes the ISRF as the result of three main contributions: far infrared (due to dust emission), near infrared and optical/UV (due to stars emission). A more detailed model of ISRF has been more recently developed by [Strong et al., 2000], in which the spectrum of each components is derived (see figure 1.6). However we have considered that, for our purposes, the simpler Cox model is sufficient. We let as future improvement of the gamma-ray emissivity model a study of the differences that would imply the use of a more refined ISRF model.

## 2.10 Cosmic Rays

One of the aims of gamma ray diffuse emission studies is to discriminate between cosmic ray models. For this reason our gamma ray emissivity model can use as input both different analytical and numerical cosmic ray models which have been developed in the last years. The cosmic rays model assumed for the computation of the gamma emissivity, determines, in practice, the resulting

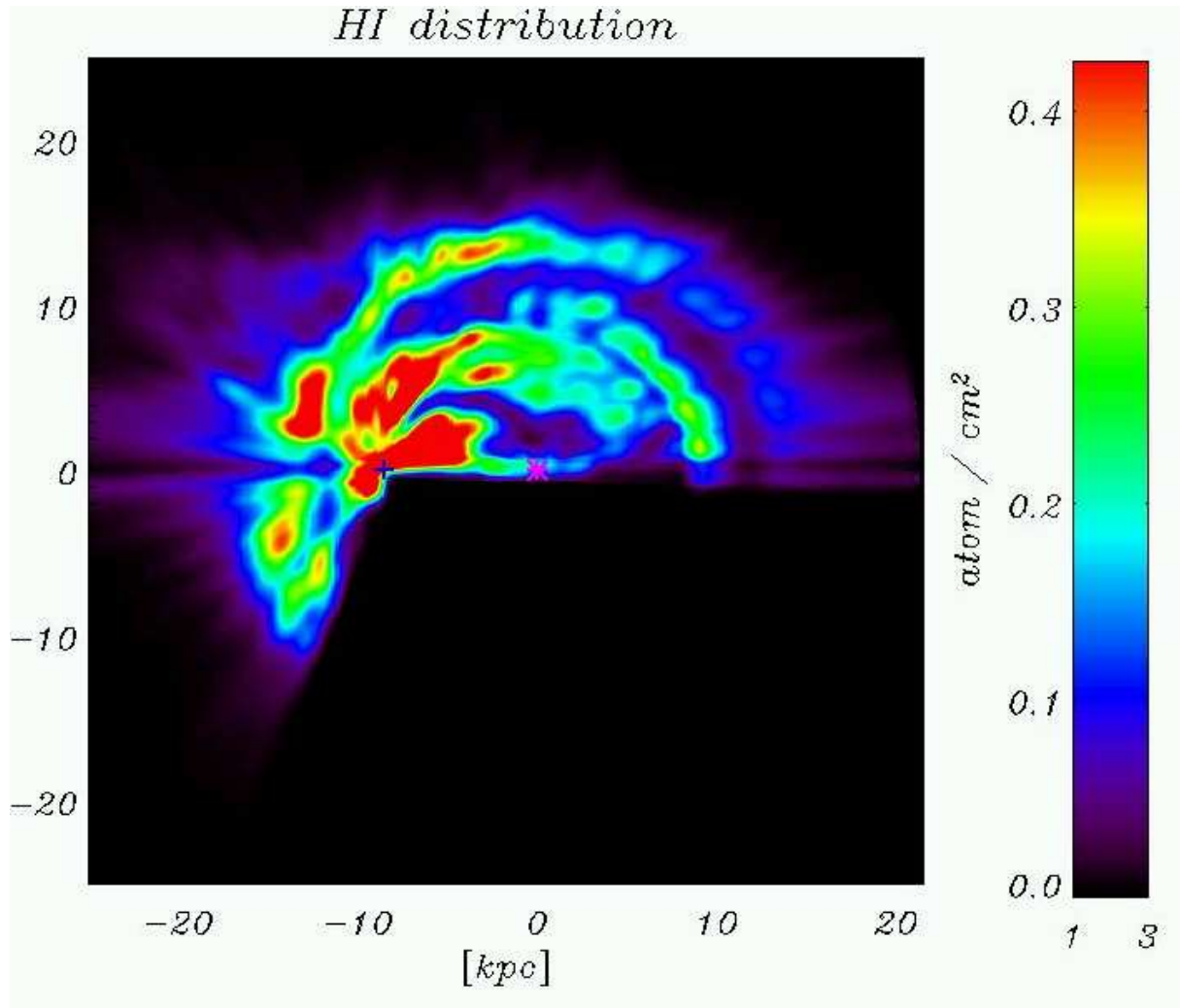


Figure 2.6: Atomic Hydrogen density on the Galactic Plane [Giuliani et al., 2003a], derived from the Leiden-Dwingeloo survey. The south celestial pole is not covered by this survey.

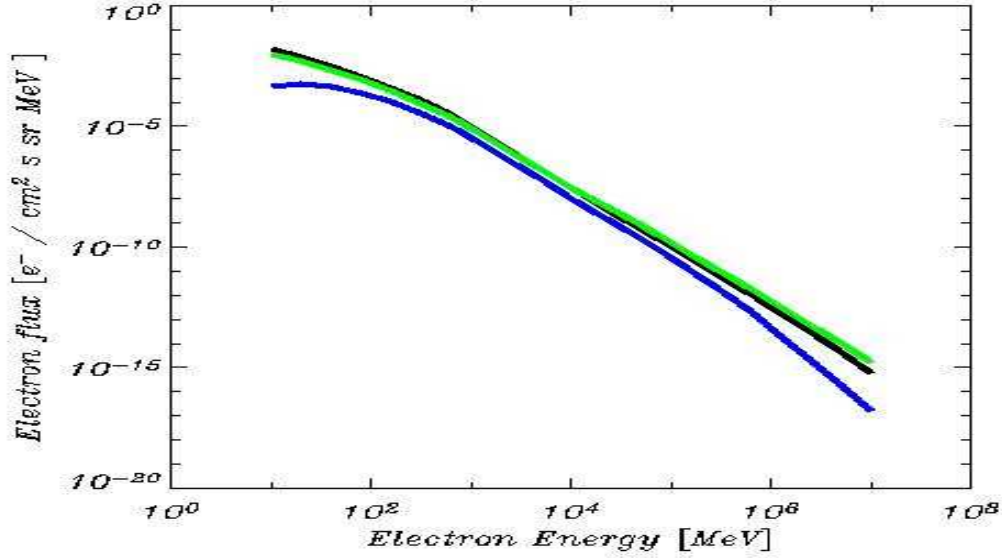


Figure 2.7: The energy distribution of the assumed electrons model. The black line is the distribution predicted for the Galaxy center ( $r=0$ ,  $z=0$ ), the green line is for the Galaxy outer region ( $r=30$  kpc,  $z=0$ ), while the blue line is for a region out of the plane ( $r=8.5$  kpc  $z=3$  kpc)

gamma-ray spectrum.

The results presented in the following chapter are obtained by using the cosmic ray model given by the numerical code GALPROP [Strong et al., 2000], [Strong et al., 2004a] which derives the cosmic ray distribution accounting for physical processes like diffusion and energy losses. We used the set of GALPROP input parameters, called “HE” in [Strong et al., 2000], namely, electron injection index: 1.7, proton injection index: 2.25, height of the cosmic-rays halo: 4 kpc, and diffusion coefficient of  $6 \cdot 10^{28} \text{ cm}^2 \text{ s}^{-1}$ . The distribution of cosmic-rays sources chosen follows the supernovae remnants distribution. This cosmic-rays model is able to reproduce the GeV excess, using a spectrum of cosmic electron harder than the local one.



# Chapter 3

## Observing the Diffuse Emission

### 3.1 The gamma-ray sky

The intensity of the diffuse gamma-ray flux ( $E > 100$  MeV) from different sky direction,  $M(l, b)$ , foreseen by this model can be evaluated by:

$$M(l, b) = \frac{1}{4\pi} \int_{100 \text{ MeV}}^{\infty} \int_0^{\infty} g(l, b, r, E) dr dE \quad (3.1)$$

Figure 3.1 and 3.5 show the total AGILE model for the first and second Galactic quadrant. The contributions to the total emission produced by the different cosmic-rays targets, for the first Galactic quadrant, are shown in figure 3.2, 3.3 and 3.4 and are obtained respectively by substituting  $g$  in eq.3.1 with :

$$g_{HI} = (q_{pp} + q_{br})n_{HI}$$

$$g_{H2} = (q_{pp} + q_{br})n_{H2}$$

$$g_{iC} = q_{iC}n_{ph}$$

Figures 3.6, 3.7 and 3.8 (second quadrant) are obtained in an analogous way.

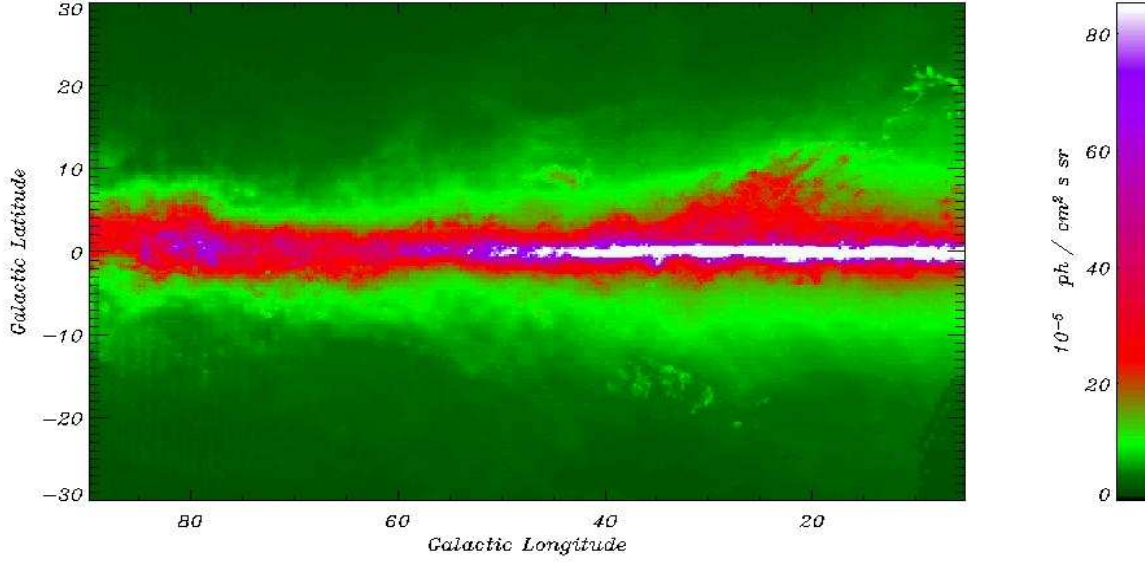


Figure 3.1: The AGILE emission model for the first Galactic quadrant.

### 3.2 New vs old model

Figure 3.9 shows the comparison between the EGRET and AGILE diffuse emission models for the Polaris Flare regions, while the same comparison for the sky region dominated by the molecular cloud of Orion is given in figure 3.10.

Obviously the finer grid with which the AGILE model is built (bin area is  $0.25 \times 0.25$  degrees) gives a better resolution to the gamma sky map. Figures 3.11 - 3.14 show the galactic latitude and longitude gradients for the two models. They indicate a good agreement between the two models on the galactic plane and a discrepancy outside the plane that can be understood in terms of the

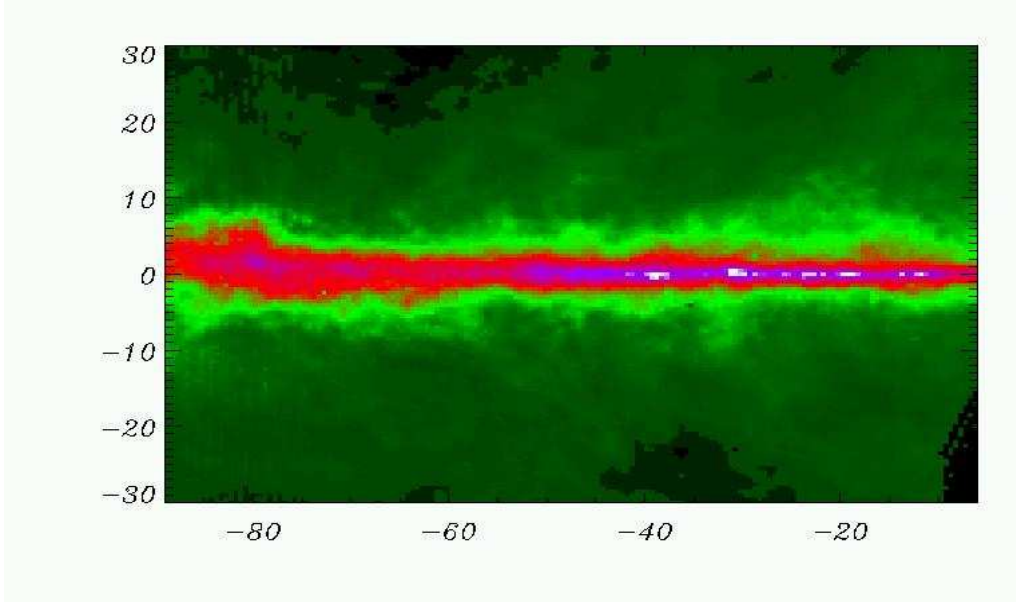


Figure 3.2: Contribution of HI regions to AGILE model, for the first Galactic quadrant. The colorscale is the same shown by the colorbar of figure 3.1.

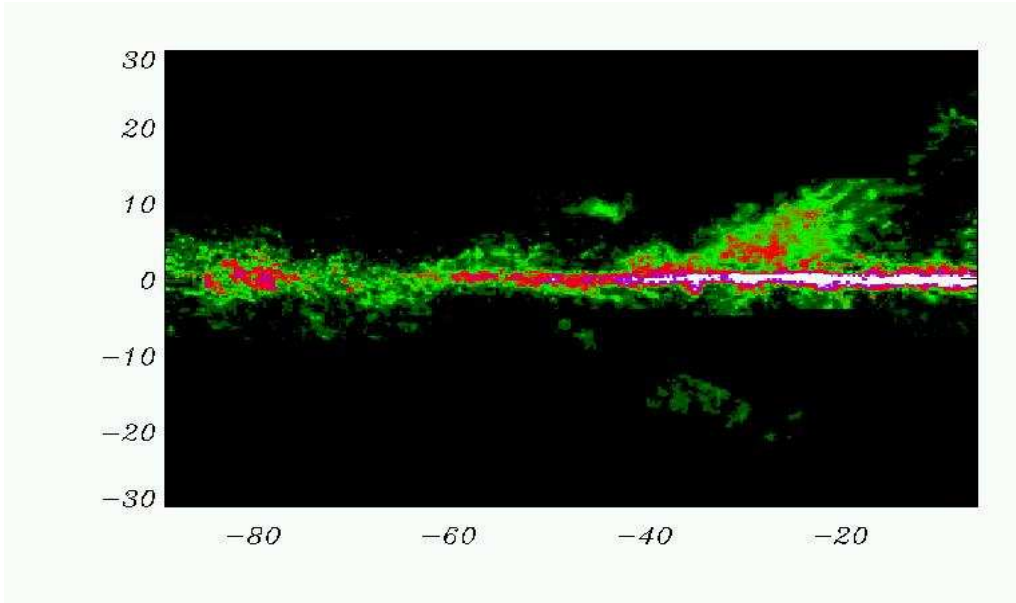


Figure 3.3: Contribution of molecular clouds to AGILE model, for the first Galactic quadrant. The colorscale is the same shown by the colorbar of figure 3.1.

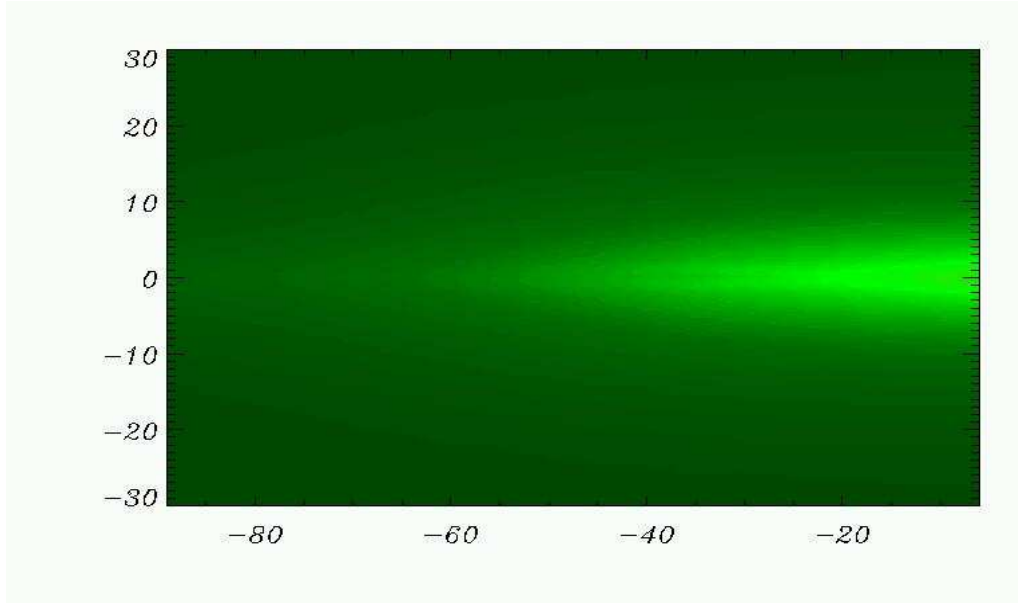


Figure 3.4: Contribution of the interstellar radiation field to AGILE model, for the first Galactic quadrant. The colorscale is the same shown by the colorbar of figure 3.1.

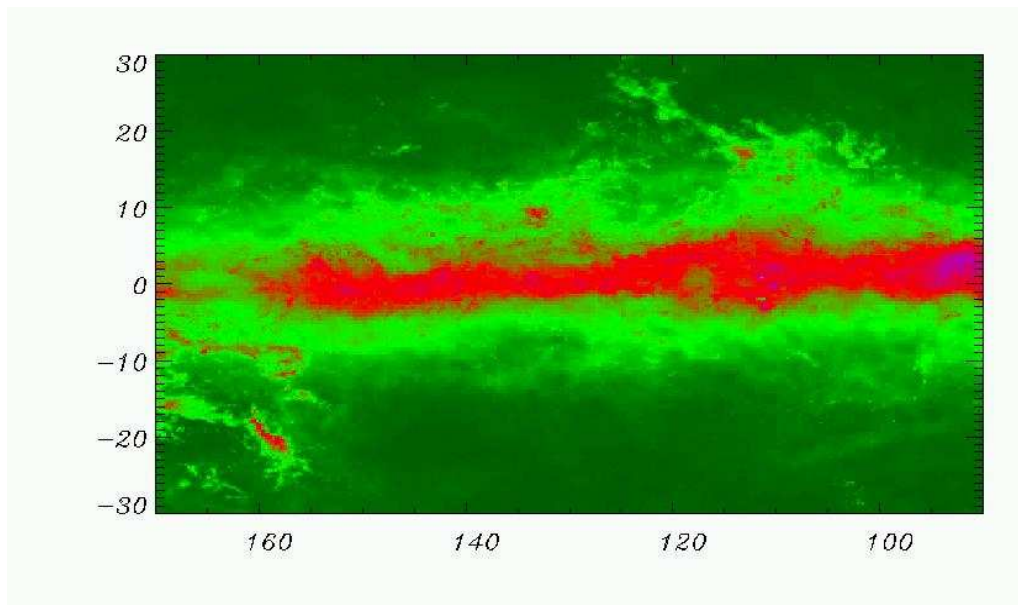


Figure 3.5: The AGILE emission model for the second Galactic quadrant. The colorscale is the same shown by the colorbar of figure 3.1.

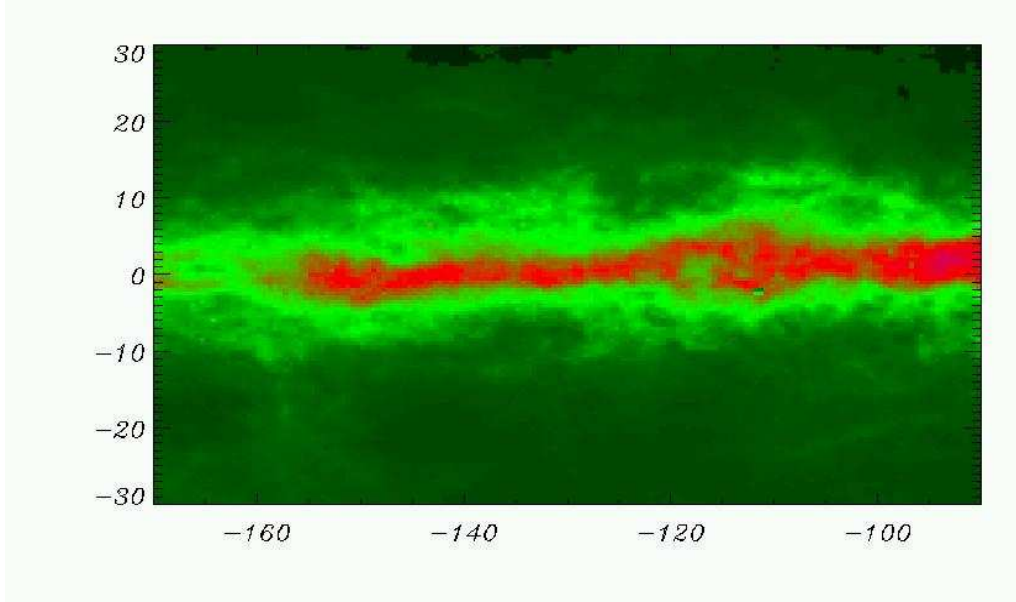


Figure 3.6: Contribution of HI regions to AGILE model, for the second Galactic quadrant. The colorscale is the same shown by the colorbar of figure 3.1.

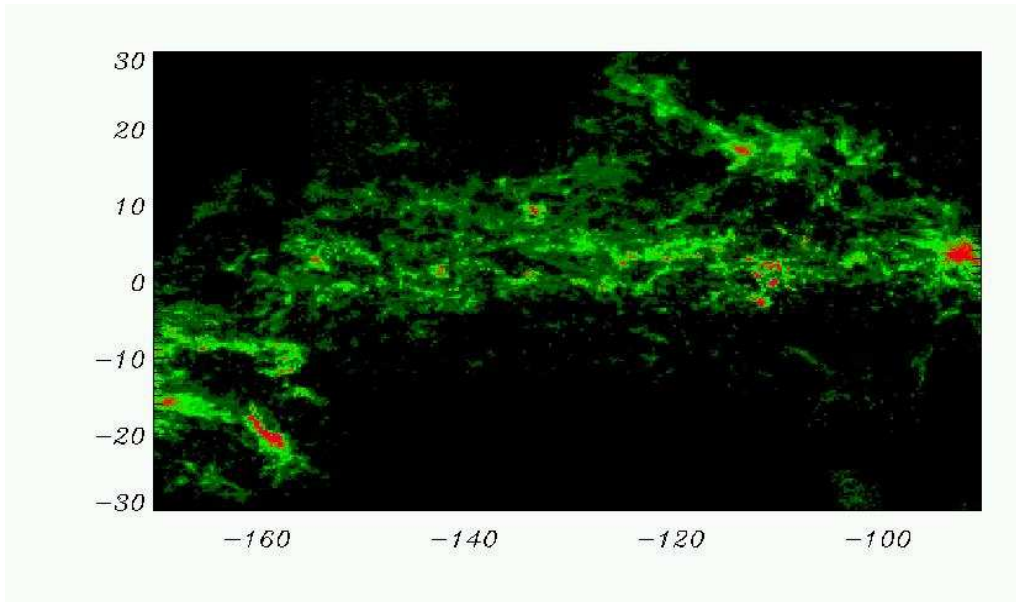


Figure 3.7: Contribution of molecular clouds to AGILE model, for the second Galactic quadrant. The colorscale is the same shown by the colorbar of figure 3.1.

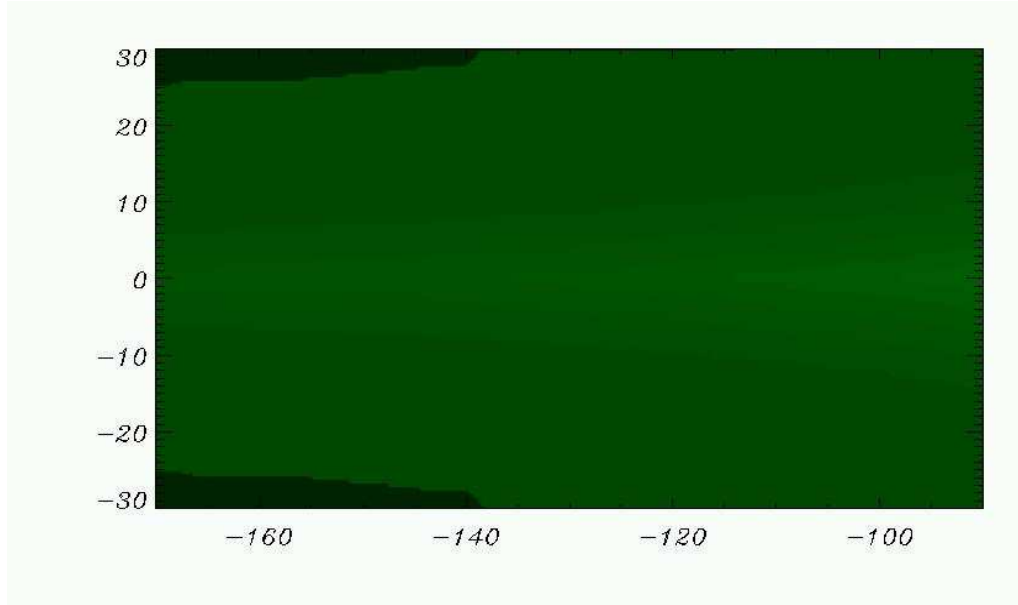


Figure 3.8: Contribution of the interstellar radiation field to AGILE model, for the second Galactic quadrant. The colorscale is the same shown by the colorbar of figure 3.1.

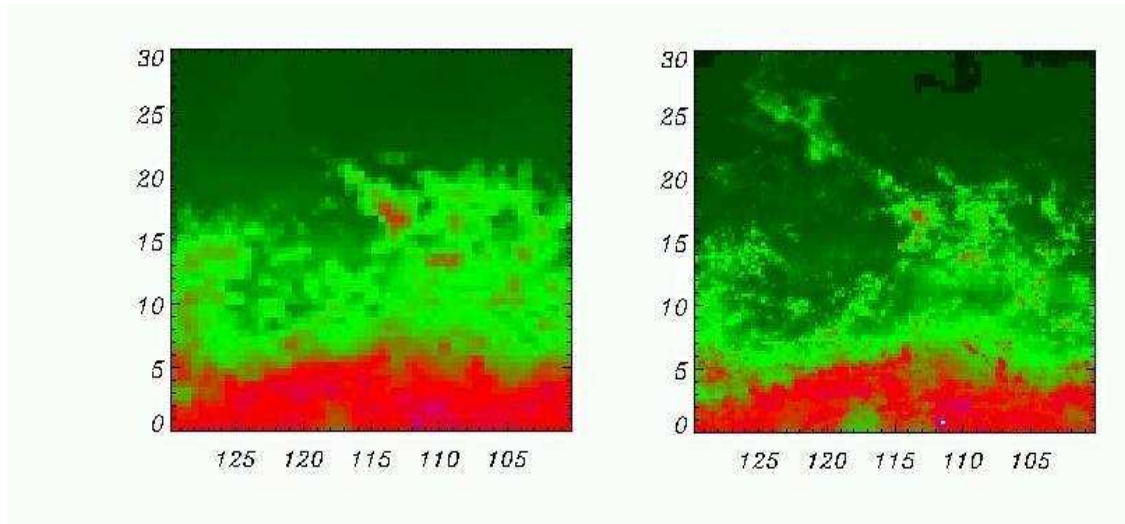


Figure 3.9: Comparison between the EGRET (left) and AGILE (right) diffuse emission model for the Polaris Flare regions. The colorscale is the same shown by the colorbar of figure 3.1.

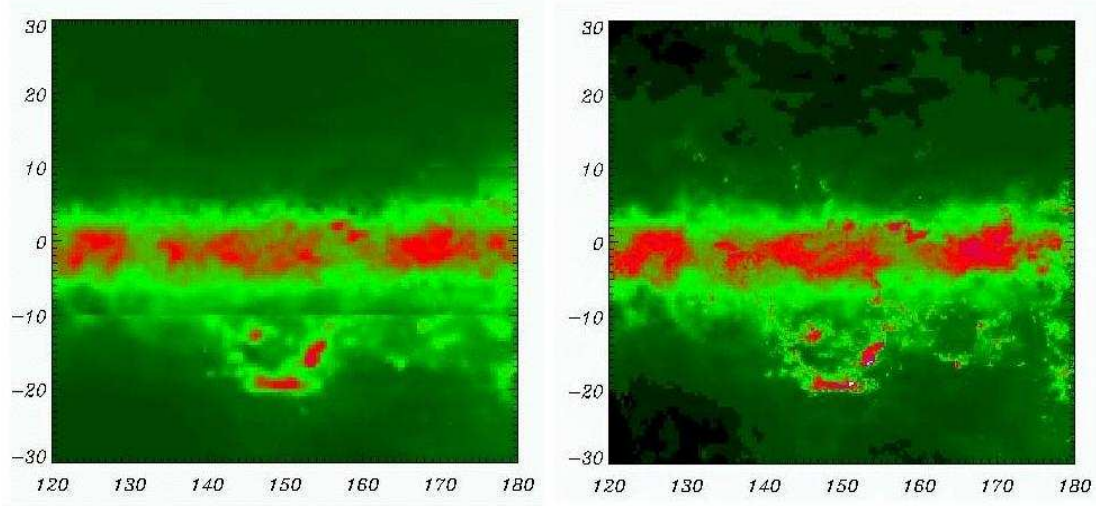


Figure 3.10: Comparison between the EGRET (left) and AGILE (right) diffuse emission model for the Orion molecular clouds regions. The colorscale is the same shown by the colorbar of figure 3.1.

different height dependence of the cosmic-ray electronic component.

### 3.3 Model vs Observations

The gamma ray data presented in this section are a sum of the EGRET observations cycles from 1 to 9, which covers almost the whole observing life of the instrument. The EGRET data for the outer Galaxy are represented in figures 3.15 and 3.16. Figure 3.15 shows the intensity of gamma ray sky observed by EGRET as function of galactic latitude, averaged in longitude from 90 to 160 degrees (second galactic quadrant). The thickness of the line represents the statistical uncertainty ( $1\sigma$ ). The red and the blue lines correspond to the AGILE and EGRET model respectively, convolved with the EGRET Point Spread Function. The contribution of molecular and neutral hydrogen to gamma emission are represented by the green and yellow lines. A constant

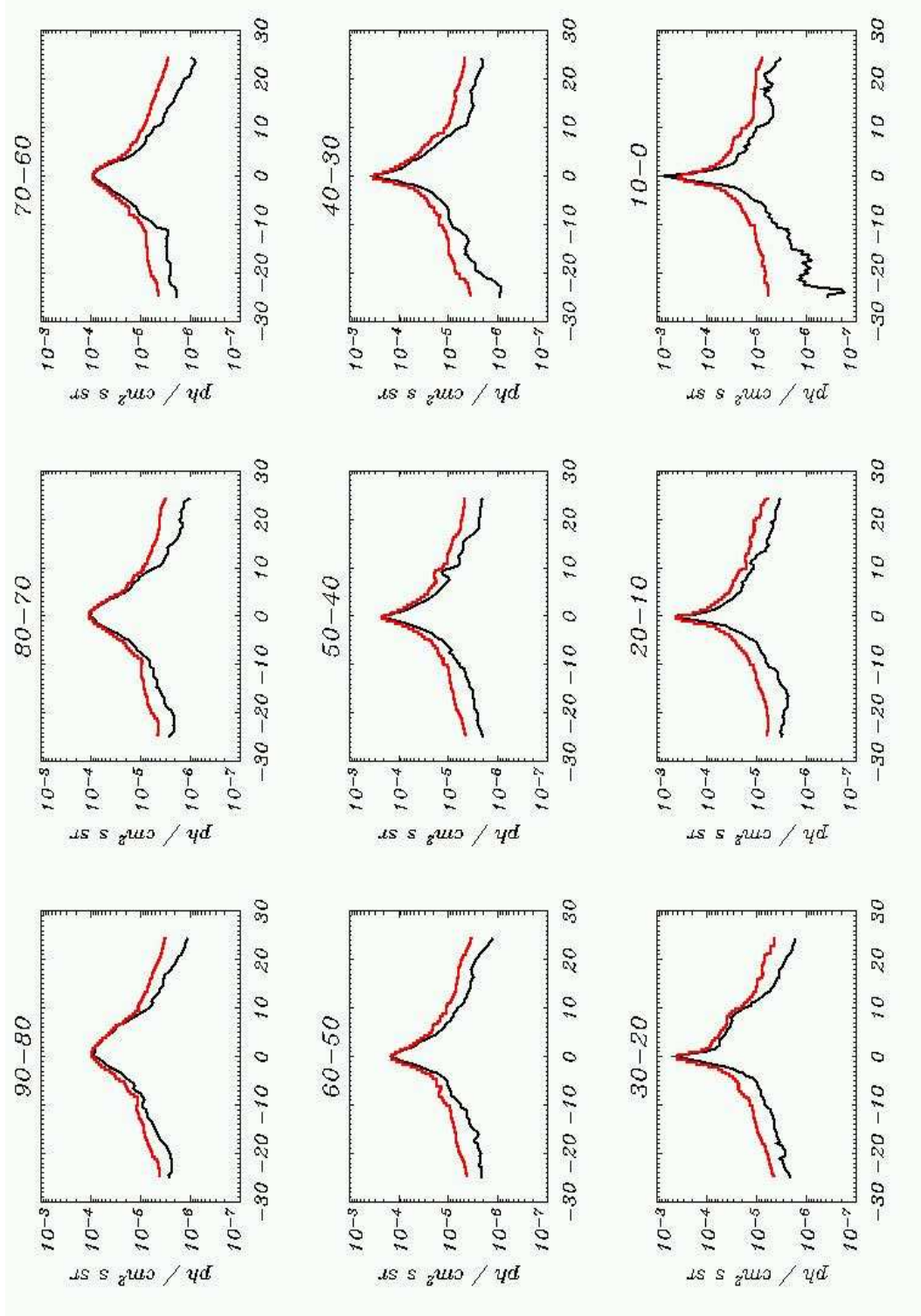


Figure 3.11: Galactic latitude profiles for the EGRET (black) and AGILE (red) model for energy channel 100 MeV - 150 MeV and different ranges of longitude.

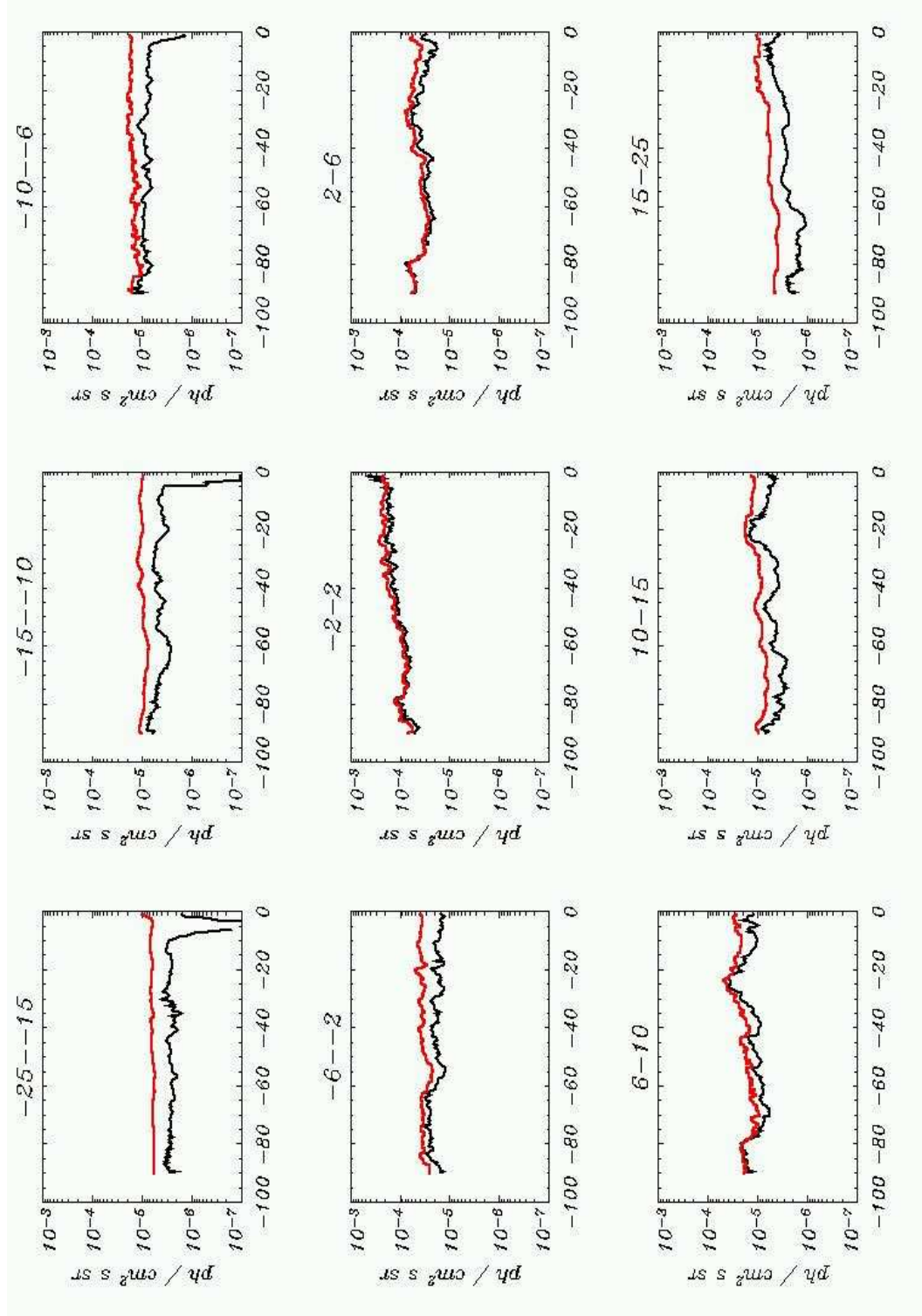


Figure 3.12: Galactic longitude profiles for the EGRET(black) and AGILE (red) model for energy channel 100 MeV - 150 MeV and different ranges of latitude.

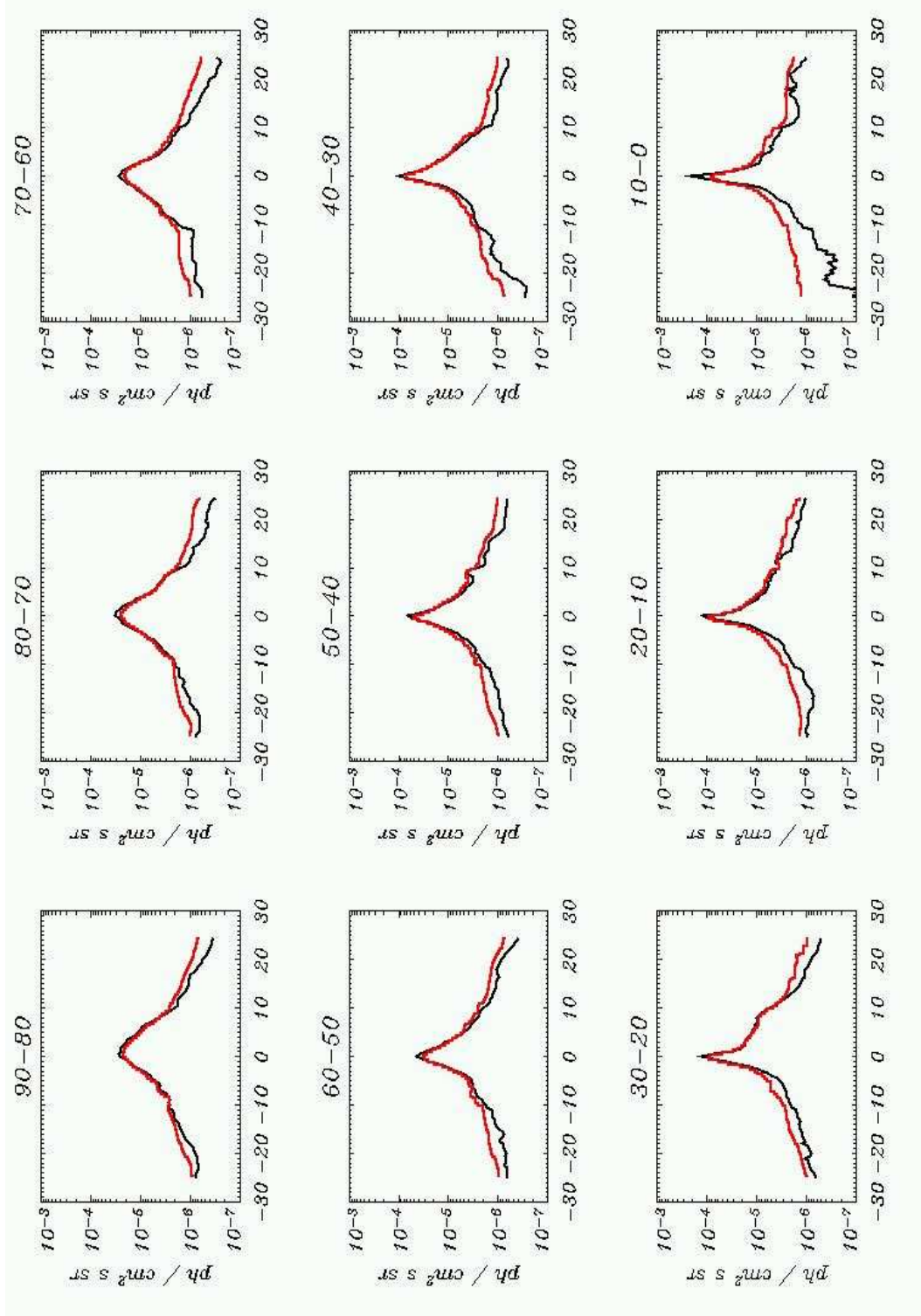
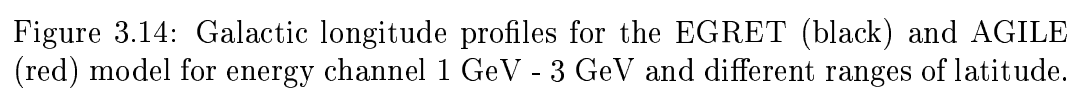


Figure 3.13: Galactic latitude profiles for the EGRET(black) and AGILE (red) model for energy channel 1 GeV - 3 GeV and different ranges of longitude.



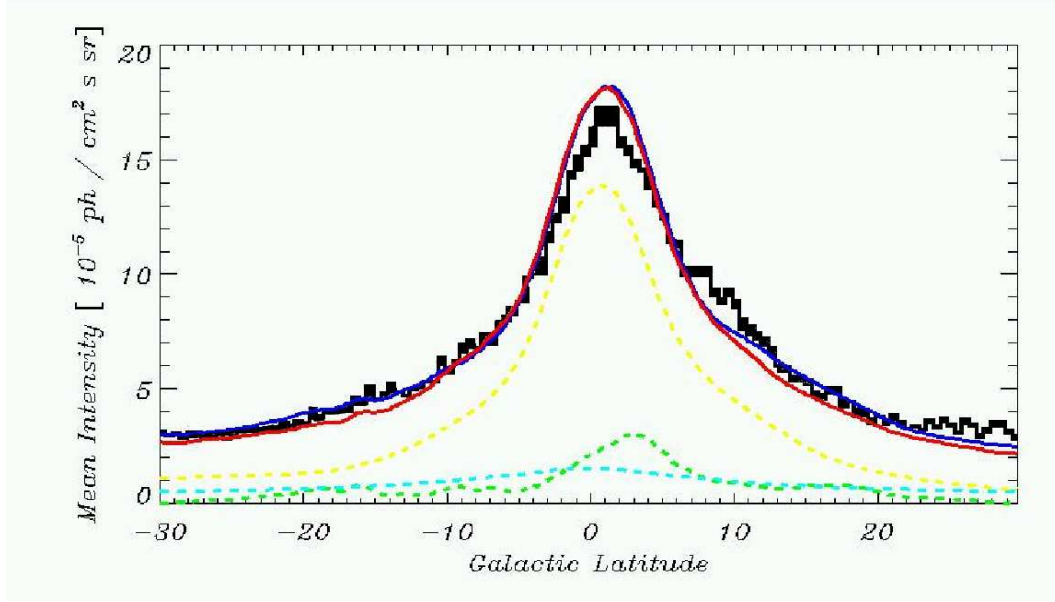


Figure 3.15: Diffuse emission intensity observed by EGRET ( $E > 100$  MeV) as function of galactic latitude averaged in longitude from 90 to 160 degrees. The red and the blue lines represent the AGILE and EGRET model respectively. The figure shows also the contributes due to HI region (yellow), molecular clouds (green) and inverse Compton (sky-blue).

value of  $10^{-5} \text{ ph cm}^2 \text{ s sr}$  has been added to both the AGILE and EGRET model in order to take into account the extragalactic diffuse emission. Figure 3.16 is the analogous plot but averaged over latitude.

The figures 3.17 and 3.18 show, instead, the results for the inner Galaxy. In this case, besides the contribution of neutral and molecular Hydrogen, the contribution of inverse Compton on interstellar radiation field is visible. From these plots a good agreement among the two models and EGRET observations can be found.

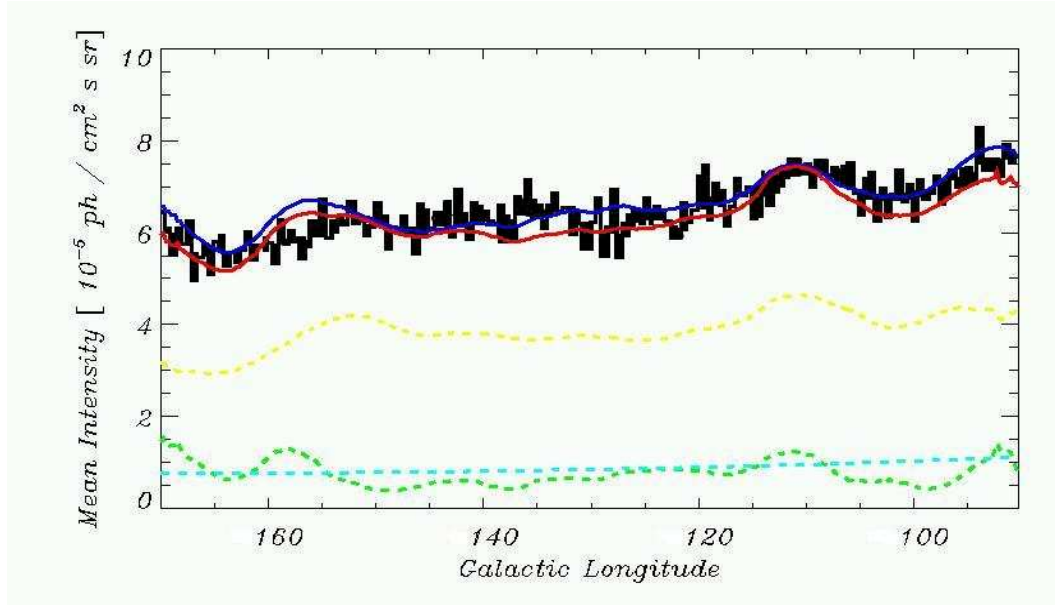


Figure 3.16: As figure 3.15 but averaged over latitudes -30 to 30.

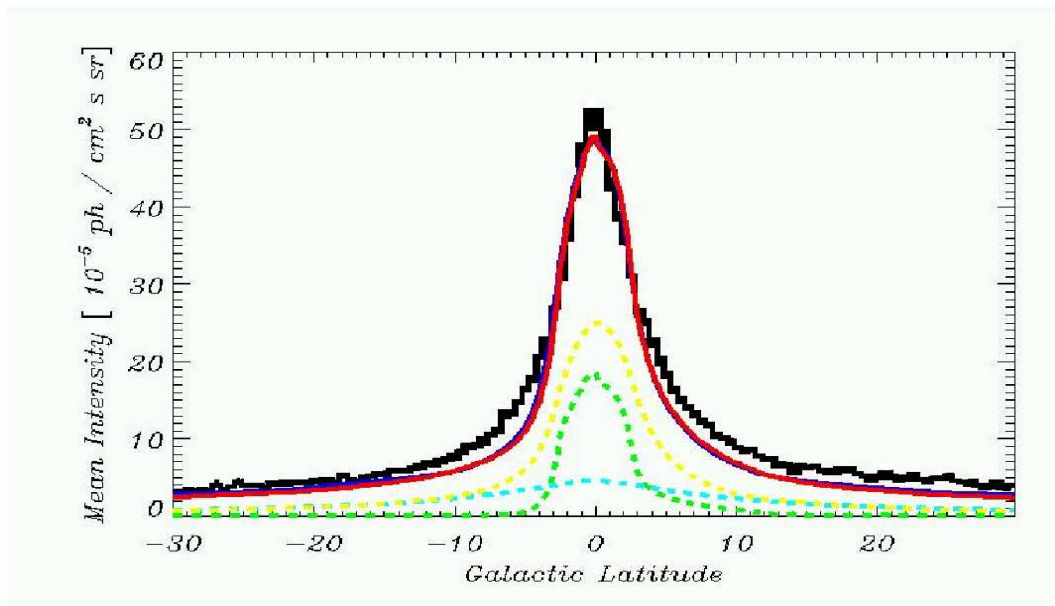


Figure 3.17: Diffuse emission intensity observed by EGRET ( $E > 100$  MeV) as function of galactic latitude averaged in longitude from 0 to 90 degrees. The red and the blue lines represent the AGILE and EGRET model respectively. The figure shows also the contributes due to HI region (yellow), molecular clouds (green) and inverse Compton (sky-blue).

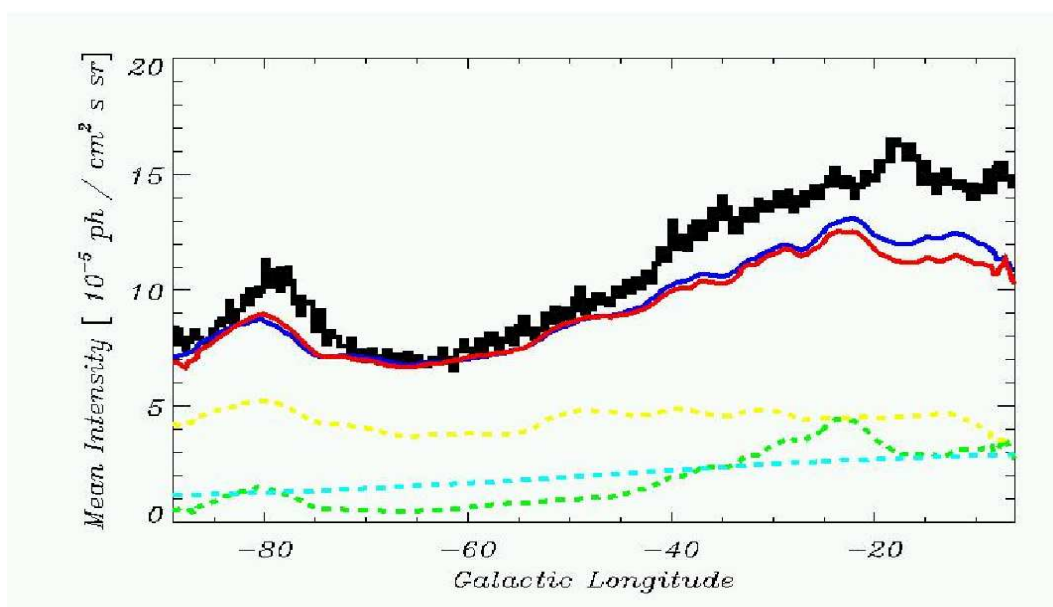


Figure 3.18: As figure 3.17 but averaged over latitude -30 to 30.

### 3.4 Cosmic-Ray Studies

The observed features of the galactic gamma-ray diffuse emission depend both of the interstellar medium distribution and on the cosmic ray distribution, it is hence not simple to get informations about the single components. In this paragraph it is presented a method to extract cosmic-ray information from gamma-ray observation, using only the matter distribution that we derived (section 2.4). We compare the results found with two CR models that follow two completely different approaches, the CR used for EGRET model, and the CR distribution derived from GALPROP, the same we use to derive the results presented in the previous sections. As it has been described in section 2.1, the model developed for the EGRET data analysis is based on the coupling among the components of the interstellar medium (diffuse matter, magnetic field and cosmic rays). In this way, it is possible to evaluate the cosmic rays density directly starting from the diffuse matter density, which can be obtained from radio observations. A completely different approach has been assumed by other models, which predict the cosmic rays density assuming a certain sources distribution and calculating how the cosmic rays propagate from these. Both the matter based model and the propagation computation model agree quite well with the gamma-ray observation but they predict very different CR distribution in Galaxy. Figure 3.19, shows the distribution on the galactic plane of the proton and electron density ( $\zeta_p$  and  $\zeta_e$ ) normalized respect to the value assumed as local density. in this case the two function are coincident for construction. Figures 3.20 and 3.21 show the same function for the distribution of cosmic rays derived from the GALPROP code. The functions  $\zeta$  are calculated integrating the cosmic-ray energy spectrum between 10

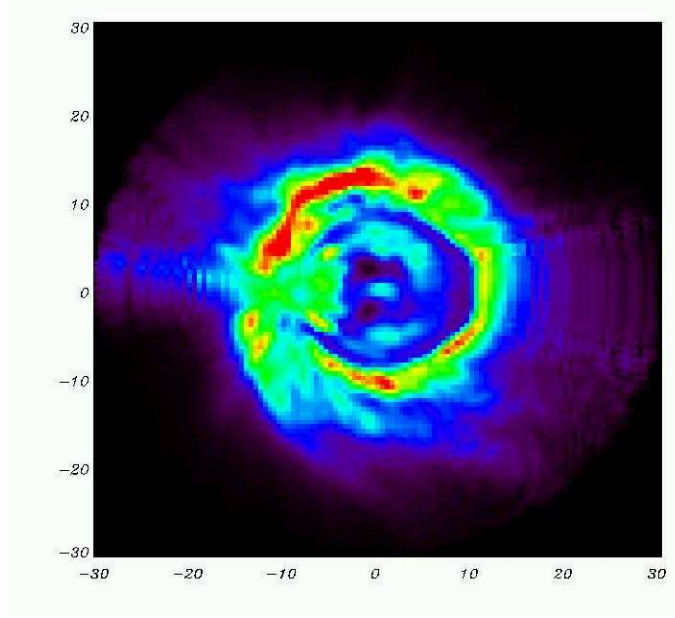


Figure 3.19: Distribution of  $\zeta$  assumed by the EGRET model.

MeV and 10 GeV.

It is useful to calculate the mean value of the  $\zeta$  functions on the line of sight averaged on the matter density, because this quantity can be directly derived from gamma-rays observations.

$$\bar{\zeta}_p(l, b) = \frac{\int_0^\infty \zeta_p(l, b, r) n_H(l, b, r) dr}{\int_0^\infty n_H(l, b, r) dr} \quad (3.2)$$

$$\bar{\zeta}_e(l, b) = \frac{\int_0^\infty \zeta_e(l, b, r) n_H(l, b, r) dr}{\int_0^\infty n_H(l, b, r) dr} \quad (3.3)$$

where  $n_H$  is the total Hydrogen density ( $n_h = n_{HI} + n_{H_2}$ ). The functions  $\bar{\zeta}$  for the two models are shown in figures 3.23 (EGRET) and 3.22 (GALPROP).

In order to extract such informations from gamma-rays observations we define two quantities  $k_{pp}(l, b)$  and  $k_{br}(l, b)$  that represent the average gamma-ray emis-

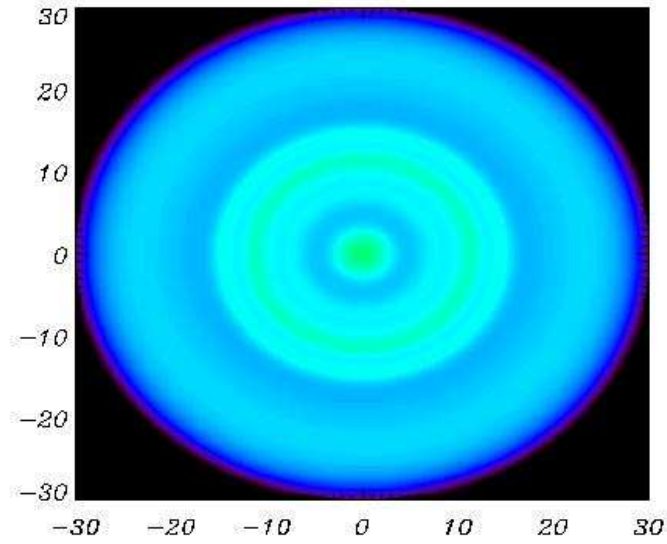


Figure 3.20: Distribution of  $\zeta_p$  calculated for the proton distribution produced by GALPROP (see section 2.10).

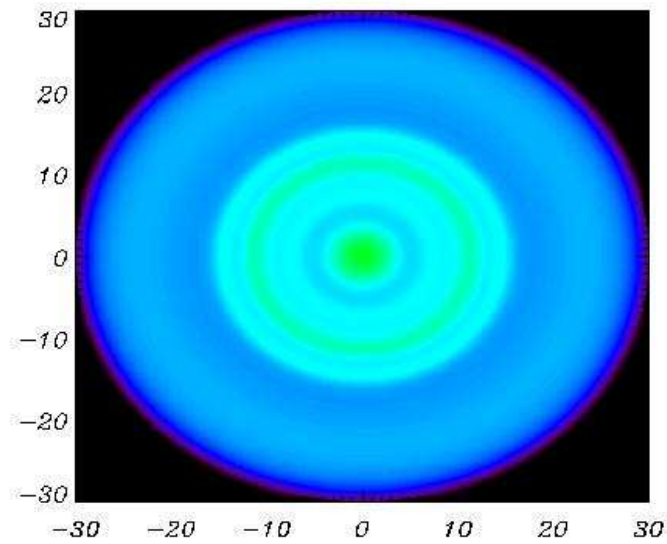


Figure 3.21: Distribution of  $\zeta_e$  calculated for the proton distribution produced by GALPROP (see section 2.10).

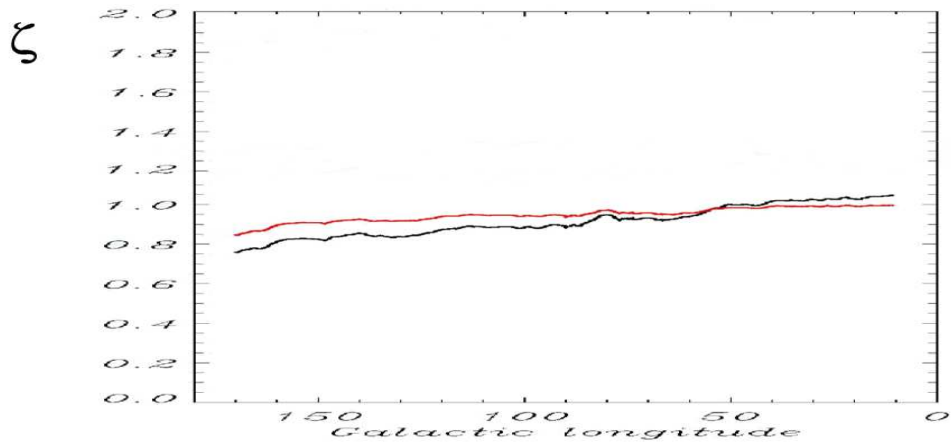


Figure 3.22:  $\bar{\zeta}_p$  (black) and  $\bar{\zeta}_e$  (red) calculated for the cosmic-ray model produced by GALPROP code.

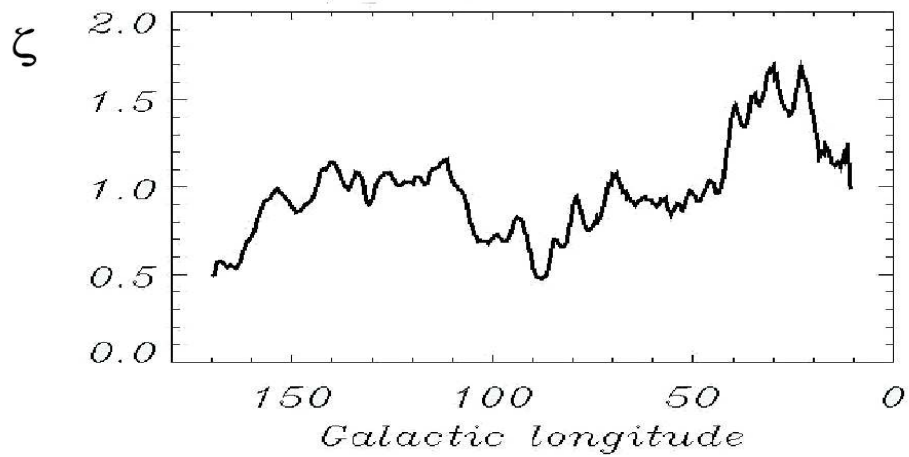


Figure 3.23:  $\bar{\zeta}_p$  and  $\bar{\zeta}_e$  calculated for the EGRET model.

sivity, for proton-proton scattering and bremsstrahlung, respectively, along a line of sight. For this purpose we require the two following assumptions to be satisfied: i) the matter distribution we obtain from radio survey is the exact three-dimensional distribution ii) the cosmic rays have the same spectral shape, even if with different normalization, in the galactic plane.

In order to eliminate the contribution due to interstellar radiation field the following analysis has been restricted to the Galactic plane region and to energies lower than 1 GeV. Under these assumptions the spectrum  $S(E, l, b)$  of the diffuse emission observed by EGRET from the Galactic plane consist of two main components, namely proton-proton and bremsstrahlung emissivities convolved with matter distribution. For the plane region,  $\sim |b| < 5^\circ$ , in fact, the extragalactic contribution can be neglected.

$$S(E, l, b) = S_{pp}(E, l, b) + S_{br}(E, l, b) \quad (3.4)$$

where

$$S_{pp}(E, l, b) = \frac{1}{4\pi} \int q_{pp}(E, l, b, r) n_H(l, b, r) dr \quad (3.5)$$

$$S_{br}(E, l, b) = \frac{1}{4\pi} \int q_{br}(E, l, b, r) n_H(l, b, r) dr \quad (3.6)$$

$S_{pp}$  has a spectral shape with a bump around 67 MeV and probably dominates above 200 MeV, while  $S_{br}$  is more important for low energies (see figure 3.24). To separate the contributions due to the matter distribution and that due to cosmic rays, we define a function  $\bar{q}_{pp}(E, l, b)$ :

$$\bar{q}_{pp}(E, l, b) = \frac{\int_0^\infty q_{pp}(E, l, b, r) n_H(l, b, r) dr}{\int_0^\infty n_H(l, b, r) dr} \quad (3.7)$$

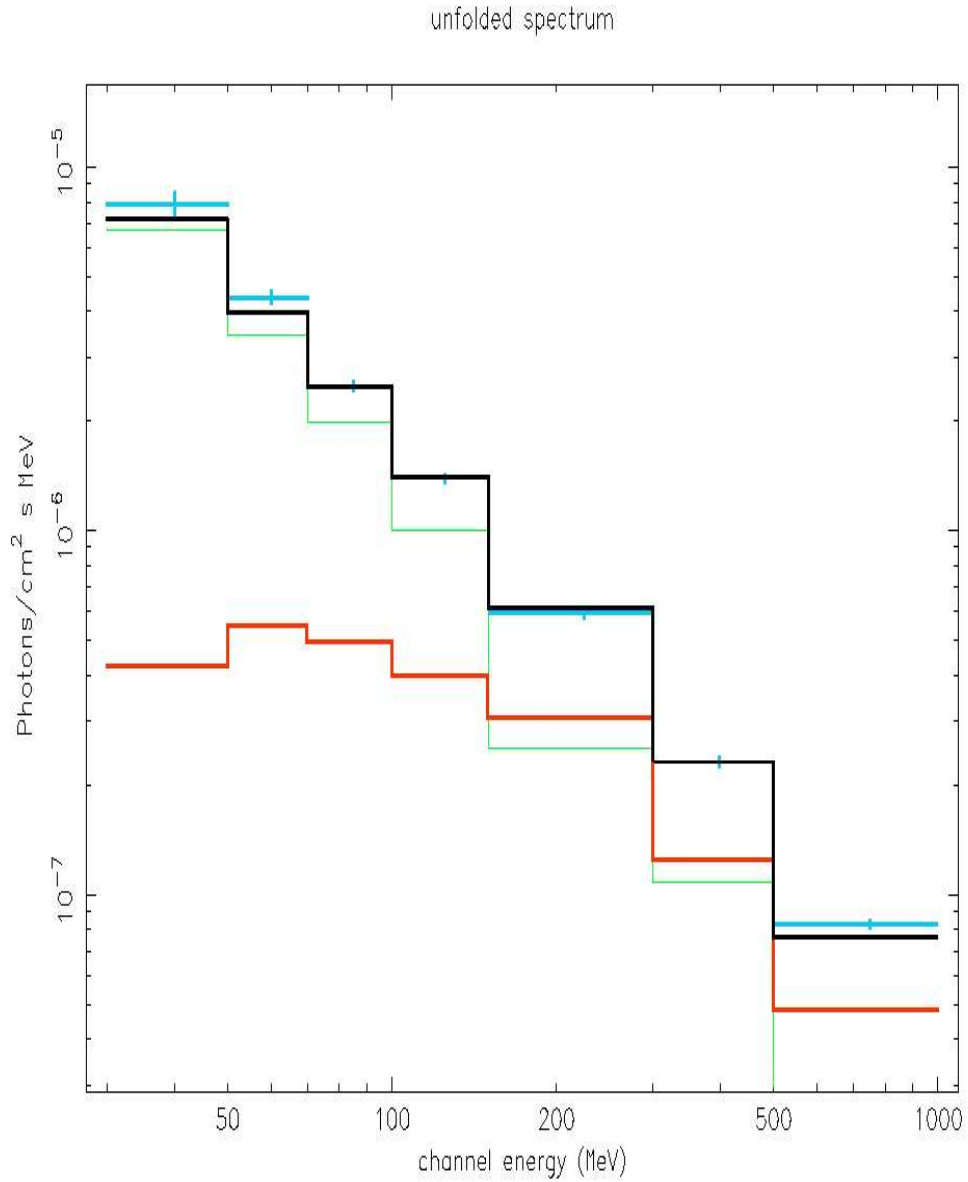


Figure 3.24: The spectrum of the diffuse emission in the galactic plane ( $l=30$   $b=0$ ) observed by EGRET (Light blue data). These data are fitted by a component derived from pp emissivity,  $S_{pp}^0$ , (red line) plus a component due to Bremsstrahlung emissivity,  $S_{br}^0$ , (green line). The total is shown by the black line

which is the average value of  $q_{pp}$ , weighted on the matter distribution along the line of sight.  $\bar{q}_{br}(E, l, b)$  can be obtained in an analogous way. Therefore eqs. 3.5 become:

$$S_{pp}(E, l, b) = \frac{1}{4\pi} \bar{q}_{pp}(E, l, b) \int n_H(l, b, r) dr \quad (3.8)$$

$$S_{br}(E, l, b) = \frac{1}{4\pi} \bar{q}_{br}(E, l, b) \int n_H(l, b, r) dr \quad (3.9)$$

In order to fit the observed spectrum we have built two "reference components" obtained by multiplying the local emissivity for the hydrogen column:

$$S_{pp}^0(E, l, b) = \frac{1}{4\pi} q_{pp}^{model}(E) \int n_H(l, b, r) dr \quad (3.10)$$

$$S_{br}^0(E, l, b) = \frac{1}{4\pi} q_{br}^{model}(E) \int n_H(l, b, r) dr \quad (3.11)$$

where  $q_{pp}^{model}$  and  $q_{br}^{model}$  are the local emissivities expected from the cosmic ray model we have assumed. This evaluation makes sense under the assumption that the spectra of  $q_{pp}$  and  $q_{br}$  are not very different along the plane of the Galaxy. This is a good approximation because the proton spectrum is not expected to vary in the Galaxy. The electrons distribution, instead, is probably inhomogeneous for electrons of energy larger than some GeV, but the gamma ray emission for bremsstrahlung around 100 MeV is mainly due to electrons of some hundreds of MeV.

We have then fitted the EGRET observations of cycles from 1 to 9 for the galactic plane, in which the set of gamma-ray photons is binned in ten energy ranges. The fit consists in finding two set of coefficients  $k_{pp}$  and  $k_{br}$  such as

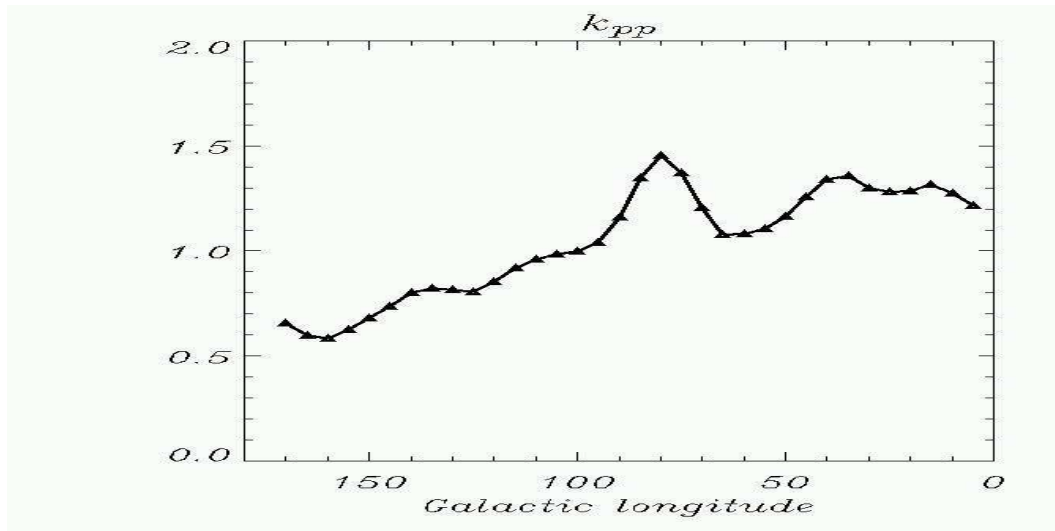


Figure 3.25: Average value of the gamma-ray emissivity due to pp-scattering, weighted on the matter distribution, versus galactic longitude, derived from EGRET observations [Giuliani et al., 2004].

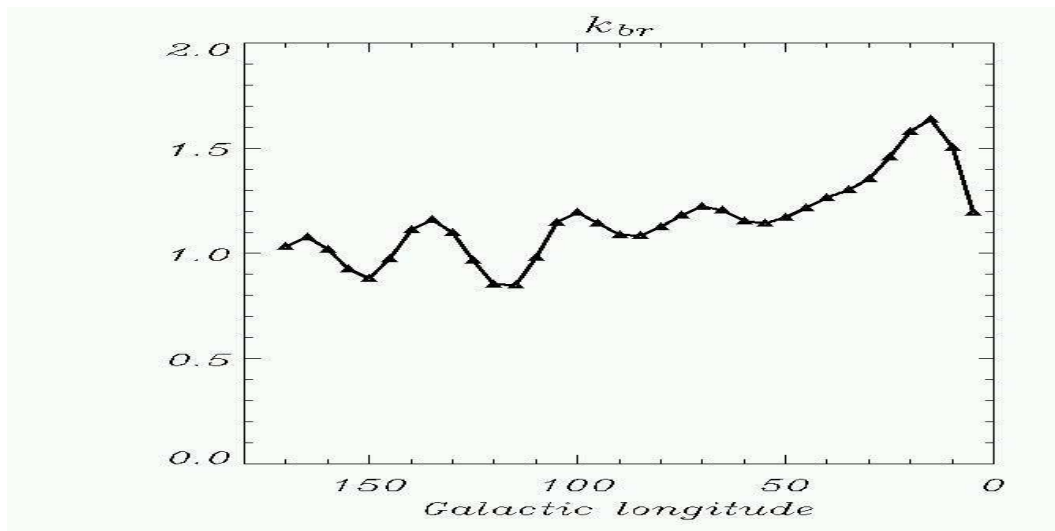


Figure 3.26: Average value of the gamma-ray emissivity due to electron Bremsstrahlung, weighted on the matter distribution, versus galactic longitude, derived from EGRET observations [Giuliani et al., 2004].

$$S(E, l, b) \sim k_{pp}(l, b)S_{pp}^0(E, l, b) + k_{br}(l, b)S_{br}^0(E, l, b) \quad (3.12)$$

The value of  $k_{pp}$  and  $k_{br}$  is, in general, different for every sky direction; these coefficients are hence functions of  $l$  and  $b$ . From equations 3.8 and 3.12 we can obtain:

$$S_{pp}(E, l, b) = k_{pp}(l, b)S_{pp}^0(E, l, b) \quad (3.13)$$

then:

$$k_{pp}(l, b) = \frac{S_{pp}(E, l, b)}{S_{pp}^0(E, l, b)} = \frac{\frac{1}{4\pi}\overline{q_{pp}}(E, l, b) \int n_H(l, b, r)dr}{\frac{1}{4\pi}q_{pp}^{model}(E) \int n_H(l, b, r)dr} = \frac{\overline{q_{pp}}(E, l, b)}{q_{pp}^{model}(E)} \quad (3.14)$$

hence  $k_{pp}$  represents the average value of  $q_{pp}$ , weighted on the matter distribution, and normalized to  $q_{pp}^{model}(E)$ .  $k_{br}$  can be obtained in an analogous way. The gamma-ray emissivities  $q$ 's are proportional to the cosmic-ray density, therefore the derived  $k_{pp}$  and  $k_{br}$  are, in turn, equal to the average values of proton and electron densities respectively ( $\overline{\zeta_p}$  and  $\overline{\zeta_e}$ ). In figures 3.25 and 3.26 the distributions of  $k_{pp}$  and  $k_{br}$ , respectively, are represented as a function of galactic longitude.

In figures 3.23, 3.22, 3.25, and 3.26 it can be noticed how the plots are clearly different. The curves are characterized by two effects: the cosmic-ray matter coupling (for example the prominences in the figure 3.25 at  $l=40$  and  $l=80$ , in correspondence of spiral-arms tangent directions) and a general galactic gradient. The plots generated using the Hunter's model present a remarkable complexity of the structure which is mainly due to the complexity of the

Galactic distribution of the cosmic rays model proposed by the same Hunter. This last model makes use of matter distribution obtained from the radio observation. The matter distribution used by Hunter, based on old radio survey, shows a remarkable irregularity that is due both to errors in the radio survey data distribution and to the deprojection technique used which can induce large errors along the line of sight. Moreover, the assumption of the EGRET model that the ratio between protons and electrons in the Galaxy is constant, implies that  $\overline{\zeta}_p$  and  $\overline{\zeta}_e$  have the same profile along the galactic longitude (figure 3.23). A completely different approach, as the one followed by the model derived from GALPROP, foresees a much more smooth distribution on the galactic plane. The trend of  $\overline{\zeta}$  obtained phenomenologically, by combining the radio observations with a matter distribution obtained with more accurate and more deep radio survey with respect to those used by Hunter, shows an average behavior between the previous models. The different profile of  $\overline{\zeta}_p$  and  $\overline{\zeta}_e$  demonstrates that the assumption of a constant ratio between protons and electrons in the whole Galaxy is not acceptable. Moreover, it can be noticed that the longitudinal gradient is reproduced in both models, even if the Galactic distributions of  $\overline{\zeta}$  are really different. The minor features shown by the functions  $k_{pp}$  and  $k_{br}$  derived by observations are intermediate between the two theoretical models. This can suggest that a CR-matter coupling has to be taken into account even if the interaction shouldn't be as strong as assumed in the EGRET model.

This method, tested on the EGRET data, has given promising results and may be therefore used for the forthcoming observation of AGILE. First at all it can be extended to regions outside the Galactic plane, by introducing a third com-

ponent in the spectrum which takes into account the emissivity contribution for inverse Compton process of the interstellar radiation field. Moreover it is possible to extend the spectrum fit process using two fit parameters for each components, namely, beside the normalization, a further parameter related to the spectral index of electron and proton distribution used to compute the gamma-ray emissivity. In this way maps, in longitude and latitude, of the mean spectral index (averaged on the line of sight) of the electron and proton distributions could be obtained.

### 3.5 AGILE and the Diffuse $\gamma$ -ray emission

The study of Galactic diffuse gamma emission will be one of the main scientific objectives of AGILE, the ASI satellite for gamma-ray astronomy that will be launched in 2005 [Tavani et al., 2003]. The AGILE solid-state tracker (the GRID instrument) will have a field of view considerably larger than that of previous gamma imagers. It will be able to cover  $\pi$  sr with one single pointing with an on-axis effective area about one half of that of EGRET and considerably better above  $30^\circ$  off axis. This means that AGILE will collect, for the same observing time, a number of diffuse photons larger by a factor of two.

AGILE will also be the gamma-ray imager with the best angular resolution obtained to date, about a factor two better than EGRET for photons with energy larger than 400 MeV, with a point spread function depending weakly on off-axis angle. In order to better exploit these capabilities, a very accurate model of the interstellar gamma-ray emission is required for the analysis of AGILE data.

In figures 3.5-3.5 is shown the model described in the previous chapter convolved with the agile Point Spread Function for different energies. These maps show only the contribution of galactic diffuse emission, but in the real observations the gamma ray point sources will be superposed to these structures. Due to the energy dependence of the Point Spread Function the map structures result to be more resolved at high energy, at low energy instead the good resolution of the model is compromised and therefore the difference with the EGRET model becomes less visible. Nonetheless, the two models give different performance also for low energy in term of source analysis.

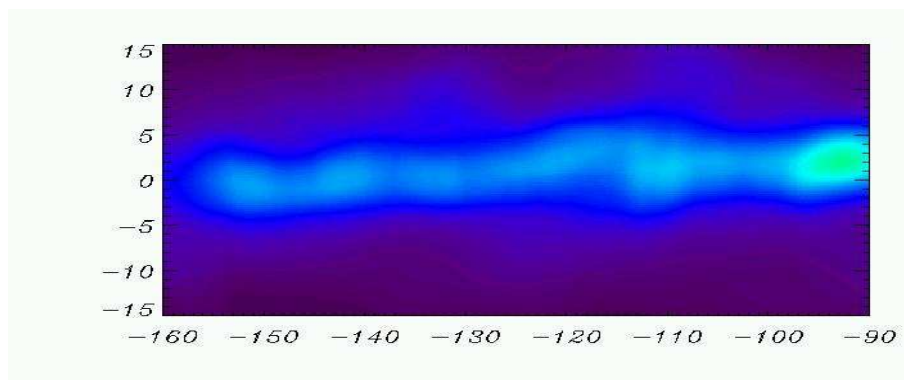


Figure 3.27: The model convolved with the AGILE PSF for 100 MeV.

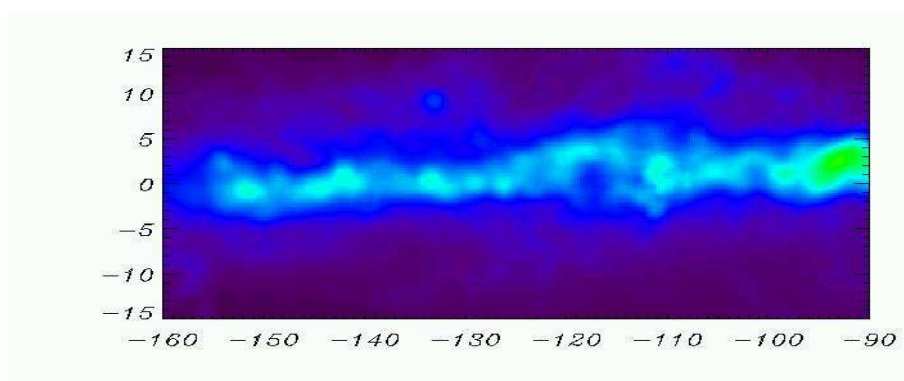


Figure 3.28: The model convolved with the AGILE PSF for 400 MeV.

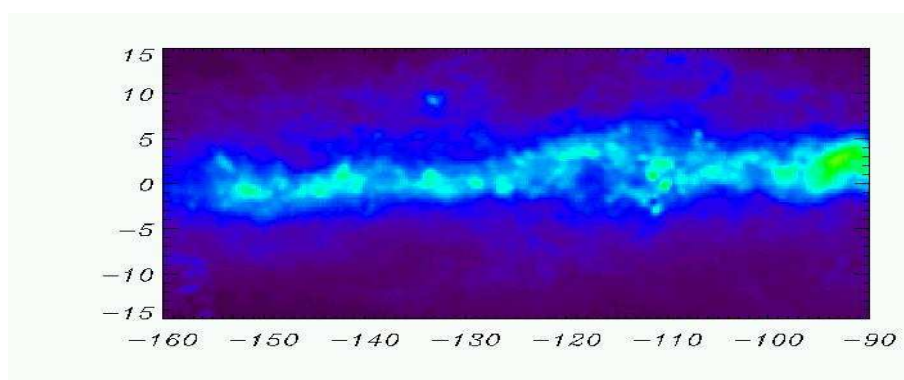


Figure 3.29: The model convolved with the AGILE PSF for 1 GeV.

### 3.6 A simulated AGILE observation

A good knowledge of the diffuse emission model is important also for sources analysis. In order to test the performances of our model from this point of view, we have simulated a set of ten AGILE observations with photons energy above 100 MeV of the second quadrant sky region for a total observing time of about 5 months. In these simulations we have included the diffuse emission model, the point sources from third EGRET catalog and a component of noise due to residual particle background. We have chosen 2GC 135+1 as test source for our analysis. The assumed flux is  $10^{-6}$  photons per  $cm^2$  per second above 100 MeV.

We performed two maximum likelihood analysis [Chen et al., 2004] on the test source using the AGILE and the EGRET models.

Table 3.1: Results of ALIKE analysis for the two models

Parameter (unit)	Value		
<b>2GC 135+01</b>	Flux ( $10^{-8}ph/cm^2s$ )	G mult	G bias
EGRET model	$179 \pm 5$	0.271	11.1
AGILE model	$149 \pm 5$	0.789	7.85

Table 3.6 summarizes the results of the analysis. Second column represents the estimated flux of the test source. We found a better agreement with the simulated value using the AGILE model. Two more parameters are provided by the maximum likelihood method, the multiplicative (G-mult) and additive (G-bias) terms which allow the diffuse emission model used to better fit to the simulation. Also in this case we can notice that a smaller correction is needed for the AGILE model.

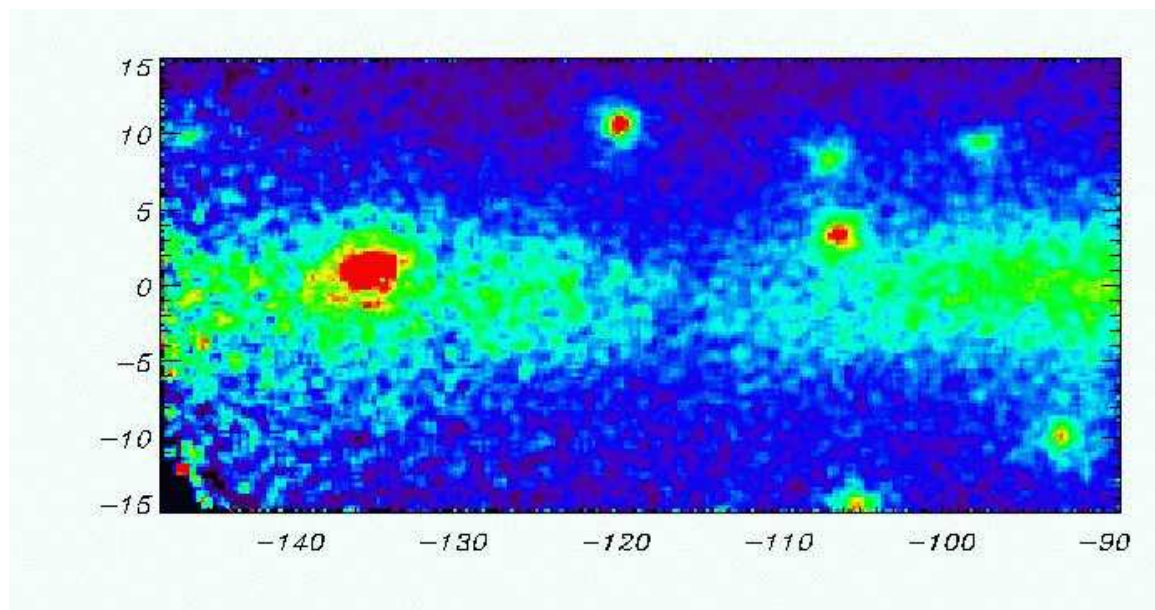


Figure 3.30: The AGILE (simulated) observations of the Galactic plane near 2CG 135+01, for energy  $> 100$  MeV, composed of ten AGILE pointing of the second quadrant sky region for a total observing time of about 5 months. with photons energy above 100 MeV. A component of noise due to residual particle background is also present in the simulation.



## Chapter 4

# AGILE performances optimization

The launch of the AGILE (Astrorivelatore Gamma a Immagini LEggero) satellite, an Italian gamma-ray mission that will observe in the 30 MeV - 30 GeV range is scheduled for the late 2005 [Tavani et al., 2003]. The AGILE observations will permit to increase our knowledge of the gamma-ray emission from the interstellar medium thanks to the peculiar features of this apparatus, such as a good angular resolution and a large field of view. This performance will be achieved exploiting the technology of Silicon microstrip detectors, which are new in the space applications, used in the construction of the AGILE tracker. In order to fully exploit the hardware potentiality of the instrument it is necessary to develop a corresponding high level software. In this chapter the work done to optimize the AGILE performances will be presented in terms of a better signal to noise ratio and energy resolution .

## 4.1 The AGILE instrument

The GRID instrument will be the gamma-ray imager of AGILE, it will be formed by a Silicon-Tungsten tracker and a calorimeter of Iodine-Cesium. AGILE will also have a coded-mask X-ray imager (called Super-AGILE), sensitive in the energy range 15 - 45 keV. A system of anticoincidences formed by 13 panels of plastic scintillator will cover the instrument on the top and lateral sides.

Table 4.1: Comparison between AGILE performances and those of the previous missions dedicated to gamma-ray emission in the energy range larger than some tens of MeV

	SAS-2	COS-B	EGRET	AGILE	GLAST
Field of view (sr)	0.25	0.25	0.5	3	3
Angular Resolution <sup>†</sup>	2°	2°	1.3°	0.7°	0.4°
Effective area <sup>*</sup> ( $cm^2$ )	116	120	1100	500	4000
Sensitivity <sup>‡</sup>	$10^{-6}$	$10^{-6}$	$10^{-7}$	$< 10^{-7}$	$10^{-8}$
Energy Resolution <sup>*</sup>	100%	50%	20%	100%	10%
Energy Range (GeV)	0.02 - 1	0.03 - 5	0.02 - 30	0.03 - 50	0.03 - 300

<sup>†</sup> At 1 GeV

<sup>\*</sup> At 100 MeV

<sup>‡</sup>  $ph\ cm^{-2}\ s^{-1}$ , above 100 MeV

The tracker is formed by 12 planes, each plane (with the exception of the two at the bottom) are made by a tungsten converter layer 250  $\mu m$  thick (corresponding to 0.07 radiation length), and two layers of silicon in which are implanted the microstrips arranged in orthogonal directions to provide the X and Y coordinates of the particle tracks. The last two have only the silicon layers.

The tracker planes have a geometric area of  $1444 \text{ cm}^2$  and the distance be-

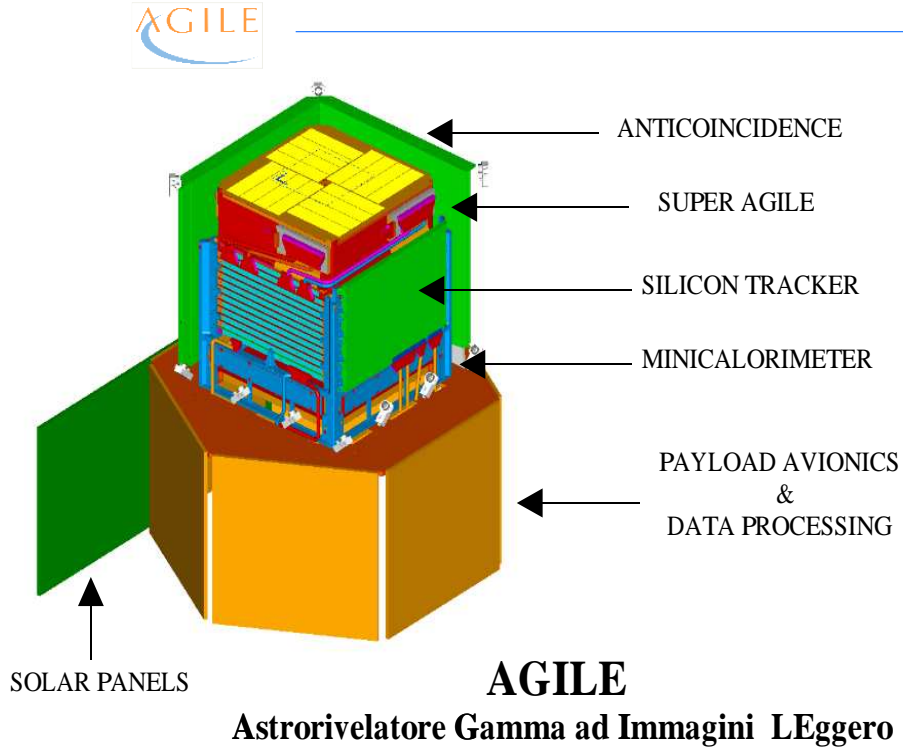


Figure 4.1: The AGILE satellite. The height of the payload is approximately 0.5 m [Tavani et al., 2003].

tween consecutive planes is 19 mm. Each silicon plane is constituted by an array of  $4 \times 4$  square tiles, with a side of 9.5 cm, which constitute the elementary detection cell. The microstrip (that have a pitch of  $121 \mu\text{m}$ ), permit of obtain, using an interpolation algorithm, a measurement of the hits position with an accuracy of about  $40 \mu\text{m}$ , for a wide range of incidence angles. The readout electronics of the silicon strips will work both for collecting tracker information and for trigger purpose of the whole apparatus. This feature, implemented for the first time in space, guarantees to AGILE its large field

of view. The tracker has an on-axis total radiation length larger than 0.84. The resulting effective area is shown in figure 4.2. The Mini-calorimeter consist of two planes of Cesium Iodine bars for a total of 1.5 radiation length. It will allow to estimate the energy of the incident photons imaged by the tracker. In addition the Mini-calorimeter will be used to study the gamma-ray bursts in the 350 keV - 100 MeV range. The two planes have the bars arranged in orthogonal directions to provide the X and Y location of the shower. The scintillation light is collected by photodiodes placed at both ends of each bar. The Super-AGILE detector is based on the  $9.5 \times 9.5 \text{ cm}^2$  silicon tiles that are used for the tracker planes. These will be placed on the top of the tracker to form an additional detection plane sensitive in the 10-40 keV range and used in conjunction with a coded mask at a distance of 14 mm. Since the microstrips provide pixels only along one dimension, Super-AGILE will consist of four equal modules arranged in two pairs, giving monodimensional sky images along two orthogonal directions. The extension in the hard X-ray range of a gamma-ray mission, made possible by the Super-AGILE detector, is an innovative concept that will allow the study of correlated variability for sources of different classes, ranging from active galactic nuclei and blazars to unidentified galactic transients. The Anticoincidence system, aimed at charged particle background rejection, is formed by a top panel and 12 lateral panels. Each panel is made by plastic scintillator, the scintillation light is collected by optical fibers and directed to 16 photomultipliers.

The expected scientific performances of AGILE are summarized in table 4.1. One of the main characteristics of the AGILE gamma-ray detector is its very large field of view. As shown in figure 4.2 the AGILE effective area remains

almost constant for large off-axis angles. This will allow to simultaneously monitor a large number of sources in a single pointing and will also result, at the end of the mission, in a large exposure factor for each region of the sky. The great sky exposure factor, coupled with the good angular resolution, will allow a detailed study of the diffuse Galactic and extra-Galactic emission and to better locate the unidentified EGRET sources. The expected sensitivity for regions along the Galactic plane is shown in figure 4.4.

Another important characteristic of the AGILE tracker is the very small dead time, about  $100 \mu\text{sec}$  (i.e. three orders of magnitude smaller than for EGRET). Furthermore, an on-board GPS system will allow to time tag the photons with an absolute accuracy of only a few  $\mu\text{sec}$ .

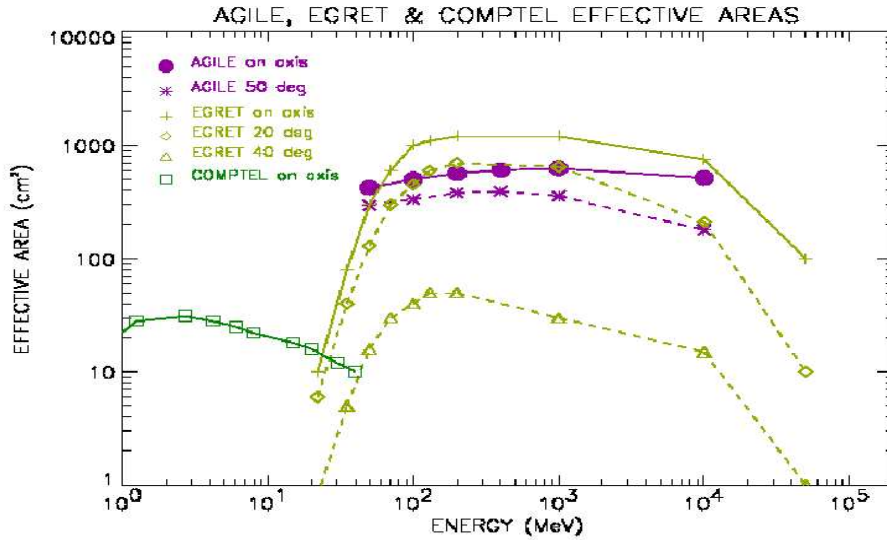


Figure 4.2: The AGILE effective area as function of energy and for different angles, compared to that of other instruments [Tavani et al., 2003].

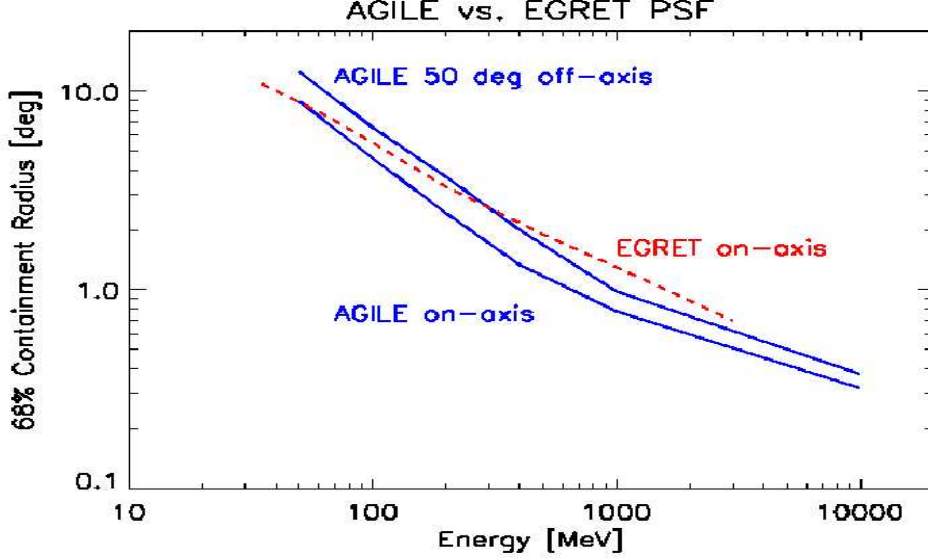


Figure 4.3: The AGILE Point Spread Functions function of energy, preliminary results [Giuliani et al., 2004].

As shown in figure 4.6, the AGILE PSF on-axis (shown at 68% containment radius) is expected to be better than that of EGRET by a factor of  $\sim 2$  above 400 MeV. The angular resolution is weakly dependent on incidence angle ( $\theta$ ), increasing of only a factor 2 for off-axis angle of 60 degrees.

## 4.2 On-board tracks reconstruction

One of the main difficulties of gamma-ray astronomy from space is represented by the huge instrumental noise produced by cosmic rays and the secondaries produced by the interaction of cosmic ray and the terrestrial atmosphere. These particles produce in the GRID instrument a signal similar to that produced by cosmic photons. The primary cosmic rays give a rate of high energy

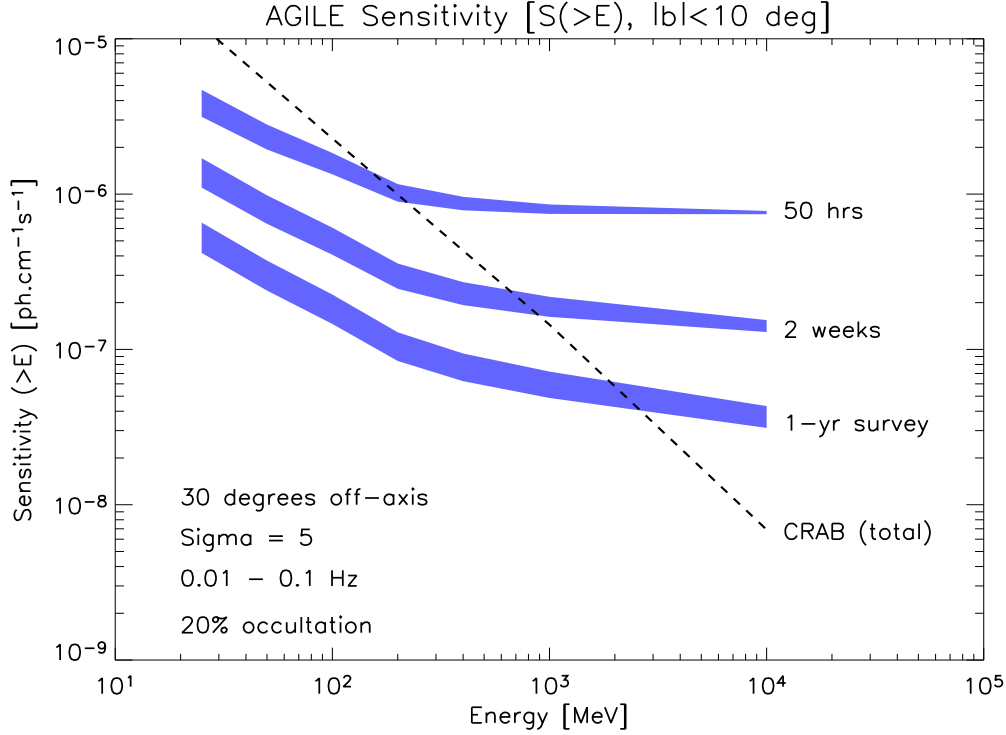


Figure 4.4: The AGILE Sensitivity for a point source on the galactic plane, seen at 30 degree of off-axis angle, for different observation time. Earth occultation and a residual particle background are also taken into account. The spectrum of the Crab pulsar is shown as comparison [Tavani et al., 2003].

events (between about 1 and 100 GeV) , coming from an up-down direction. The interaction of cosmic protons with the Earth's atmosphere produces secondaries, as low energy (less than 1 GeV) protons, electrons, positrons and gamma photons. The terrestrial magnetic field makes the distribution of protons, electrons and positrons arriving at the AGILE tracker isotropic. The secondary gammas (the albedo photons) instead come mainly from the directions in which the line of sight crosses a larger thickness of atmosphere, namely from the terrestrial limb. The total flux of background events is about  $10^{-1}$  *particles/cm<sup>2</sup>sec sr*, hence several orders of magnitude larger than the cosmic

gamma-rays flux. AGILE will have a data-handling system with the scope of cutting a large part of the background rate, that otherwise would give an excessive load for the telemetry channel of scientific data.

The remaining noise rate will be eliminated offline with more complex techniques than those usable on board. The on-board data-handling will process the events through a triggers system consisting of a hardware and a software level. The hardware level accepts only the events that produce some particular configuration of fired anticoincidence panels and tracker planes. The large GRID field of view is based on the capability of this level of exploiting the tracker planes as trigger, without the necessity of other detectors as, for example, the systems of “time of flight” used for the previous gamma-ray missions. This level, thanks to its simplicity, will be able of handle also high rate of events, and it will provide an output event rate of about 100 Hz. The software level will be, in turn, composed by two steps. In the first step it will be applied a set of simple algorithms that, analyzing the event morphology, will be able to eliminate further the background rate (more details on this step of processing can be found in [Cocco et al., 2002]). Nevertheless the event rate after the first software level (estimated in about 30 Hz) is still too high for the capabilities of the telemetry channel. It is then necessary a further processing step, to eliminate the background events, particularly those produced by albedo photons, that can be discriminated by cosmic gamma-rays only on the basis of the incoming direction. In the following paragraphs an algorithm that, carrying out a reconstruction of GRID events, is able of estimate the direction of the incident photon is presented.

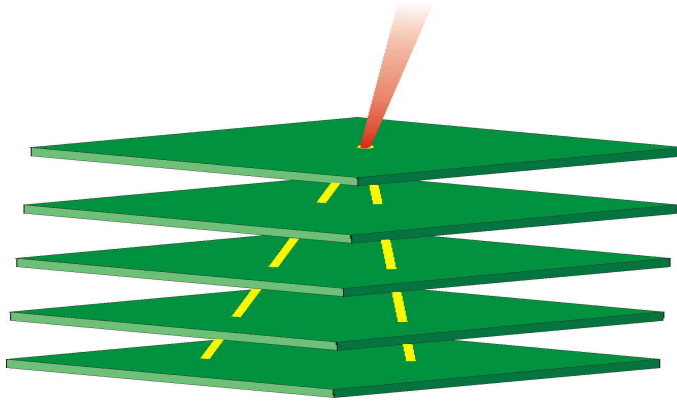


Figure 4.5: A view of the basic interaction in a pair production telescope.

#### 4.2.1 Event reconstruction in pair production detectors

In the pair production telescopes, the  $\gamma$  ray is annihilated with its energy transferred to an electron-positron pair which is created:

$$h\nu \rightarrow e^+ + e^-$$

The interaction takes place in the electric field of a nucleus. The energy and the momentum of the  $\gamma$ -ray are taken by the electron-positron pair, and in a smaller part by the nucleus. Therefore, by measuring the energy and momentum of the pair, the energy and the momentum of the  $\gamma$ -ray are estimated. The reconstruction of the  $\gamma$ -ray direction proceeds through the identification and analysis of the  $e^+e^-$  tracks stemming from the production vertex. At each plane the microstrip on the silicon layers give, separately, the coordinates X and Y of the hits corresponding to the passage of the two electrons. The first step of the event analysis requires to find the two tracks among the possible associations of the hits detected by the tracker silicon layers. This means, in

practical terms, dividing the hits among those belonging to each track and those external to both tracks. This operation is complicated by the fact that the tracks can have a complex morphology, especially at low energy, while at high energy the hits of the two tracks are very close. Moreover the hits of the  $e^+e^-$  pairs, are often superimposed over hits released by  $\delta$ -rays and other secondary phenomena.

Regarding the second step it is necessary to fit the hits of each track with a line which models the electron trajectory. This task is complicated by the fact that electrons path is not a straight line because of the multiple scattering. Moreover, measurements on the electrons passage through the silicon planes are affected by an intrinsic error of not negligible amplitude.

The first two steps are performed separately for the hits corresponding to the X and Y coordinates. A total of four tracks (two for each projection) are then produced. In order to obtain the direction in the three-dimensional space of the electrons moment, it is required to correctly associate the two projection of each track. A technique which allows to maximize the probability of correct association of the projections is then necessary.

### 4.2.2 The "Kalmaex Algorithm"

In order of find and fit tracks a Kalman filter-smoother algorithm [Kalman, 1960], [Frühwirth, 1987] has been developed. Unlike traditional pattern recognition algorithms, this technique always progressively updates the track-candidate information during the track-finding process, predicts as precisely as possible the next hit to be found along the trajectory. This capability is used to merge into an unique recursive algorithm the track-finding procedure and the fitting

of track parameters.

This technique satisfies two crucial requirements for an on-board reconstruction: it provides good results and it don't need much CPU time, it is in fact able to perform a tracks finding and fitting with a little number of basic operations.

In the Kalman filter formalism the electron trajectory is handled as a evolving system, the planes are the instants of this evolution in which it is acquired information on the system. The coordinates of the vector  $(p_k)$ , which describe the system at the plane  $k$ , are the position  $(x_k)$  and the tangent of track direction  $(\tan \theta_k)$ . The Kalman filter is a process parted in two step, called *Filtering* and *Smoothing*.

- *Filtering*: Starting from the first plane, the position and direction of the electron on every plane is estimated on the basis of the track obtained in the previous planes. This estimate is corrected taking into account of the coordinate of the hit closest to the estimated position.
- *Smoothing*: Starting from the last plane, the track is corrected on every plane on the basis of the hits on the planes lying below. In this way the position and direction of the particle passage on the first plane is determined using the information of the entire track.

The evolution law of the state vector is :

$$p_k = F p_{k-1} + w_k \quad (4.1)$$

where  $F$  is the matrix that operate the geometrical projection from a plane to next,

and  $w_k$  is the deviation due to multiple scattering. This effect is described by matrix the  $Q$

$$Q = cov(w_k) \quad (4.2)$$

The errors associate to  $p_k$  are described by the covariance matrix :

$$C_k = cov(p_k - p_k^{true}) \quad (4.3)$$

where  $p_k^{true}$  contain the true values of system at plane k .

At every plane we have a measure of particle passage (  $m_k$  ), the measurement is described by the following relation:

$$m_k = Hp_k + \mu \quad (4.4)$$

where H is the transformation from vector  $p_k$  to the measure.

$\mu$  is the measurement error described by matrix:

$$V = cov(\mu) = ( \sigma^2 ) \quad (4.5)$$

The estimate of system vector is articulated in three steps called *Prediction*, *Filtering* and *Smoothing*.

Former make a projection of the vector from plane k-1 to plane k . This correspond to a prediction of more probable state of the system at plane k made from the states on previous planes.

$$p_k^{proj} = Fp_{k-1} \quad (4.6)$$

the error on  $p_k^{proj}$  is a combination of the errors on  $p_{k-1}$  (projected at plane k) and the multiple scattering effects

$$C_k^{proj} = FC_{k-1}F^T + Q \quad (4.7)$$

A measure on plane k is an independent information of the state vector on plane k, which can be combined with  $p_k^{proj}$  with a weight inversely proportional to the respective errors:

$$\begin{aligned} p_k &= \frac{(C_k^{proj})^{-1}p_k^{proj} + H^TV^{-1}m_k}{(C_k^{proj})^{-1} + H^TV^{-1}H} = \\ &= C_k[(C_k^{proj})^{-1}p_k^{proj} + H^TV^{-1}m_k] \end{aligned} \quad (4.8)$$

where:

$$C_k = [(C_k^{proj})^{-1} + H^TV^{-1}H]^{-1} \quad (4.9)$$

These operations constitute the *filtering*. In this way is possible to insert the measures on the next planes to create a track.

The *smoothing* process carry backward the information. This processing, analogous at the prediction and filtering process, is performed thought a gain matrix on the k-th plane:

$$A_k = C_kF^T(C_{k+1}^{proj})^{-1} \quad (4.10)$$

The state vector become:

$$p_k^{smooth} = p_k + A_k(p_{k+1}^{smooth} - p_{k+1}^{proj}) \quad (4.11)$$

that have an incertitude described by the matrix :

$$C_k^{smooth} = C_k + A_k(C_{k+1}^{smooth} - C_{k+1}^{proj})A_k^T \quad (4.12)$$

Also these operation have to be performed iteratively, proceeding from the last plane to the first. The vector  $p_k^{smooth}$  on the generic plane  $k$  will contain the informations coming from all the available measurements.

In the Kalman filter computation is also possible define a  $\chi^2$  that gives a estimate of the fit goodness. The residuals on each plane are defined as:

$$r_k = m_k - Hp_k^{smooth} \quad (4.13)$$

The matrix with which the residuals are weighted is:

$$R_k = V - HC_k^{smooth}H^T \quad (4.14)$$

It is then possible to calculate the  $\chi^2$  parameter:

$$\chi_k^2 = r_k^T R_k^{-1} r_k \quad (4.15)$$

It is therefore possible to associate at every fitted track a total chi square ( $\chi^2$ ), given by the sum of the  $\chi_k^2$  on each plane. If the combination of the tracker hits gives rise to more than two possible tracks, the  $\chi^2$  can be used to choose the best pair of tracks. In this way the Kalman filter is used not only as fitting

technique, but also as tracks finder. Also the association between X and Y track projection can be performed on the basis of the  $\chi^2$ .

### 4.2.3 Simulation Results

We have applied the Kalmaex algorithm on a set of simulated tracker events (both background particles and gamma-ray photons) obtained by the monte-carlo code GAMS [Longo et al., 2002]. This showed that this technique gives a good result, the precision in direction evaluation is only 30% worst with respect to the precision of the on-ground processing. Figure 4.6 show the 68% containment radius of gamma-ray photons reconstructed with the Kalmaex algorithm as a function of energy for different angles of incidence. The strong dependence on energy is due to multiple scattering effect which affect the less energetic tracks.

### 4.2.4 Background rejection

The algorithm has been applied to a set of simulated photons with direction distribution and energy spectra that reproduce the albedo photons features, when the Earth is partially in the AGILE field of view. The arrival directions of photons are reconstructed in order to discriminate the gamma rays produced by earth atmosphere, which are one of most intense source of noise events at this level of triggers. Figure 4.7 shows the angular separations ( $s$ ) between the derived photon direction and the simulated Earth-center direction. The maximum of distribution correspond to the atmospheric limb which in this simulation is seen at 66 degree of distance from Earth center (corresponding

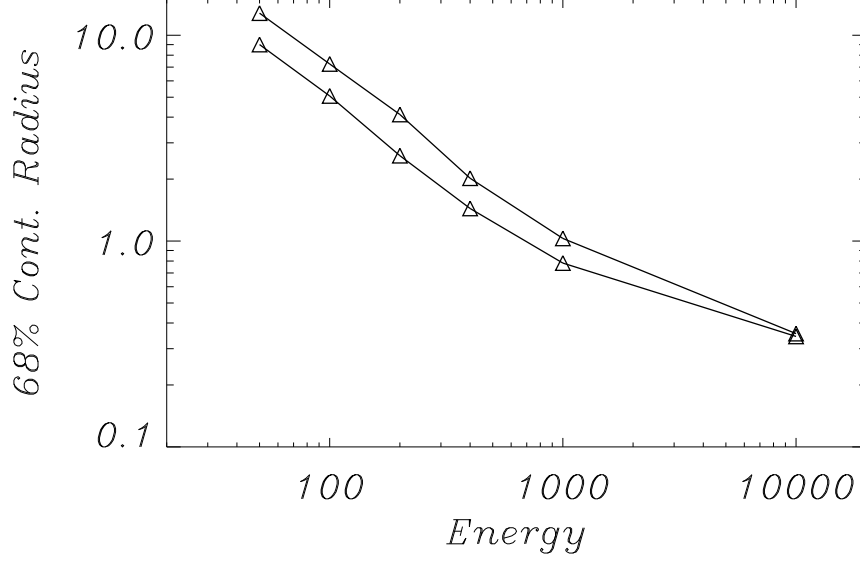


Figure 4.6: 68% containment radius of photons reconstructed with the Kalmex algorithm, for 0 and 50 degree of incidence angles.

to an AGILE altitude of 600 Km). A cut of the events with  $s$  less than  $70^\circ - 80^\circ$  can eliminate about 80% of the albedo photons, allowing to send the remaining events on ground, where they will be realized with more raffinate algorithms.

The Kalmaex algorithm is also able to reject part of the background due to charged particles. The algorithm in fact produces also a quality factor of reconstructed events called  $\chi_{rec}^2$ . If the reconstruction process is applied to spurious events due to charged particles the distribution of  $\chi_{rec}^2$  is very different from that obtained from gamma-ray photons. A cut of events based on the value of  $\chi_{rec}^2$  can therefore reduce the particle background by about 70%.

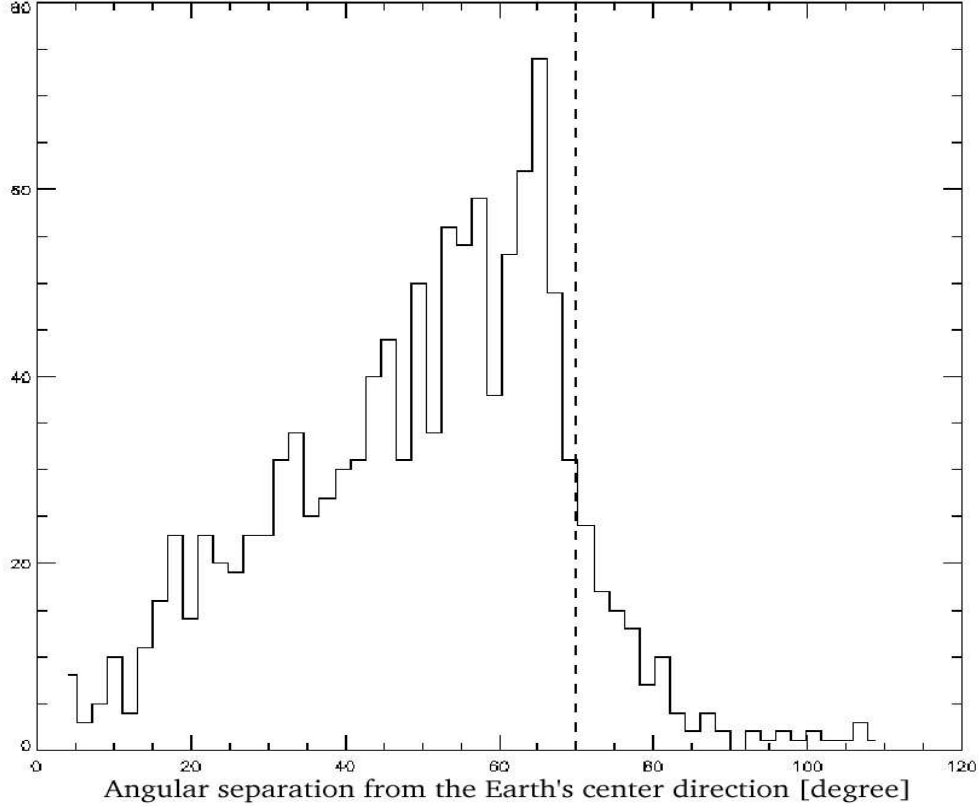


Figure 4.7: Angular distances between the Earth's center direction and the photons reconstructed directions.

### 4.3 On-ground tracks reconstruction

The on ground reconstruction processing is based on the same Kalman filter presented in the previous section, nevertheless some refinements have been introduced in order to improve the reconstruction performances. The main refinement consist in the use of Kalman filter to estimate the energy of the single tracks, which, in turn is used as input of the Kalman filter iteratively. Therefore we find that the AGILE Tracker, thanks to its excellent spatial resolution, can by itself provide a good estimate of the incident photon energy

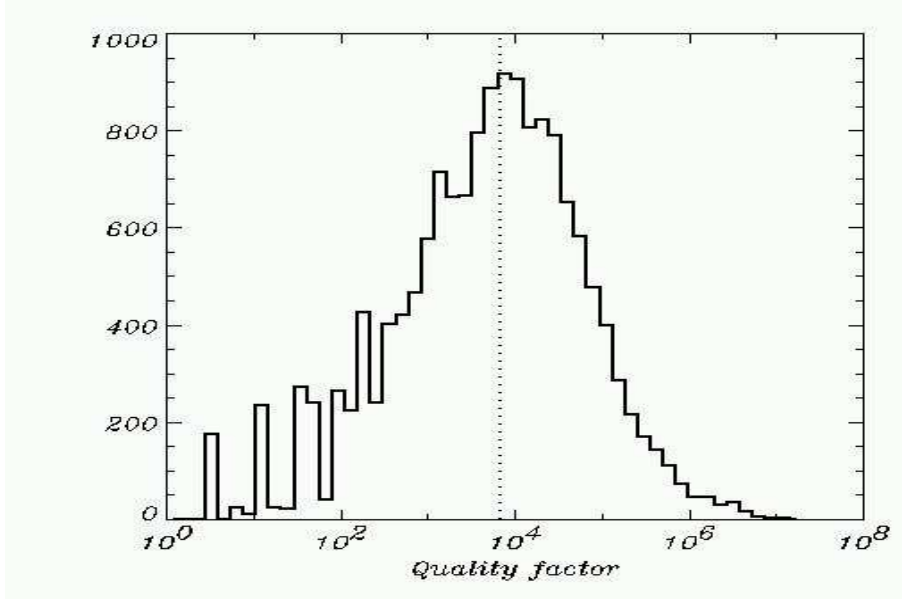


Figure 4.8: Quality factor ( $\chi^2$ ) of background events. The dotted line represent a typical value for a background cut based on this parameter.

from the multiple scattering of  $e^+/e^-$  passing through the converter planes. In fact it is possible to estimate the energy of the electrons from the aspect of their tracks because when an electron passes through a medium undergoes scattering due to interaction with atomic nuclei of the material; smaller the energy, greater the effect. The angular deviation of electrons due to interaction with the material has approximately a Gaussian distribution. Also the projection of this deviation in a view of the instrument has a Gaussian distribution, with standard deviation:

$$\theta_{rms} = \frac{13.6}{E_e[MeV]} \sqrt{\frac{z}{X_0}} \left( 1 + 0.038 \ln \frac{z}{X_0} \right) \quad (4.16)$$

where  $z$  is the thickness and  $X_0$  is the radiation length of the material. There-

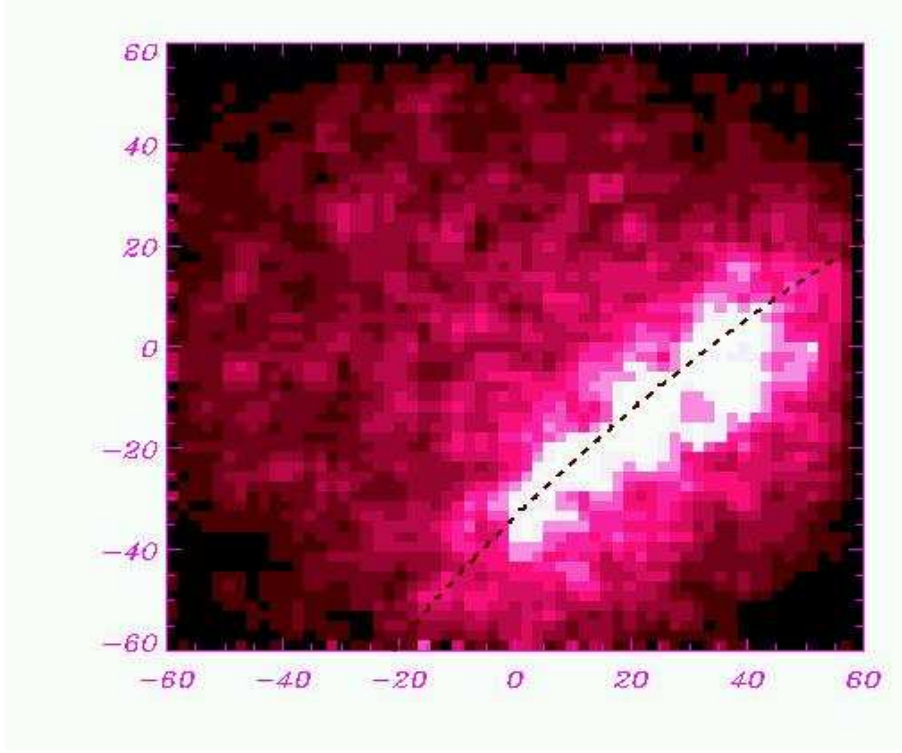


Figure 4.9: Reconstructed image of the Earth limb in the AGILE field of view. The coordinates are given in degrees, the on-axis direction correspond to 0,0 [Giuliani et al., 2004]

fore, once fixed thickness and material, the average scattering angle depends only on particle energy.

The energy evaluation exploits the fact that for every track the electron slope deviation at every plane can be easily measured. It is therefore possible to estimate the energy inverting the equation (4.16), assuming  $\theta_0$  equal to the root mean square of these deviations and assuming:

$$\theta_{rms} = \frac{\sum (\theta_k - \theta_{k-1})^2}{N} \quad (4.17)$$

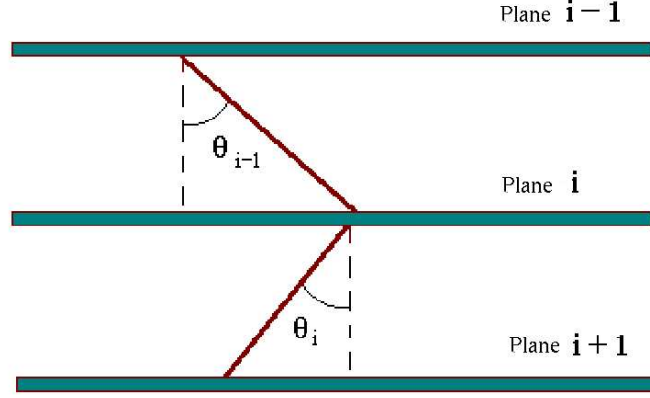


Figure 4.10: Angles definition describing the slopes of the electrons pair.

where  $\theta_k$  is the inclination of particle track after the  $k$ -th plane and  $N$  is the number of crossed planes. This technique is limited by the small number of possible measurements of deviations in one single track (for a track passing through  $N_p$  planes  $N$  is equal to  $N_p - 2$ ).

The inclination of a track at the  $k$ -th plane ( $\theta_k$ ) can be derived in a simple way :

$$\theta_k = \arctan \frac{m_{k+1} - m_k}{d} \quad (4.18)$$

where  $m_k$  is the electron passage coordinate at the  $k$ -th plane and  $d$  is the distance between two planes. The error on  $m_k$  corrupts the measurement of multiple scattering and hence of energy, especially when the scattering angles give deviation comparable or smaller than these errors.

In order to compensate for these errors a Kalman filter can be applied to fit

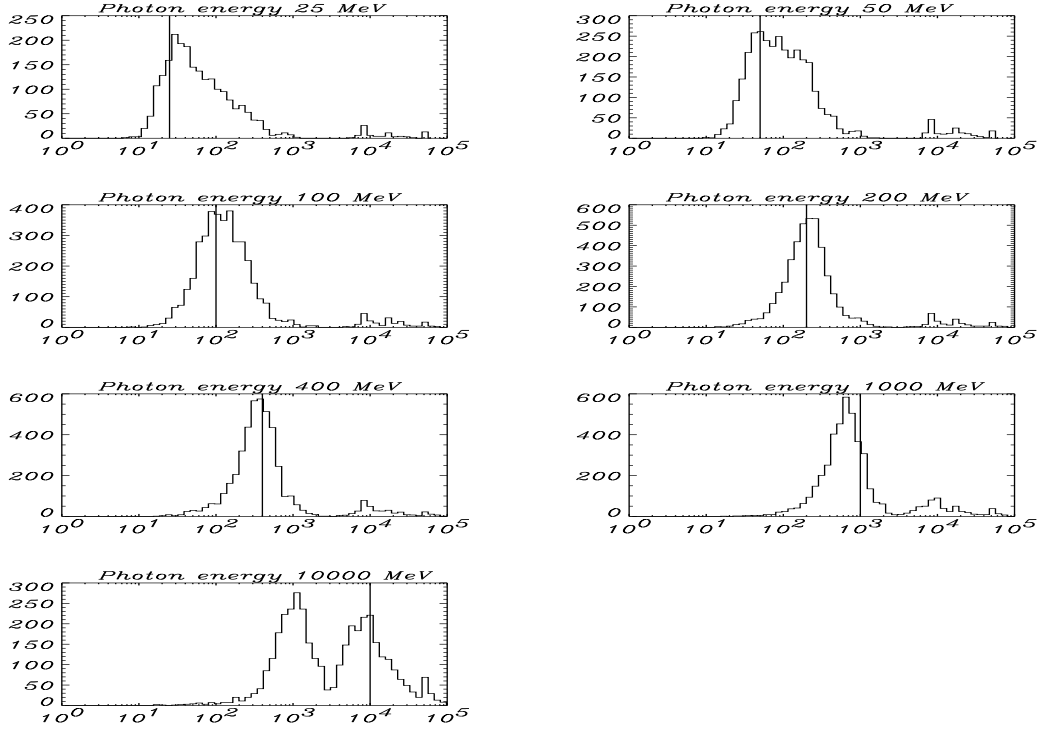


Figure 4.11: Distribution of energy reconstructed with the 'Multiple scattering' method for photons of several energies (photons are 30 degrees off-axis). On the horizontal axis is the reconstructed energy in MeV. The vertical solid line indicates the true energy

the track. In this way it is possible to obtain a better knowledge of the particle path coordinates and, hence, of  $\theta_k$ .

The fit obtained by the Kalman filter is a set of vectors  $p_k$  with elements:

$$p_k = \begin{pmatrix} x_k \\ \tan \theta_k \end{pmatrix} \quad (4.19)$$

therefore the track inclination at every plane can be immediately derived. The Kalman filter needs an evaluation of the particle energy to calculate the fit of the track, and hence the precision obtainable with this kind of fit depends on

precision of energy value. The problem needs to be addressed in an iterative way. An arbitrary energy can be used to start executing the Kalman filter; the values obtained give an evaluation of energy (through eq. 4.17 and 4.16) which is the input for a second Kalman filter. The iteration carries on until the energy values converge.

The distributions of photon energies reconstructed with the method described above are shown in figure 4.11. The simulated photons have the same incoming direction ( $\theta = 30^\circ$   $\phi = 70^\circ$ ) but different energies (from 25 MeV up to 10 GeV).

Table 4.2 shows the three parameters used to describe the distributions. The first parameter,  $E_m$ , is the geometric mean of values. The ratio  $\Delta E/E_m$  indicates the width of distribution. Two "68% containment radius" has been calculated for energies both below and above  $E_m$  and  $\Delta E$  represents the sum of two.  $\Pi$  is the percentage of events with energy reconstructed in the range  $\frac{E_{true}}{1.62} < E < 1.62E_{true}$ . In this way the range is symmetric with respect to  $E_{true}$  (in a logarithmic scale) and the width of range is equal to  $E_{true}$ . Hence if  $\Pi$  equal to 68%,  $\Delta E/E$  is equal to 1. From the results shown in figure 2.1 and in table it can be seen that this method gives good results for intermediate energies (100, 200, 400 MeV and partially at 50 MeV). Photons with very low energies (25 MeV) are badly reconstructed due to their complex morphology and this in turn affects their energy measurement. Photons with high energy (1 - 10 GeV) have multiple scattering angles equal or smaller than the tracker intrinsic resolution (about 0.36 degrees), hence the multiple scattering evaluation is affected by measurement errors.

Table 4.2: Parameters of reconstructed energy distributions. All photons are 30 degrees off-axis

Photon energy	$E_m$ [MeV]	$\Delta E/E_m$	$\Pi$
25 MeV	69	2.9	37 %
50 MeV	116	2.2	37 %
100 MeV	155	1.8	46 %
200 MeV	259	1.5	56 %
400 MeV	435	1.6	57 %
1 GeV	846	6.4	40 %
10 GeV	3050	4.1	24 %

#### 4.3.1 Spectral capabilities

Figure 4.12 shows the energy response matrix obtained by using the method described in section 4.3. The matrix has 8 energy channels with energies between 10 MeV and 50 GeV.

To test the spectral capabilities of the AGILE energy reconstruction method, we simulate an observation of a point source for  $10^6$  sec at 30 degree off-axis with background induced by mid-latitude diffuse  $\gamma$ -ray emission. The source spectrum is described by a power law:

$$F = k \left( \frac{E[\text{Mev}]}{100} \right)^{-\alpha} \quad (4.20)$$

with input photon index  $\alpha = 2$  and differential flux  $k = 1.5 \times 10^{-9}$  ph cm $^{-2}$  s $^{-1}$  MeV $^{-1}$  at  $E = 100$  Mev.

The reconstructed fit values obtained using the response matrix are (at 90% conf. lev.):

$$\alpha = 1.99 \pm 0.2 \quad (4.21)$$

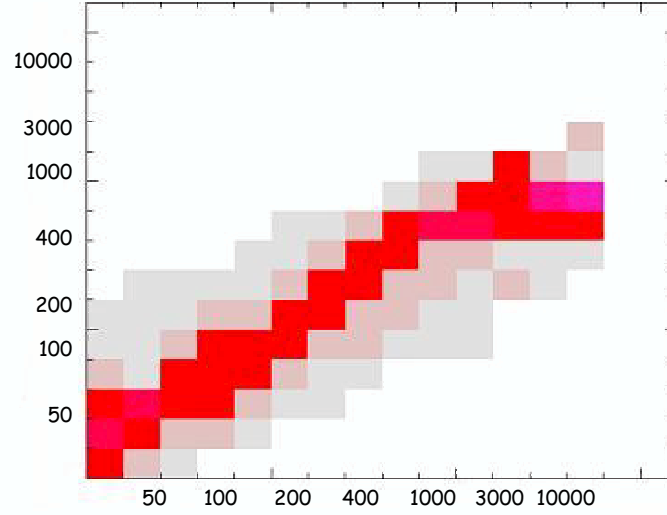


Figure 4.12: The AGILE Response Matrix of energy reconstruction using the Multiple Scattering method. In the abscissa are the true energy channels while in ordinate are the reconstructed energy channels .

and

$$k = 1.56 \times 10^{-9} \pm 1.4 \times 10^{-10} \text{ ph cm}^{-2} \text{ s}^{-1} \text{ MeV}^{-1} \quad (4.22)$$

The preliminary results obtained for the spectral resolution are shown in figure 4.13.

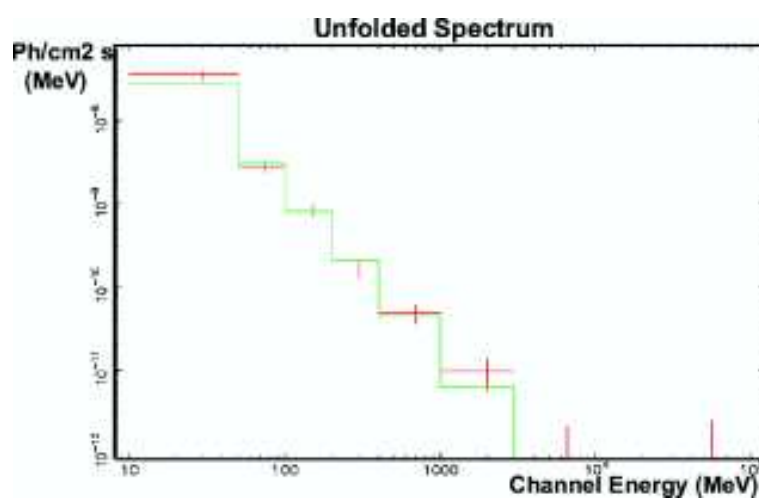


Figure 4.13: Spectral deconvolution for the simulated observation of a point source for  $10^6$  sec at 30 degree off-axis from Tracker-only information. preliminary plots [Giuliani et al., 2003b]



# Chapter 5

## Conclusions

In this thesis I have described the development of a new model of the gamma-ray emissivity (in the MeV - GeV range) of interstellar medium of our galaxy. The model follows the classical approach in which the gamma-ray emissivity is produced by the interaction of the cosmic-ray flux with the interstellar medium, through the process of proton-proton scattering (with production and decay of  $\pi^0$ ), Bremsstrahlung, and inverse Compton scattering. For this model I have obtained the three-dimensional distribution of diffuse matter (HI regions and molecular clouds) in the galactic plane, which, being based on recent radio survey, has a finer resolution and a larger extension with respect to distributions used by previous models.

The intensity of gamma-ray diffuse emission foreseen by this new model agrees quite well with the EGRET observations, both for spatial distribution and spectrum. The angular resolution of gamma-ray emission maps, that can be obtained using this model, are better of a factor of two with respect to previous works. This allows to better cope with the scientific requirements of a new generation of gamma-ray telescopes. The model presented here has been

developed for the AGILE mission and is intended to be an analysis tool for its forthcoming observations. The model is crucial for the study of both diffuse emission and discrete gamma-ray sources. Concerning the study of diffuse emission I have proposed a method to extract information on the cosmic-rays Galactic distribution from the diffuse gamma-ray observations. This method, tested on EGRET data, produced the profile along the Galactic plane of the cosmic-ray (both protons and electrons) density enhancement, which shows a general gradient proceeding from the center to the anticenter region, and a superimposed finer modulation.

The study of gamma-ray point-like sources in the Galactic plane is performed using likelihood techniques that requires a Galactic diffuse emission model as input. The analysis of a simulated AGILE observation shows that more accurate is the diffuse emission model, more precise are the sources features reconstructed by the likelihood calculation.

The AGILE observations will carry new informations on the galactic gamma-ray diffuse emission, because especially of the large field of view and the good angular resolution of its gamma-ray imager. Other two features which need particular attention for a gamma-ray instrument are the energy resolution and the background rejection of spurious events due to charged particles or gamma radiation from terrestrial atmosphere. In the last part of this thesis I presented the study of the optimization of these features. Concerning the energy resolution, I have developed a technique for energy reconstruction of tracker events based on the measure of the multiple scattering suffered by the  $e^+e^-$  pairs. The application of this technique to Montecarlo-simulated data showed that is possible to use the AGILE imaging tracker also as a partial "calorimeter",

obtaining good results in term of energy and spectral resolution. Concerning the background rejection I developed an algorithm able to made a basic reconstruction of tracker events. It produces a quite good estimate of the direction of gamma events, which permits to discriminate the events originated from the Earth's atmosphere. The same algorithm produces also a quality factor of the reconstructed events which can be used to discriminate about 70% of the residual background (both charged particles and albedo photons). Thanks to the good results obtained and its relative simplicity this algorithm as been chosen as part of the AGILE on-board software.



# Acknowledgments

This thesis is the summary of a three years work in the field of astrophysics, and I'd like to thank all the people who has contributed to it.

I'm deeply indebted to my supervisor Sandro Mereghetti, for his attention in following my activities and for his constant friendship.

I wish to acknowledge Marco Tavani for the useful discussions and, above all, for his continuous encouragement.

I'm really grateful to all the Milano AGILE Group for the friendship they have always demonstrated.

I heartily thank Stan Hunter for his great availability in sharing his experience during useful discussions which have helped me in improving my model. I'm most grateful to Andrew Strong for his constructive suggestions about this thesis and for his great kindness.



# Bibliography

- [Aharonian & Atoyan, 2000] Aharonian, F. A. and Atoyan, A. M. (2000). Broad-band diffuse gamma ray emission of the galactic disk. *A&A*, 362, 937–952.
- [Bennett et al., 1977] Bennett, K., Lichti, G. G., Bignami, G. F., Bonnardeau, M., Paul, J. A., Buccheri, R., Scarsi, L., Hermsen, W., Kanbach, G., and Mayer-Hasselwander, H. A. (1977). COS-B observations of localised high-energy gamma-ray emission from the anticentre region of the galactic disc. *A&A*, 56, 469–471.
- [Berezhko & Völk, 2000] Berezhko, E. G. and Völk, H. J. (2000). Galactic Gamma-Ray Background Radiation from Supernova Remnants. *ApJ*, 540, 923–929.
- [Bertsch et al., 1993] Bertsch, D. L., Dame, T. M., Fichtel, C. E., Hunter, S. D., Sreekumar, P., Stacy, J. G., and Thaddeus, P. (1993). Diffuse Gamma-Ray Emission in the Galactic Plane from Cosmic-Ray, Matter, and Photon Interactions. *ApJ*, 416, 587–+.
- [Biermann & Sigl, 2001] Biermann, P. L. and Sigl, G. (2001). Introduction to Cosmic Rays. *Lecture Notes in Physics, Berlin Springer Verlag*, 576, 1–+.

- [Breitschwerdt et al., 2002] Breitschwerdt, D., Dogiel, V. A., and Völk, H. J. (2002). The gradient of diffuse gamma -ray emission in the Galaxy. *A&A*, 385, 216–238.
- [Casadei & Bindi, 2004] Casadei, D. and Bindi, V. (2004). The Origin of Cosmic Ray Electrons and Positrons. *ApJ*, 612, 262–267.
- [Chen et al., 2004] Chen, A., Vercellone, S., Pellizzoni, A., Giuliani, A., Mereghetti, S., and Tavani, M. (2004). Population Studies of Gamma-Ray Sources with AGILE. *Memorie della Societa Astronomica Italiana Supplement*, 5, 191–+.
- [Chi & Wolfendale, 1991] Chi, X. and Wolfendale, A. W. (1991). The interstellar radiation field: a datum for cosmic ray physics. *Journal of Physics G Nuclear Physics*, 17, 987–998.
- [Clemens, 1985] Clemens, D. P. (1985). Massachusetts-Stony Brook Galactic plane CO survey - The Galactic disk rotation curve. *ApJ*, 295, 422–428.
- [Cocco et al., 2002] Cocco, V., Longo, F., and Tavani, M. (2002). Simulation of the agile gamma-ray imaging detector performance: Part ii. *Nuclear Instruments and Methods in Physics Research Section A*, 486, 623–638.
- [Cox et al., 1986] Cox, P., Kruegel, E., and Mezger, P. G. (1986). Principal heating sources of dust in the galactic disk. *A&A*, 155, 380–396.
- [Dame et al., 2001] Dame, T. M., Hartmann, D., and Thaddeus, P. (2001). The Milky Way in Molecular Clouds: A New Complete CO Survey. *ApJ*, 547, 792–813.

- [Dame et al., 1987] Dame, T. M., Ungerechts, H., Cohen, R. S., de Geus, E. J., Grenier, I. A., May, J., Murphy, D. C., Nyman, L.-A., and Thaddeus, P. (1987). A composite CO survey of the entire Milky Way. *ApJ*, 322, 706–720.
- [De Boer et al., 2004] De Boer, W., Herold, M., Sander, C., and Zhukov, V. (2004). Excess of EGRET Galactic Gamma Ray Data interpreted as Dark Matter Annihilation. *astro-ph/0408272*.
- [Dermer, 1986a] Dermer, C. D. (1986a). Binary collision rates of relativistic thermal plasmas. II - Spectra. *ApJ*, 307, 47–59.
- [Dermer, 1986b] Dermer, C. D. (1986b). Secondary production of neutral pions and the diffuse galactic gamma radiation. *A&A*, 157, 223–229.
- [Digel et al., 1999] Digel, S. W., Aprile, E., Hunter, S. D., Mukherjee, R., and Xu, F. (1999). EGRET Observations of the Diffuse Gamma-Ray Emission in Orion: Analysis through Cycle 6. *ApJ*, 520, 196–203.
- [Digel et al., 1996] Digel, S. W., Grenier, I. A., Heithausen, A., Hunter, S. D., and Thaddeus, P. (1996). Diffuse High-Energy Gamma-Ray Emission beyond the Solar Circle: The Cepheus and Polaris Flares and the Perseus Arm. *ApJ*, 463, 609–+.
- [Digel et al., 2001] Digel, S. W., Grenier, I. A., Hunter, S. D., Dame, T. M., and Thaddeus, P. (2001). EGRET Observations of Monoceros: Diffuse Gamma-Ray Emission in the Outer Galaxy. *ApJ*, 555, 12–22.
- [Dopita & Sutherland, 2003] Dopita, M. and Sutherland, R. (2003). *Astrophysics of the Diffuse Universe*. Springer.

- [Erlykin & Wolfendale, 2002] Erlykin, A. D. and Wolfendale, A. W. (2002). Supernova remnants and the origin of cosmic radiation: evidence from low-energy gamma rays. *Journal of Physics G Nuclear Physics*, 28, 2329–2348.
- [Fichtel et al., 1975] Fichtel, C. E., Hartman, R. C., Kniffen, D. A., Thompson, D. J., Ogelman, H., Ozel, M. E., Tumer, T., and Bignami, G. F. (1975). High-energy gamma-ray results from the second small astronomy satellite. *ApJ*, 198, 163–182.
- [Frühwirth, 1987] Frühwirth, R. (1987). Application of kalman filtering to track and vertex fitting. *Nuclear Instruments and Methods in Physics Research*, A262, 444–450.
- [Giuliani et al., 2003a] Giuliani, A., Chen, A., Mereghetti, S., Pellizzoni, A., Tavani, M., and Vercellone, S. (2003a). *Gamma Emission from the Galaxy: a new model for AGILE*. Proceedings of the 4th AGILE Science Workshop, Frascati (Roma), 11–13.06.2003.
- [Giuliani et al., 2003b] Giuliani, A., Lipari, P., Pittori, C., Tavani, M., and Zanello, D. (2003b). *Optimization of the Angular and Energy Resolution of the AGILE Gamma-Ray Detector*. Proceedings of the 4th AGILE Science Workshop, Frascati (Roma), 11–13.06.2003.
- [Giuliani et al., 2004] Giuliani, A., Mereghetti, S., and Tavani, M. (2004). . In preparation.
- [Hartmann & Burton, 1997] Hartmann, D. and Burton, W. B. (1997). *Atlas of galactic neutral hydrogen*. Cambridge; New York: Cambridge University Press, ISBN 0521471117.

- [Hunter et al., 1997] Hunter, S. D., Bertsch, D. L., Catelli, J. R., Dame, T. M., Digel, S. W., Dingus, B. L., Esposito, J. A., Fichtel, C. E., Hartman, R. C., Kanbach, G., Kniffen, D. A., Lin, Y. C., Mayer-Hasselwander, H. A., Michelson, P. F., von Montigny, C., Mukherjee, R., Nolan, P. L., Schneid, E., Sreekumar, P., Thaddeus, P., and Thompson, D. J. (1997). EGRET Observations of the Diffuse Gamma-Ray Emission from the Galactic Plane. *ApJ*, 481, 205–+.
- [Hunter et al., 1994] Hunter, S. D., Digel, S. W., de Geus, E. J., and Kanbach, G. (1994). Gamma-ray observations of Ophiuchus with EGRET: The diffuse emission and point sources. *ApJ*, 436, 216–228.
- [Kalman, 1960] Kalman, R. E. (1960). A new approach to linear filtering and prediction problems. *Journal of Basic Engineering*, pages 35–45.
- [Kerr et al., 1986] Kerr, F. J., Bowers, P. F., Jackson, P. D., and Kerr, M. (1986). Fully sampled neutral hydrogen survey of the southern Milky Way. *A&AS*, 66, 373–504.
- [Kraus, 1986] Kraus, J. (1986). *Radio Astronomy*. ed. Powell.
- [Kraushaar et al., 1972] Kraushaar, W. L., Clark, G. W., Garmire, G. P., Borken, R., Higbie, P., Leong, V., and Thorsos, T. (1972). High-Energy Cosmic Gamma-Ray Observations from the OSO-3 Satellite. *ApJ*, 177, 341–+.
- [Longo et al., 2002] Longo, F., Cocco, V., and Tavani, M. (2002). Simulation of the agile gamma-ray imaging detector performance: Part i. *Nuclear Instruments and Methods in Physics Research Section A*, 486, 610–622.

- [Mori, 1997] Mori, M. (1997). The Galactic Diffuse Gamma-Ray Spectrum from Cosmic-Ray Proton Interactions. *ApJ*, 478, 225–+.
- [Pohl & Esposito, 1998] Pohl, M. and Esposito, J. A. (1998). Electron Acceleration in Supernova Remnants and Diffuse Gamma Rays above 1 GeV. *ApJ*, 507, 327–338.
- [Pohl et al., 1997] Pohl, M., Kanbach, G., Hunter, S. D., and Jones, B. B. (1997). The Pulsar Contribution to the Diffuse Galactic Gamma-Ray Emission. *ApJ*, 491, 159–+.
- [Skibo, 1993] Skibo, J. G. (1993). Diffuse Galactic Positron Annihilation Radiation and the Underlying Continuum. *Ph.D. Thesis*.
- [Sreekumar, 1993] Sreekumar, P. (1993). . *Phys. Rev. Lett.*, 70, 127–129.
- [Strong et al., 2000] Strong, A. W., Moskalenko, I. V., and Reimer, O. (2000). Diffuse Continuum Gamma Rays from the Galaxy. *ApJ*, 537, 763–784.
- [Strong et al., 2004a] Strong, A. W., Moskalenko, I. V., and Reimer, O. (2004a). Diffuse Galactic Continuum Gamma Rays: A Model Compatible with EGRET Data and Cosmic-Ray Measurements. *ApJ*, 613, 962–976.
- [Strong et al., 2004b] Strong, A. W., Moskalenko, I. V., Reimer, O., Digel, S., and Diehl, R. (2004b). The distribution of cosmic-ray sources in the Galaxy,  $\gamma$ -rays and the gradient in the CO-to- $H_2$  relation. *A&A*, 422, L47–L50.
- [Tavani et al., 2003] Tavani, M., Barbiellini, G., Argan, A., Auricchio, N., Bernabeo, A. R., Bulgarelli, A., Caraveo, P. A., Celesti, E., Chen, A., Cocco, V., Costa, E., Del Monte, E., De Paris, G., Di Cocco, G., Fedel,

- G., Feroci, M., Fiorini, M., Froysland, T., Galli, M., Gianotti, F., Giuliani, A., Labanti, C., Lapshov, I., Lazzarotto, F., Lipari, P., Longo, F., Mastropietro, M., Mattaini, E., Mauri, A., Mereghetti, S., Morelli, E., Morselli, A., Pacciani, L., Pellizzoni, A., Perotti, F., Picozza, P., Pittori, C., Pontoni, C., Porrovecchio, G., Preger, B., Prest, M., Rapisarda, M., Rossi, E., Rubini, A., Sant'Ambrogio, E., Soffitta, P., Soli, L., Traci, A., Trifoglio, M., Vallazza, E., Vercellone, S., Zambra, A., and Zanello, D. (2003). The AGILE instrument. pages 1151–1162.
- [Thompson et al., 1993] Thompson, D. J., Bertsch, D. L., Fichtel, C. E., Hartman, R. C., Hofstadter, R., Hughes, E. B., Hunter, S. D., Hughlock, B. W., Kanbach, G., Kniffen, D. A., Lin, Y. C., Mattox, J. R., Mayer-Hasselwander, H. A., von Montigny, C., Nolan, P. L., Nel, H. I., Pinkau, K., Rothermel, H., Schneid, E. J., Sommer, M., Sreekumar, P., Tieger, D., and Walker, A. H. (1993). Calibration of the Energetic Gamma-Ray Experiment Telescope (EGRET) for the Compton Gamma-Ray Observatory. *ApJS*, 86, 629–656.